The University of Nottingham

UNITED KINGDOM · CHINA · MALAYSIA

MOLECULAR MODELLING OF THE CANNABINOID RECEPTORS: STRUCTURE-BASED DESIGN, SYNTHESIS AND PHARMACOLOGICAL EVALUATION OF NOVEL LIGANDS BASED ON THE FENOFIBRATE SCAFFOLD

JASON LOO SIAU EE

MPharm, R.Ph

School of Pharmacy

The University of Nottingham Malaysia Campus

Thesis submitted to the University of Nottingham for the degree of Doctor of Philosophy

February 2015

ABSTRACT

The cannabinoid receptors CB1 and CB2, which belong to the rhodopsin family of GPCRs, are implicated in the pathology of various disease states. As drugs targeting these receptors remain limited, novel cannabinoid receptor ligands represent an unmet need with substantial therapeutic potential. We present here the construction and application of homology models of the human CB1 and CB2 cannabinoid receptors based on the crystal structure of the human adenosine A2A receptor for the structure-based design of novel ligands based on the fenofibrate scaffold. Models were refined through molecular dynamic simulations in a lipid bilayer, and were validated via the prediction of known ligand binding affinities, enrichment studies and assessment of predicted ligand binding modes. These validated models were subsequently used in predicting the binding mode of fenofibrate derivatives to the cannabinoid receptors. The predicted binding mode of these fenofibrate derivatives to the CB2 receptor showed good agreement with known mutagenesis data, indicating the binding of these compounds to be stabilized primarily by hydrogen bonds with W5.43 and C7.42, aromatic stacking with F2.57, F3.36 and W6.48, and hydrophobic contact with F2.64, V3.32 and I5.47. A series of novel ligands was derived based on these findings, docked into our model, synthesized and pharmacologically evaluated at the CB2 receptor. The pharmacology of these ligands validated our modelling predictions and binding mode hypothesis, with several of these ligands showing unique pharmacology by binding in an allosteric manner. These findings may be used to guide the design of further derivatives and highlight the promise of the fenofibrate scaffold in the development of novel CB2 receptor ligands.

ACKNOWLEDGEMENTS

LIST OF ABBREVIATIONS

Δ^9-THC	Delta-9 tetrahydrocannabinol
2-AG	2-arachidonyl glycerol
A_{2A}	Adenosine receptor 2A
AIDS	Acquired immunodeficiency syndrome
ATB	Automated Force Field Topology Builder
ATP	Adenosine triphosphate
AUC	Area under curve
BSA	Bovine serum albumin
cAMP	Cyclic adenosine monophosphate
CB1	Cannabinoid receptor 1
CB2	Cannabinoid receptor 2
$CHCl_3$	Chloroform
CHO	Chinese Hamster Ovary
CINV	Chemotherapy-induced nausea and vomiting
CNS	Central nervous system
DAG	Diacylglycerol
DCE	1,2 dichloroethane
DCM	Dichloromethane
DIAD	Diisopropyl azodicarboxylate
DMF	Dimethylformamide
EDTA	Ethylenediaminetetraacetic acid
EtOAc	Ethyl acetate
EMEA	European Medicines Agency
FAAH	Fatty acid amide hydrolase

fs	Femtosecond
FDA	U.S Food and Drug Administration
FTIR	Fourier transform infrared spectroscopy
GDP	Guanosine diphosphate
GPCR	G protein-coupled receptor
GTP	Guanosine triphosphate
HCl	Hydrochloric acid
HDL	High density lipoprotein
HMDS	1,1,1,3,3,3-hexamethyldisilazane
HPLC	High performance liquid chromatography
HRMS	High resolution mass spectroscopy
IP_3	Inositol triphosphate
K	Kelvin
LDL	Low density lipoprotein
MAPK	Mitogen-activated protein kinase
MeCN	Acetonitrile
MD	Molecular dynamics
$MgCl_2$	Magnesium chloride
MS	Multiple sclerosis
NaCl	Sodium chloride
NaOH	Sodium hydroxide
NAPE	N-arachidonylphosphatidylethanolamide
NMR	Nuclear magnetic resonance
ns	Nanosecond
NSB	Non-specific binding
PBS	Phosphate buffered saline

PIP2	Phosphatidyl inositol diphosphate
PKA	Protein kinase A
PKC	Protein kinase C
PPAR	Peroxisome proliferator-activated receptor
POPC	Palmitoyl-oleoyl-phosphatidylcholine
ps	Picosecond
Rf	Retention factor
RMSD	Root mean square deviation
ROC	Receiver Operating Characteristic
SEM	Standard error of the mean
T4L	T4-lysozyme
THF	Tetrahydrofuran
TLC	Thin layer chromatography
TM	Transmembrane
Tris	tris(hydroxymethyl)aminomethane
VDW	Van der Waals

TABLE OF CONTENTS

1   INTRODUCTION

1.1   G protein-coupled receptors

1.1.1   Structure, function, and classification

The G protein-coupled receptor (GPCR) superfamily is one of the largest and most varied family of proteins in the human genome, consisting of approximately 800 members (1). The receptors under this superfamily are diverse in both their function and the ligands that they bind, regulating a myriad of physiological processes, from smell and taste to the control of blood pressure, sleep regulation and pain. These processes are mediated by various extracellular ligands that include biogenic amines, peptides, ions and nucleotides, among others. Despite this diversity, all GPCRs share two common features. Firstly, the overall structure of all GPCRs are similar: consisting of seven transmembrane α-helices, an extracellular N-terminus, an intracellular C-terminus, and three interhelical loops on each side of the cell membrane (see Figure 1-1) (1,2). Hence, the GPCRs are also known as ''7-transmembrane receptors'' and ''heptahelical receptors'', although the term GPCR is by far more established. Secondly, as implied by their name, GPCRs are also able to interact with and signal through guanosine-nucleotide binding proteins (G proteins) of various subtypes, although this property has yet to be demonstrated for many GPCRs, particularly the orphan receptors (more than 100 GPCRs with currently no known ligand) (3).
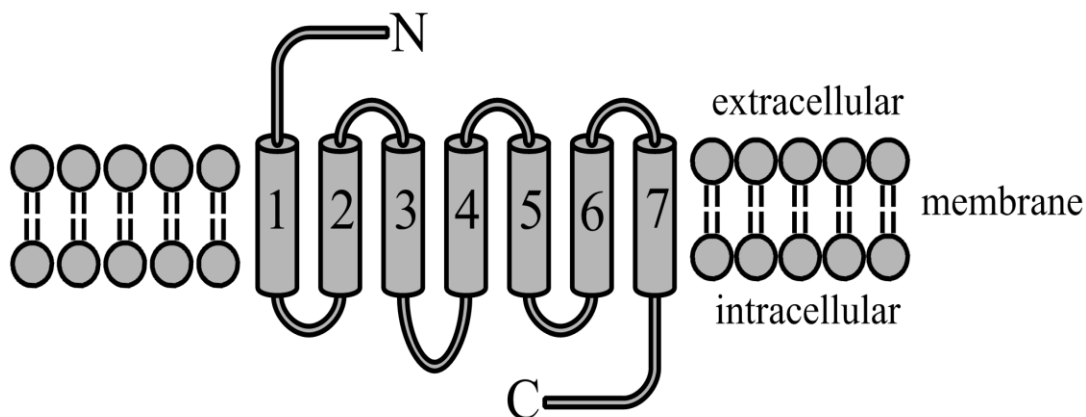
Figure 1-1 Schematic structure of a typical G protein-coupled receptor.

Due to the vast variation present, there have been several classification systems used over the years to sort the GPCR superfamily, mostly utilizing sequence similarity and phylogenetic analysis as classification tools. Previously, one of the most frequently used classification systems divided the GPCRs according to the classes A to F, which represented rhodopsin-like, secretin-like, metabotropic glutamate-like, fungal pheromone, cAMP and frizzled/smoothened GPCRs respectively (4). This classification system was designed to include GPCRs from all species, and includes classes that do not appear in humans, such as the fungal pheromone and cAMP classes. More recently, Fredriksson *et al* presented the increasingly popular GRAFS classification system following phylogenetic analysis of the GPCR sequences found in the human genome (1). GRAFS itself is an acronym of the families identified, namely glutamate, rhodopsin, adhesion, frizzled/taste2, and smoothened.

1.1.2 Activation and signal transduction in GPCRs

1.1.2.1 Pathways mediated through G proteins

While it is becoming increasingly recognized that not all GPCRs currently classified as such may be able to interact with G proteins, the majority of the GPCRs still exploit these signal transduction pathways from which their name is derived. G proteins are heterotrimeric proteins whose activation is linked to guanosine diphosphate (GDP) - guanosine triphosphate (GTP) exchange, and are composed of three subunits (α, β, and γ), with several subtypes of each (see Figure 1-2) (5).
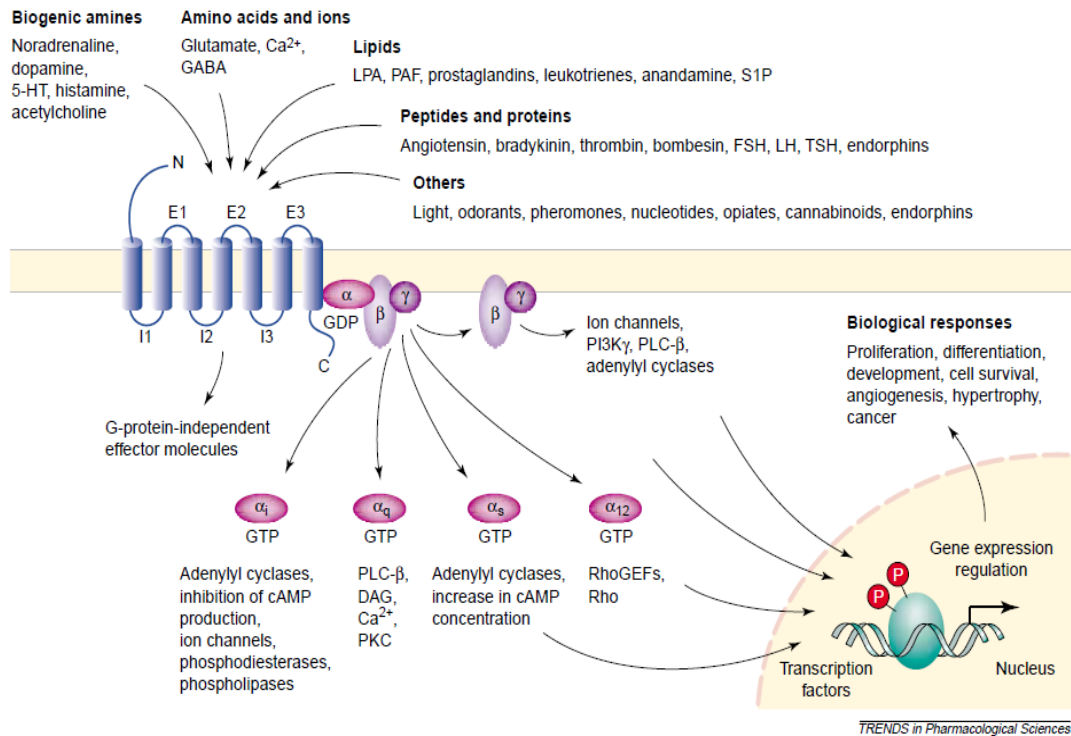
Figure 1-2 Diversity of GPCR ligands and signalling pathways. Taken from reference (6)

In the inactive state, the Gα subunit contains a GDP molecule within its binding pocket. Following ligand binding, a conformational change is induced in the GPCR that allows for interaction of the cytoplasmic face of the receptor with the C terminus of the Gα subunit, while the Gβγ subunit stabilizes this interface (5,7). This in turn catalyses the exchange of GDP for GTP in the Gα subunit, and upon GTP binding the Gα subunit dissociates from both receptor and the Gβγ subunit, proceeding to effect second messenger mechanisms within the cell (8). The G protein-receptor complex is therefore transient in nature, as the much higher concentration of GTP within the cell ensures rapid exchange with GDP. The activated receptor is consequently able to interact with several other G proteins before its bound ligand dissociates, contributing to signal amplification (5,8). While the signalling cascades mediated through G proteins are complex, they can broadly be divided into 4 main families based on the Gα subunit: G_S, $G_{i/o}$, $G_{q/11}$, and $G_{12/13}$ (2). Specific receptors have specific preferences for the G proteins that they couple with, although it has been demonstrated that many GPCRs are able to activate several types of G proteins to a certain degree (5).

G_S dissociation from the G protein results in the activation of the adenylyl cyclase pathway, leading to a cellular increase of cyclic adenosine monophosphate (cAMP) concentration and the subsequent activation of protein kinase A (PKA) (2,8). In contrast, G_i acts in an opposing manner on the same pathway, leading to an inhibition of adenylyl cyclase activity (2). The G_q subunit activates the enzyme phospholipase C, which in turn cleaves the cell membrane component phosphatidylinositol diphosphate (PIP2) into two second messengers, diacylglycerol (DAG) and inositol triphosphate (IP_3) (2,8). This ultimately results in the activation of protein kinase C (PKC) and an increase in intracellular calcium levels, subsequently activating calcium-dependent and calmodulin-dependent protein kinases.

Although the Gα subunit has been more extensively studied in G protein-mediated signalling, it has emerged that the Gβγ dimer itself activates or inhibits a vast range of proteins,

including adenylyl cyclase, G protein-activated inward rectifier K^+ channels, and PKC, among others (9–13). Notably however, higher concentrations of the Gβγ dimer are required before a significant response is generated when compared to the Gα subunit, as has been shown experimentally for phospholipase C (14). This ability to mediate several pathways at once demonstrates the complexity involved in G protein signalling, allowing for the fine control of cellular processes.

1.1.2.2 Signalling through G protein-independent pathways

It has becoming increasingly evident in recent years that activated GPCRs may produce biochemical responses independent of heterotrimeric G proteins and the classical second messengers (6). These pathways may be mediated through other non-GPCR membrane receptors such as receptor activity modifying proteins, other membrane proteins, or other intracellular molecules (2,6). For example, following phosphorylation of the receptor, β-arrestin molecules (an adaptor molecule involved in receptor internalization) bound to the GPCR may link the receptor to Src-kinase activation and subsequent activation of components in the mitogen-activated protein kinase (MAPK) pathway (15). Similarly, several GPCRs have been shown to complex with small GTP-binding proteins such as Ras, Rab, and Rho, leading to activation of phospholipase D (16).

GPCRs are now understood to mediate a multitude of interconnected signalling pathways, with the final outcome a composite product of the various G proteins and signal transduction pathways activated at any one time. As such, there have been valid arguments that the term "G protein-coupled receptor" is no longer appropriate, and that the designation "seven-transmembrane receptor" or "heptahelical receptor" be preferably used (16).

1.1.3 GPCRs: An area of continued interest in drug discovery

The fact that the GPCRs are so varied has made them one of the top targets in drug discovery and development today, with an estimated 30% of the pharmaceuticals available on the market targeting them (17). Table 1-1 depicts some examples of successful pharmaceuticals targeting the GPCRs. Despite this large market share, these drugs currently target only approximately 30 GPCRs, with a large contribution from the rhodopsin family, particularly the biogenic amine receptors (17). Therefore, the remaining known GPCRs within the superfamily, together with the orphan receptors, represent a vast amount of untapped potential for future pharmaceutical research and development, although it should be noted not all GPCRs may play a pathological or targetable role in disease states.

Trade Name (Generic name)	GPCR targeted	Indication	Company
Plavix® (Clopidogrel)	Purinergic P2Y12	Myocardial infarction	Sanofi-Aventis
Zyprexa® (Olanzapine)	Serotonin 5HT2, Dopamine D1,D2, D4 Muscarinic M1, Adrenergic α1, Histamine H1	Schizophrenia, bipolar disorder	Eli Lilly
Diovan® (Valsartan)	Angiotensin AT2	Hypertension, heart failure, post myocardial infarction	Novartis
Serevent® (Salmeterol)	Adrenergic β2	Asthma	GlaxoSmithKline
Oxycontin® (Oxycodone)	Opioid κ	Pain	Purdue Pharma
Singulair® (Montelukast)	Cysteinyl leukotriene CysLT1	Asthma	Merck
Clarityn® (Loratadine)	Histamine H1	Allergic rhinitis	Schering-Plough

Table 1-1 Examples of marketed drugs targeting GPCRs.

1.1.4 Pharmacological assays for GPCRs

Research efforts involving GPCRs primarily focus on the discovery of novel ligands as leads for the development of potential therapeutic compounds. Novel ligands are typically assessed *in vitro* for binding affinity and efficacy using cell lines stably transfected with the receptor of interest. Binding affinity (K_i) is frequently determined using a competition binding assay with a known radiolabelled ligand. Functional activity (i.e. whether a ligand is an agonist, neutral antagonist, or inverse agonist) can be determined using a variety of functional assays that measure either GTP, cAMP or IP_3 levels using radiometric, luminescence or fluorescence techniques (18).

Most GPCRs typically possess some degree of constitutive activity (a basal level of activation in the absence of any agonist) due to a proportion of the receptors being in an activated state. Full agonists induce the maximal level of activation possible, partial agonists activate the receptor above basal levels but not maximally, neutral antagonists bind to the receptor but maintains basal levels by neither stimulating nor inhibiting the receptor, while inverse agonists decrease the level of receptor activation below basal levels (19).
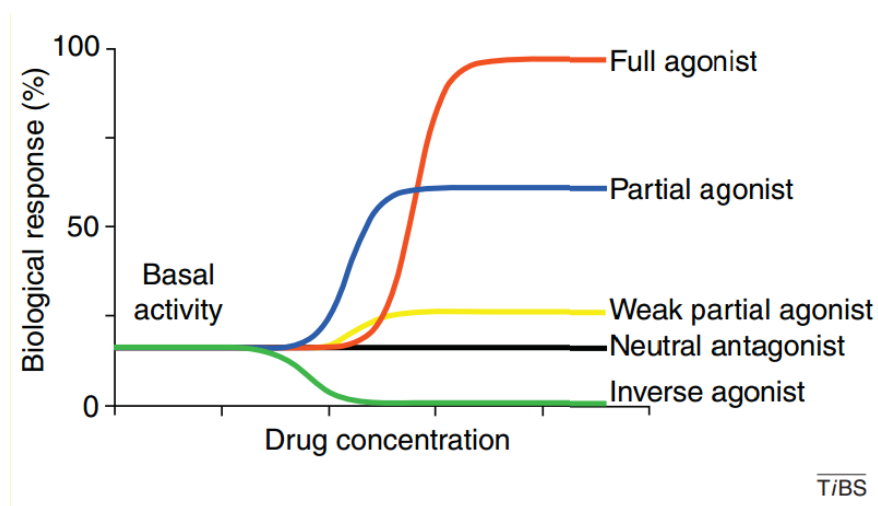
Figure 1-3 Pharmacological effect of agonists, partial agonists, neutral antagonists and inverse agonists. Taken from reference (19).

As the $[^{35}S]$GTPγS binding assay is employed for the purposes of this thesis, only this particular method is discussed here.

1.1.4.1 Competition binding assays

Competition binding assays using a radioligand allow the binding affinities of unlabelled compounds to be determined by measuring their ability to displace a fixed concentration of known radiolabelled ligand from the receptor (20). As the level of radioactivity detected is directly proportional to the amount of radioligand that remains bound to the receptor, measurement over a logarithmic range of competing ligand concentrations allow for the plotting of inhibition curves using non-linear regression. The inhibition constant (IC_{50}) from the assay, which is defined as the concentration of ligand that inhibits the binding of the radioligand by 50% and is experiment specific, can then be converted into binding affinity (K_i) using the Cheng-Prusoff equation (21):

$$K_i = \frac{IC_{50}}{1 + \frac{[L]}{K_d}}$$

Equation 1 The Cheng Prusoff equation. *Where K_i is the binding affinity of the ligand, IC_{50} is the experimentally determined inhibition constant, [L] is the radioligand concentration and K_d is the dissociation constant of the radioligand.*

Competition binding assays however provide no information on the binding ligand's functional activity, and other methods must be employed to determine if the ligand is an agonist, neutral antagonist or inverse agonist.

1.1.4.1 [^{35}S]GTPγS binding assay

The [^{35}S]GTPγS binding assay allows for the determination of a ligand's efficacy at GPCRs by measuring the enhancement of GTP binding upon receptor activation (22). [^{35}S]GTPγS is a radiolabelled, non-hydrolyzable analogue of GTP. Upon receptor activation [^{35}S]GTPγS associates with Gα subunit of the G protein, and as it cannot be hydrolysed back to GDP, the G protein heterotrimer cannot reform, resulting in an accumulation of Gα subunits. Measurement of the directly proportional radioactivity allows the % of receptor activation to be calculated; dose response curves can then be plotted in order to determine EC$_{50}$ values. As this assay measures the event directly resultant from ligand-receptor binding, it has an advantage over functional assays which measure other downstream events, such as measurement of intracellular cAMP levels or MAPK phosphorylation, in that it minimizes the effect of signal amplification and interference from other signalling pathways.

Results from [^{35}S]GTPγS binding assays are typically expressed as a percentage of basal binding, with agonists showing a % basal binding over 100%, neutral antagonists showing negligible change in binding, and inverse agonists showing a % basal binding below 100%. Alternatively, results can be expressed as a percentage of the maximum response achieved by a known full agonist under identical conditions, which has the added advantage of providing a clearer indication of the level of agonist activation achieved. In this case full agonists show a response close to 100%, neutral antagonists show a response of 0%, while inverse agonists show a response below 0%.

1.1.5   Challenges in X-ray crystallography of GPCRs

With the continued interest in the GPCRs by both academic and industrial researchers, there has been a need for the three-dimensional structures of these proteins to be elucidated for use in structure-based drug design, virtual screening projects and in studying their structure-function relationships. However, like most membrane proteins, there are several inherent challenges that must be overcome when attempting to crystallize GPCRs for X-ray diffraction (19,23), a typical method of obtaining 3D structures of proteins. In fact, the first crystal structure of a mammalian GPCR, that of bovine rhodopsin, was only solved in the year 2000 (24).

Firstly, GPCRs are generally expressed at low levels in native cells (a notable exception being bovine rhodopsin, which is highly expressed in rod cell disc membranes) (23,25). Recombinant systems developed must therefore be capable of high expression levels and native protein folding (23). Secondly, GPCRs have poor thermodynamic stability during the purification process, and are also prone to proteolysis due to their flexible extramembranous regions (23). Thermodynamic stability has been achieved by methods such as utilizing stabilizing ligands, stabilizing mutations, high salt concentrations, and the addition of lipids during the purification and crystallization process (26–29). Receptor stability and structure resolution has also been enhanced by truncating disordered regions, engineering disulfide bonds between loops, receptor-antibody Fab fragment complex formation, fusion of T4-lysozyme (T4L) with the receptor, and the utilization of nanobodies (26–28,30). Thirdly, once the GPCRs are detergent-solubilized, there are difficulties in growing diffraction quality crystals, owing to their flexible third intracellular loop and C terminus, as well the fact that they lack a considerable exposed polar surface area in order to form crystal lattice contacts (27). The methods developed involving T4L fusion and antibody Fab complexes addressed these issues, stabilizing the receptor and providing the contacts needed for crystallogenesis (26,27,30). Both these approaches also relied on advances in lipid-mediated crystallogenesis, such as bicelle crystallization and lipid mesophase techniques (31,32).

As a result of these new techniques, the crystal structures of GPCRs other than bovine rhodopsin have been solved in recent years, including those of the adrenergic β1 and β2 in 2007, adenosine A2A in 2008, dopamine D3 in 2010, chemokine CXCR4 in 2010, histamine H1 in 2011, nociceptin receptor NOP in 2012, opioid κ, μ, and δ in 2012, muscarinic M2 and M3 in 2012, neurotensin 1 receptors in 2012, protease-activated receptor PAR1 in 2012, sphingosine-1 phosphate S1P1 in 2012, corticotrophin-releasing factor receptor 1 CRF1 in 2013, and glucagon receptor GCG in 2013 (26,28,29,33–45). In addition, the β2 receptor in complex with the Gs protein has also recently been crystalized, representing a major breakthrough in the crystallography of GPCRs (46). These structures, however, still only represent a minute portion of the GPCRs. Due to the costs and time involved in elucidating GPCR structures via X-ray diffraction, coupled with the possibility that techniques such T4L fusion may possibly introduce structural artefacts, protein structure prediction and other computational methods are proving to be a valuable method of producing three-dimensional structures for studying the GPCRs.

1.1.6   GPCR amino acid numbering system

All amino acid residues in GPCRs presented in this thesis are numbered using the system presented by Ballesteros and Weinstein (47). According to this system, each amino acid number begins with the TM helix number in which the amino acid is located, followed by a locant. The most highly conserved residue within that helix is arbitrarily assigned a locant of 50. For example, the most highly conserved residue in TM3 of GPCRs is the arginine in the DRY motif. Consequently, using the Ballesteros-Weinstein system, this arginine is numbered as R3.50, is preceded by D3.49, and followed by Y3.51. Residues located within the extra and intracellular loops are numbered using their global position within the protein amino acid sequence.
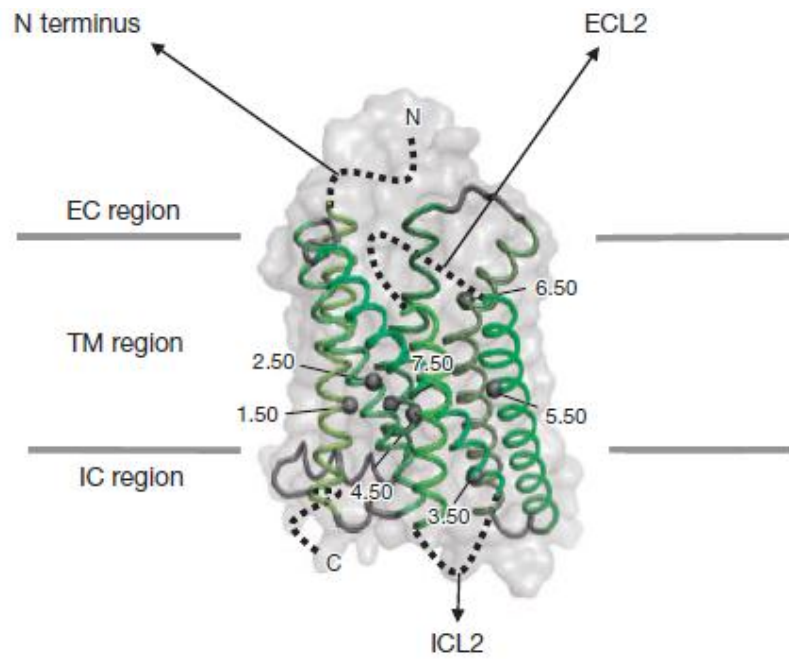
Figure 1-4 Ballesteros Weinstein numbering in GPCRs. Taken from reference (48).

1.2 The cannabinoid receptors CB1 and CB2

1.2.1 Discovery, distribution and classification

Cannabis, also colloquially known as marijuana, hashish or weed, is the name given for preparations derived from the plant *Cannabis sativa* and is one of the most popular illicit drugs used recreationally today, mainly due to its euphoric effects and the ability to alter sensory perception (49). Despite being classified as a substance of abuse in many countries, the diverse properties of this plant on human physiology have been utilized therapeutically for several millennia and are well documented (50).

The bioactive constituents of cannabis, which are lipophilic, were originally thought to act non-specifically via the perturbation of lipids in the cell membrane (51). However, the elucidation of the structure of delta-9-tetrahydrocannabinol **1** (Δ^9-THC) (see Figure 1-5), the main psychoactive constituent of cannabis, whose structure was subsequently used to define the classical cannabinoids, and further studies demonstrating its stereo-selectivity and structural-selectivity led to the view that a distinct receptor existed for Δ^9-THC (52–54). The demonstration of the existence of a saturable, high-affinity stereospecific binding site in the brain of mice for [^{3}H]CP55940 **3** (a synthetic, non-classical cannabinoid) by Devane *et al* in 1988 provided definite evidence of the existence of this then unknown receptor (55). Further research in this area finally led to the identification of an orphan GPCR in the brain that bound the cannabinoids, and this GPCR was subsequently termed cannabinoid receptor CB1 (56). While being most abundant in the human brain, CB1 receptors have since been shown to also be present in peripheral, metabolically-relevant tissues such as liver, skeletal muscle, adipose tissue, and pancreas, albeit at lower concentrations (57–60). This was subsequently followed by the identification of a second cannabinoid receptor, termed CB2, which is expressed mainly in the cells of the immune and haematopoetic systems, but is also found in the brain, adipose tissue, skeletal muscle, and pancreas (58,61–63). In recent years there have been

pharmacological studies suggesting the existence of a third cannabinoid receptor, among the possible candidates being the orphan receptor GPR55, although this view is controversial, and based on current evidence, no receptor other than CB1 and CB2 fits all the criteria to be classified as a novel cannabinoid receptor (64).
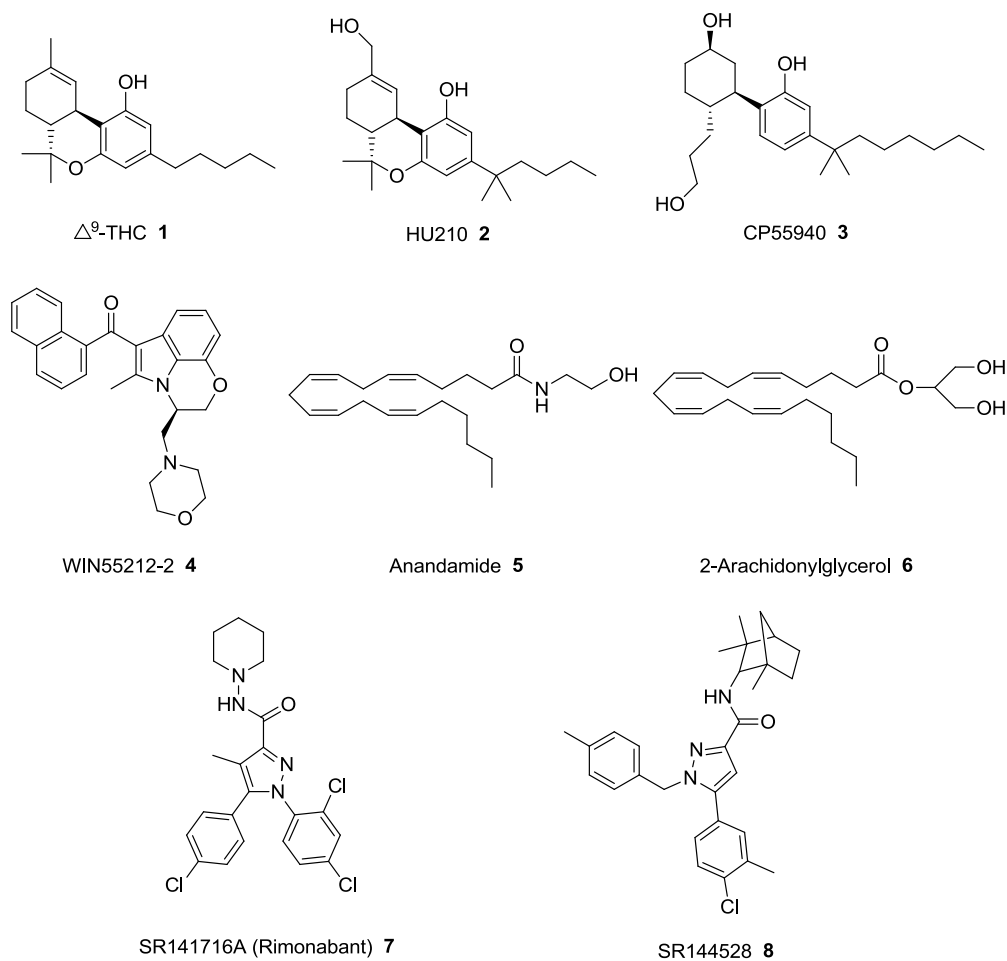
Figure 1-5 Selected cannabinoid receptor ligands. *(A) Classical cannabinoids Δ^9 –THC and HU210. (B) Non-classical cannabinoid CP55940. (C) Aminoakylindole agonist WIN5521202. (D) Endogenous cannabinoids anandamide and 2-AG. (E) CB1 selective antagonist SR141716A. (F) CB2 selective antagonist SR144528*

In Fredriksson *et al*'s paper, the CB1 and CB2 receptors are classified as belonging to the α-group in the rhodopsin family of GPCRs, putting them in the same receptor cluster as the melanocortin receptors, endothelial differentiation GPCRs, and adenosine receptors (1). Interestingly, the CB1 and CB2 receptors themselves only show 44% sequence homology between themselves overall, with this figure rising to 68% if only the transmembrane regions are taken into account (61).

1.2.2   Endogenous cannabinoids

Simultaneous with the discovery of the cannabinoid receptors, proof of the existence of an endogenous ligand was provided following the isolation of anandamide from porcine brain tissue (65). Anandamide **5** has been shown to be a CB1 selective ligand, where it displays partial or full agonist activity (66). Anandamide is mainly synthesized *in vivo* from the membrane lipid precursor N-arachidonoylphosphatidylethanolamide (NAPE) utilizing a pathway involving phospholipase D, and degraded by fatty acid amide hydrolase (FAAH), though other parallel pathways may exist (67,68). The isolation of anandamide was followed by the discovery of 2-arachidonoylglycerol **6** (2-AG), the second endocannabinoid. 2-AG is synthesized *in vivo* from diacylglycerol (DAG) via the enzyme DAG lipase (69,70). While anandamide and 2-AG represent the endocannabinoids predominantly present in the brain, several other endocannabinoids of the eicosanoid class have also been shown to exist, namely 2-arachidonoyl glycerol ether, O-arachidonoylethanolamie (virodhamine), and N-arachidonoyl dopamine (71–74). These lipid-derived, highly lipophilic ligands, were found to be structurally distinct from the first cannabinoid ligands described, which were mainly synthetic analogues that followed the discovery of Δ^9-THC (such as the classical cannabinoid HU210 **2**, non-classical cannabinoid CP55940 **3**, and the aminoakylindole WIN

55212-2 **4**), an early indicator of the diversity of ligands capable of binding to the cannabinoid receptors.

1.2.3   Cannabinoid receptor signalling

As expected of GPCRs, signal transduction of the cannabinoid receptors is complex but occurs mainly through G proteins, specifically the G_i subtype (75). As such, activation of the cannabinoid receptors leads to an inhibition of adenylyl cyclase and a decrease in cellular cAMP levels in a pertussis toxin-sensitive manner. Some studies have also shown the cannabinoid receptors to be capable of stimulating cAMP production to some degree, with proposed mechanisms for this activity including production of another endogenous activator of adenylyl cyclase such as prostaglandin, augmentation of G_s activity and activation of isoforms 2/4/7 of adenylyl cyclase via G$\beta\gamma$ dimers uncoupled from G_i and direct interaction with G_s (76–81). Additionally, the cannabinoid receptors have been shown to signal through many of the non-G protein pathways described earlier that will not be discussed here, but is subject to a review by A.C Howlett (82).

1.2.4   Therapeutic potential of targeting the cannabinoid receptors

The cannabinoid receptors and their distribution throughout the human body result in their contribution in the regulation of a variety of physiological processes as well as the pathology of many disease states. As such, over the years *in vitro* assays, animal studies and clinical trials have highlighted a multitude of pathophysiological conditions where pharmacotherapy targeting either one or both cannabinoid receptors may potentially be of benefit. These diseases include:

- Obesity and other related metabolic disorders

- Anorexia and cachexia

- Pain and inflammation

- Stroke and neurotoxicity

- Multiple sclerosis

- Movement disorders such as Parkinson's disease, drug-induced dyskinesia, Huntington's disease, Tourette's syndrome, and tardive dyskinesia.

- Alzheimer's disease

- Amyotrophic lateral sclerosis

- Epilepsy

- Anxiety and depression

- Schizophrenia

- Insomnia

- Drug or alcohol addiction

- Nausea and emesis

- Cardiovascular diseases such as hypertension, atherosclerosis, myocardial reperfusion injury, and circulatory shock

- Asthma

- Glaucoma and retinopathy

- Cancer

- Hepatitis and liver cirrhosis

- Inflammatory bowel disease

- Arthritis

- Osteoporosis

It is clear from the length of this list that pharmacological modulation of the endocannabinoid system possesses substantial therapeutic potential. As a full discussion regarding all the diseases listed is beyond the scope of this thesis, the focus here will be on conditions in which drugs targeting the cannabinoid receptors have successfully entered Phase III clinical trials or gained regulatory approval. Readers who are interested in obtaining more information on the role of cannabinoids in all of the conditions listed are directed to an excellent review by Pacher *et al* (83), from which the above list is derived.

1.2.4.1 Obesity and related metabolic disorders

It has been known for many years that the use of cannabis increases appetite and can cause significant weight gain, and following further study the orexigenic (i.e. appetite stimulating) properties of Δ^9-THC was experimentally demonstrated (84). As such, the role of the endocannabinoid system in regulating appetite centrally and via peripheral energy metabolism has been a main focus of research over the years. Studies have revealed that the endocannabinoid system modulates feeding centrally through decreasing satiety signals, enhancing orexigenic signals, as well as increasing eating motivation through reward mechanisms involving the mesolimbic pathway (reviewed in (85) and (86)). Peripherally, the endocannabinoid system modulates energy expenditure, and it has been shown that CB1 knockout mice are resistant to

obesity induced by diet and have increased energy expenditure (59,87). Treatment of diet-induced obese mice with the CB1 inverse agonist SR141716A **7** (rimonabant) showed a reduction in food intake that was transitionary in nature (suggesting tolerance to the central effects of rimonabant), but a reduction in body weight that was sustained, highlighting the importance of increased peripheral energy expenditure in the response (88). As overactivity of the endocannabinoid system has been implicated in clinical obesity, with obese patients showing elevated endocannabinoid levels in the adipose tissues, it followed that treatment with a CB1 antagonist/inverse agonist had potential clinical benefit (89). Consequently, rimonabant was further developed by Sanofi-Aventis as an anti-obesity agent under the trade name Acomplia®.

Four clinical trials involving rimonabant, known as the RIO (*R*imonabant *I*n *O*besity) trials, showed that administration of rimonabant was associated with a reduction in body weight that was sustained as long as treatment was continued, decreased plasma glucose and insulin levels, as well as improvements in the lipid profiles of patients as demonstrated by a decrease in plasma triglycerides and an increase in high-density lipoprotein (HDL) cholesterol levels (90–93). Following these trials the European Medicines Agency (EMEA) approved Acomplia® in 2006 for the treatment of overweight and obese patients, defined as patients with Body Mass Index > 27kg/m^2, who have associated risk factors such as type 2 diabetes and dyslipidaemia.

Unfortunately, rimonabant failed to gain regulatory approval from the U.S Food and Drug Administration (FDA), due to concerns over psychiatric adverse events associated with its use that were inadequately highlighted in the RIO trials, such as depression, agitation, anxiety, seizures, and suicidal ideation (94). Post-marketing safety data led to the EMEA voicing the same concerns, and sales of Acomplia® were suspended in October 2008, with approval of rimonabant finally withdrawn in January 2009 (95). The fallout of this incident led to discontinuation of several other CB1 antagonists/inverse agonists in clinical research, such as SR147778 **9** (surinabant), MK0364 **10** (taranabant), and CP945598 **11** (otenabant) (Figure 1-6).

Surinabant **9** Taranabant **10** Otenabant **11**
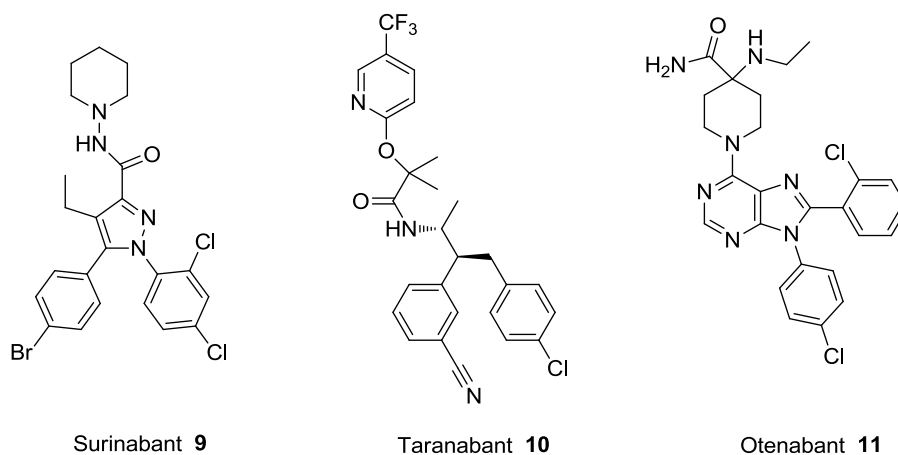
Figure 1-6 Selective CB1 inverse agonists whose development have been discontinued

While CB1 antagonists/inverse agonists have failed to succeed as anti-obesity agents, the cannabinoid receptor agonist Δ^9-THC (dronabinol) has been licensed as an appetite stimulant in AIDS patients, and is marketed as Marinol®.

1.2.4.2 Chemotherapy-induced nausea and vomiting

Chemotherapy-induced nausea and vomiting (CINV) is one of the most prevalent side-effects of current cancer-treatment regimens, and also one of the most debilitating. The pathophysiology of emesis is complex, involving multiple neurotransmitters in the gut and chemoreceptor trigger zone at the base of the brain (96). The pharmacological mechanism of cannabinoids' anti-emetic properties are still unclear, but is hypothesized to possibly include an interaction with 5-HT$_3$ receptors (one of the most prominent receptors implicated in emesis) on GABAergic neurons, where they mediate opposing effects on GABA release (97). There is also evidence that CB1 receptors located in the brainstem region control the vomiting reflex, while endocannabinoids in the gastrointestinal tract have a physiological role in emesis (98). Several small studies and case reports over the years have established the place of cannabinoids as a valuable option in CINV and

palliative care. A meta-analysis of 30 of these studies conducted by Tramer *et al*, with a total sample size of 1366 patients, concluded that the cannabinoids were slightly more effective than conventional anti-emetics, with higher patient preference due to their euphoric and sedating properties (99). However, the associated psychiatric adverse effects would limit their use as a first line agent.

As such, dronabinol and other cannabinoids have over the years gained acceptance as an anti-emetic in CINV, particularly when first line agents are inefficacious. Dronabinol (Marinol[®]), its synthetic analogue nabilone **12** (Cesamet[®]), and Sativex[®], a cannabis-based preparation consisting of equal amounts of Δ^9-THC and cannabidiol **13** (a non-psychoactive plant cannabinoid), have all been licensed for the suppression of nausea and vomiting associated with chemotherapy.

Nabilone **12**   Cannabidiol **13**
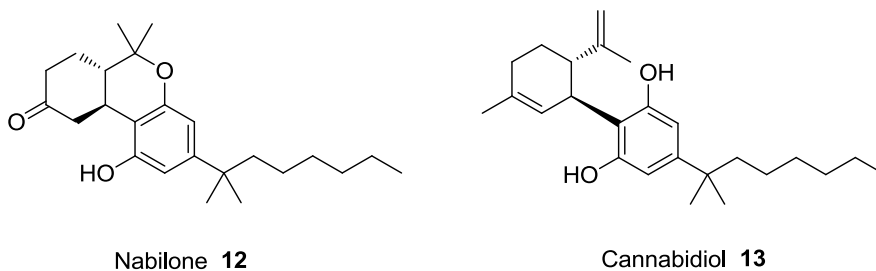
Figure 1-7 Structures of nabilone and cannabidiol

1.2.4.3 Multiple sclerosis and neuropathic pain

Multiple sclerosis (MS) is an autoimmune, inflammatory disease which results in loss of the myelin sheath of neurons in the central nervous system, leading to a range of clinical symptoms that include painful muscle spasms, ataxia, paralysis, cognitive impairment, visual disturbances, incontinence, and constipation (100,101). Due to the complex nature of the neuronal system, symptoms frequently vary, relapse and remit. In particular, muscle spasticity and neuropathic pain constantly lead to reduced mobility, patient distress, and a reduction in quality of life (101). Drugs

targeting the immune system in order to slow progression of the disease remain moderately effective at best, and treatment tends to be primarily symptomatic (102).

Early animal models designed to mimic the pathology of MS have found that administration of cannabinoid receptor agonists such as Δ^9-THC, WIN 55212-2, JWH-133 **14** and methanandamide **15** reduced muscle spasticity and tremor, whereas cannabinoid receptor antagonists exacerbated these symptoms (103). A possible explanation for these findings was offered when it was found that the endocannabinoid system is highly activated in MS patients, suggesting an autoprotective role of the endocannabinoids via a negative feedback loop (104).

JWH-133 **14**   Methanandamide **15**
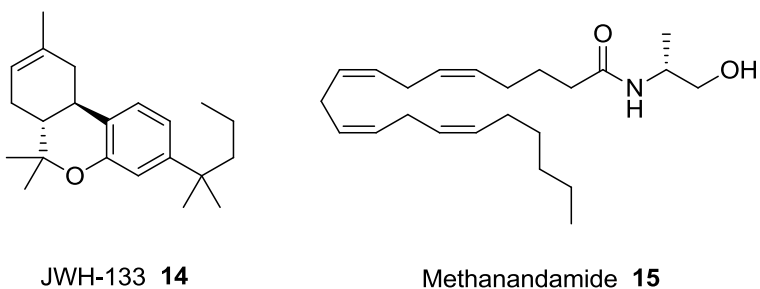
Figure 1-8 Structures of JWH-133 and methanandamide

Subsequently, cannabis extracts began to be the subject of studies involving MS patients, although most of these studies had extremely small sample sizes due to the rarity of the disease. However, one large multi-centre study involving 660 patients, found that after 15 weeks, treatment of MS patients with cannabinoids resulted in no change in Ashworth scores (a score measuring muscle spasticity), tremor, depression, or tiredness (105). On the other hand, significant improvements were found in patient-reported pain, spasticity and sleep quality. Interestingly, the treatment group also showed a reduction in hospital admissions for relapse. A 12-month follow up showed more promising results, with the treatment group showing marked improvements in Ashworth scores (106). A meta-analysis conducted in 2007 by Iskedjian *et al* supported these

findings, concluding that cannabis based treatments were effective in neuropathic and multiple-sclerosis related pain (107).

Sativex® has since been licensed for the symptomatic treatment of neuropathic pain associated with multiple sclerosis and as an adjunctive analgesic in cancer patients (108). Trials studying the use of cannabinoids for the treatment of pain in other conditions are ongoing.

1.2.5 Emerging strategies in targeting the cannabinoid receptors

The lessons learnt in the marketing authorization withdrawal of rimonabant have led to proposed solutions to circumvent the psychiatric adverse events mediated by CB1 receptors in the central nervous system (CNS). Among the possible alternatives, as discussed in a review by R.G Pertwee, are developing neutral antagonists, developing peripherally-restricted ligands that are incapable of crossing the blood brain barrier, selective targeting of the CB2 receptors, targeting particular tissues expressing the cannabinoid receptors, targeting up-regulated receptors, and exploiting the ability of the endocannabinoid system to interact synergistically with other receptors and ligands (108). Several of these strategies could potentially be achieved by the rational design of novel cannabinoid receptor ligands.

The development of a neutral antagonist would likely allow for the beneficial effects of CB1 blockade without compromising central constitutive activity, thus theoretically allowing for a reduction in psychiatric adverse effects. In a similar manner, the development of ligands that retain potency and are less lipophilic, and thus unable to cross the blood-brain barrier, would achieve the same result. Indeed, preclinical evidence demonstrating the viability of this approach has already been presented by Dziadulewicz *et al*, who developed a potent, orally bioavailable, cannabinoid receptor agonist that was capable of producing analgesic activity with limited CNS penetration in animal models of neuropathic pain (109).

Currently, none of the CB2 selective agonists available are entirely CB2-specific, and only show selectivity within a finite dose range (108). Agonists of the CB2 receptor have also been shown to display analgesic activity in many models of acute, neuropathic, inflammatory, cancer-related, and post-operative pain (reviewed in reference (110) and (111)). It has been demonstrated that CB2-selective agonists are capable of producing these anti-nociceptive effects at doses that do not result in observable central CB1-related effects (110,111). While other factors, such as the CB1 to CB2 receptor expression ratio may affect the dose required to achieve this effect, the development of highly selective CB2 agonists would significantly improve the range of this therapeutic window (108). The development of novel CB2-selective agonists has been a focal point of research in recent years, with new scaffolds based on 4-oxo-1,4-dihydroquinoline-3-carboxamide (112), 1,8-napththyridine-4(1H)-one-3-carboxamide (113,114), 4-quinolone-3-carboxylic acid (115), and oxazinoquinolone motifs (116,117) being described. While some of these relatively new compounds have shown promise, such as GW842166X **16** which is currently in clinical development for the treatment of inflammatory pain (118), there is still a need for novel leads targeting the cannabinoid receptors.
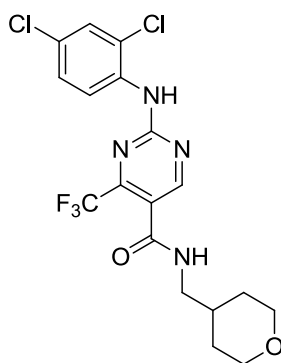
GW842166X **16**

Figure 1-9 Structure of GW842166X

The ability of cannabinoid receptor ligands to interact with other receptors, such as the vanniloid TRPV1 receptor, may also be potentially exploited therapeutically via the development of

a single ligand that targets both receptors. One such ligand, which acts as both a CB2 receptor inverse agonist and a TRPV1 receptor agonist, has already been developed, and has been proposed to possess potential anti-inflammatory activity (119). The plant cannabinoid Δ^9-tetrahydrocannabivarin has also been shown to simultaneously activate CB2 receptors and block CB1 receptors, a combination that could be beneficial in the treatment of stroke and chronic liver diseases (108,120). Other receptors, such as the peroxisome proliferator-activated receptors (PPAR) have also been shown to be activated by anandamide (121). These examples thus highlight the potential of the development of cannabinoid ligands that affect multiple targets.

These strategies emphasize the unmet need for novel compounds targeting the cannabinoid receptors. A better understanding of the cannabinoid receptors, their structure-function relationships, their interaction with ligands, and the principles which govern receptor selectivity would therefore allow for the rational design of ligands capable of achieving the above.

1.3   Molecular modelling of the cannabinoid receptors

To date, the crystal structure of both cannabinoid receptors remains unsolved. As such, over the years numerous homology models of the cannabinoid receptors have been used in order to study these receptors at an atomistic level. This chapter serves to highlight some of the many successful applications of molecular modelling of the cannabinoid receptors, beginning with a discussion on the key concepts of molecular modelling techniques.

1.3.1   Key concepts in molecular modelling

1.3.1.1 Homology modelling

The three-dimensional structures of proteins are traditionally deduced experimentally using spectroscopic methods such as NMR and X-ray crystallography before being deposited in repositories such as the Protein Data Bank (PDB) (122). As of August 2013, the PDB contained approximately 86,000 protein structures, although the actual number of unique protein structures is much lower as the PBD contains multiple entries for the same protein determined under differing conditions and resolutions. The gap between the number of unique protein sequences known and structures solved continues to widen however, due to the disproportionate resources and time required for each task; the generation of diffraction-quality crystals of certain proteins (particularly membrane proteins) remains the primary bottleneck in the structure-elucidation process (123). As such, various computational methods allowing for the prediction of 3D models of proteins for which experimental structures are absent have in recent years become invaluable in bridging this gap, with such structure prediction methods being collectively known as homology modelling.

Homology modelling can be defined at an elementary level as the prediction of the three-dimensional structure of a protein for which its sequence but not structure is known, using its alignment to a homologous (related) protein whose structure has been experimentally determined (124). While various methods for the homology modelling of a particular target exist, the general

principles and processes remain similar: a suitable template is selected, an alignment between target and template is determined, an initial model is constructed, the model is refined and validated, and the process is reiterated until an acceptable model is generated.
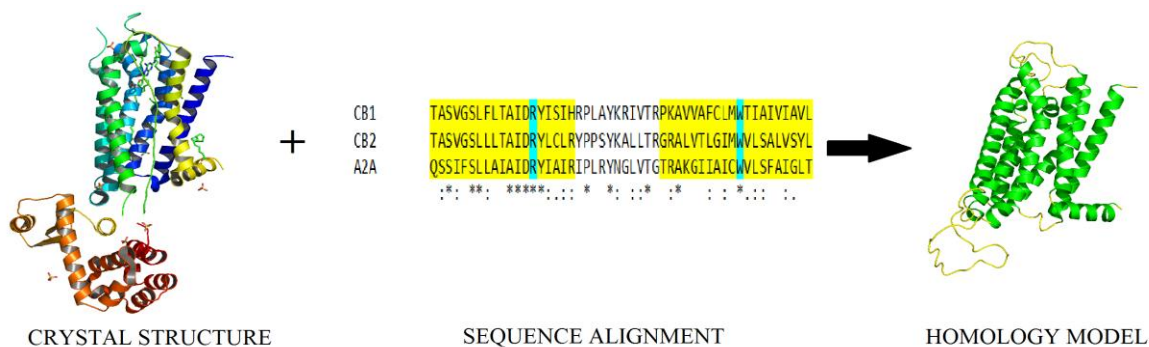
Figure 1-10 General process of homology modelling.

The selection of a suitable structural template is typically done by utilizing specific sequence alignment algorithms such as BLAST (125) or PSI-BLAST (126) to search databases such as the PDB for structures which are related in sequence to the target protein. If the protein family of the target is already known (e.g. if the target is known to be a GPCR), the field of search can be narrowed down substantially by performing sequence alignments only against structures in the same protein family to find the template with the highest sequence identity to the target, though other factors such as the X-ray resolution may play a role in template selection. The use of multiple templates may also be beneficial in cases of low sequence identity, though this effect is primarily due only to an improvement in the sequence alignment between target and template (127).

Following the identification of a suitable template or templates, most sequence alignments produced during the initial screen will require some form of refinement. Sequence alignment remains the one of the most crucial steps in homology modelling as any error in alignment would be subsequently amplified. The chance of such errors can be minimized via the utilization of

multiple sequence alignments and a knowledge-based approach when refining the initial alignment. Multiple sequence alignments allow for the delineation of strongly divergent areas in the sequences, where mutations resulting in amino acid insertions and deletions are more likely to occur. If the general fold of the protein family is known, areas where gaps in the sequence alignment are less likely to occur may have been previously identified, for example in the hydrophobic core of transmembrane proteins, and such information may be used to manually improve any algorithm-generated alignment.

An initial model can then be constructed using this alignment, and while various programs exist for this task models are generally constructed in the same manner; residues in the template are replaced by the target residues using the same protein backbone coordinates, with only the side chains being varied. The model is then refined to minimize any high energy clashes that may have been generated in this process. At this stage the model is normally checked for structural integrity via visual inspection and comparison with known crystal structures through methods such as Ramachandran plots, which compares the amide bond φ and ψ angles of the model against 118 proteins with known crystal structures of resolution 2.0 Å or better (128,129). An example of a Ramachandran plot is shown in Figure 1-11.
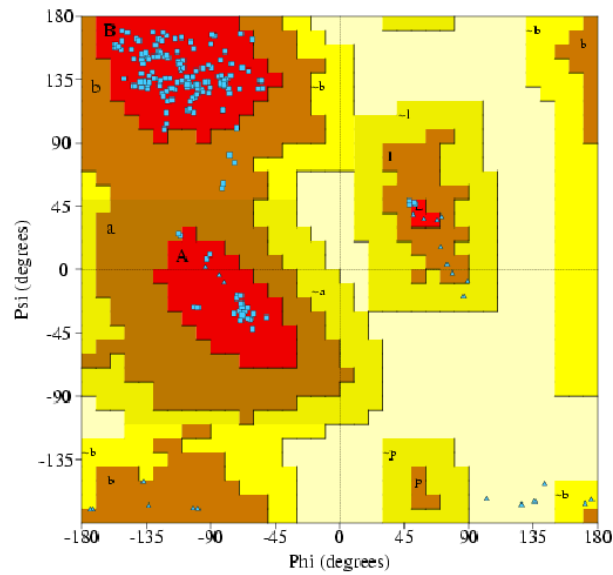
Figure 1-11 A typical Ramachandran plot. *The contours on the plot were derived from the φ and ψ angles of 118 protein crystal structures. The red, yellow, beige, and white regions represent the most favoured, additionally allowed, generously allowed and disallowed regions respectively.*

The precise backbone conformation, side chain rotamers, and hydrogen-bonding networks in this initial model are however, broadly similar to the template and likely inaccurate. While there are many more paths leading away from the desired target state than towards it, in recent years models typically undergo refinement and optimization using various methods, the most prominent of which are molecular dynamics and Monte Carlo simulations due to increasing force field accuracy, sampling efficiency, and computational capability (124,130,131).

The refined model can then be validated or evaluated based on its intended use, usually via the reproduction of known experimental data. In typical drug discovery applications, the model may be evaluated through docking and predicting the binding affinities and interactions of known ligands, or used to screen a virtual library of known ligands and decoy molecules in order to obtain an enrichment factor or Receiver Operating Characteristic (ROC) curve, which measures the ability of a particular virtual screening protocol to select active compounds when compared to random

screening (132). ROC curves have several advantages over conventional enrichment curves (which plot the fraction of actives found against the fraction of database screened), one in particular is that they are independent of the rate of active molecules in the sample set (133). If the evaluated model is unable to produce the desired outcome, the process can be reiterated; with a different model selected and the evaluated until a satisfactory model that is deemed to be representative of the target is obtained.

1.3.1.2 Molecular dynamics and empirical force fields

Three-dimensional models of a protein obtained through either crystallographic techniques or homology modelling can provide useful information regarding its structure. However, these static representations merely represent one possible conformation of an ensemble, as proteins in real biological systems are dynamic in nature (134). Homology models, particularly those with low sequence identities, may also be in non-native conformations that are similar to their templates, necessitating refinement. Molecular dynamics (MD) represents one of the most prominent methods in computer simulations of biological macromolecules to address these issues, allowing for the study of a wide range of system properties and behaviour based on the principle that these properties can all be derived from the interactions between atoms in the studied system (135).

MD simulations generate successive configurations of a system by solving Newton's equations of motion (135). By taking into account the interaction energy between all atoms in the system, the force acting on each individual atom is derived, and their new coordinates after a fixed time step (typically 1 or 2fs) is calculated. This process is repeated several million times in order to generate a trajectory from which system properties and behaviour can be studied. In the context of a receptor-ligand system, these trajectories can be used to sample receptor conformations, deduce key

amino acid residues, investigate ligand binding and approximate ligand binding affinity via the derivation of the free energy of binding, as well as to probe receptor activation mechanisms.

The interactions between all the atoms in a system, and correspondingly the forces they experience at each successive time step, are governed by a pre-defined set of equations known as a force field (136). These empirical (electronic effects are ignored and interactions are calculated based only on nuclear positions) force fields typically have the following functional form:

$$V(\bar{r}) = \sum_{\text{bonds}} K_b(b - b_0)^2 + \sum_{\text{angles}} K_\theta(\theta - \theta_o)^2 + \sum_{\text{dihedrals}} K_\chi(1 + \cos(n\chi - \delta))$$

$$+ \sum_{\text{nonbonded-pairs},i,j} \left[\frac{q_i q_j}{4\pi e_o r_{ij}} - \varepsilon_{ij} \left\{ \left(\frac{R_{\min ij}}{r_{ij}} \right)^{12} - 2 \left(\frac{R_{\min ij}}{r_{ij}} \right)^6 \right\} \right]$$

Equation 2 General form of an empirical force field

Interactions are generally divided into bonded (bonds, angles and dihedrals) and non-bonded (electrostatic and Van der Waals) interactions. Bonded interactions such as bonds and angles are treated as simple springs governed by Hooke's Law while dihedrals are governed by a sinusoidal function. Non-bonded interactions are modelled using a 12-6 Lennard-Jones potential for van der Waals interactions and a Coulombic potential for electrostatic interactions (137). Numerous force fields exist that differ mainly in the way these equations are parameterized and the experimental data in which they are validated against; well-known examples being the CHARMM, AMBER, and GROMOS force fields (138–140).

The scope of feasible simulations using MD is limited primarily by two factors, namely force field accuracy and computational demand (137). While force fields have been constantly refined over the past two decades to include different classes of molecules and validated using

various methods, there is still room for improvement, and the result of any simulation has to take into context known experimental data. The availability of computing power limits most simulations for large systems such as membrane proteins to several hundred nanoseconds, but many biological processes of interest such as receptor activation take place on the micro- to millisecond time scale, which is unachievable by most research groups that are without access to specialized supercomputers such as Anton (141).

1.3.1.3 Automated docking

In the context of virtual high throughput screening or structure-based drug design projects, the primary aim is typically to either identify potential leads from small molecule databases or to predict the binding mode of a particular class of ligands to its receptor. The large number of ligands to be processed in both cases necessitates a method that is computationally inexpensive without compromising prediction accuracy. Docking remains the primary method used to achieve these goals.

On a fundamental level, docking can be defined as a computational technique that is used to predict the binding conformation and binding affinity of a ligand to its receptor (135,142). When a series of ligands is docked successively, the ligands can be ranked according to their predicted binding affinities, allowing the identification of potential lead molecules. While the exact method may differ, most docking programs typically combine a search algorithm and a scoring function (see Figure 1-12). Using a representation of the receptor (derived from X-ray structures or homology models), the search algorithm first generates possible conformations of the ligand within a defined binding site. Methods for conformational sampling of the ligands vary from incremental construction to genetic algorithms and Monte Carlo methods, and normally incorporate biases or local search methods such that the attributes of energetically favourable conformations are kept in

successive conformations (142).   Each conformation is then scored based on the energetics between ligand and receptor, and the conformations ranked in order to provide a best prediction of the binding mode and binding affinity.
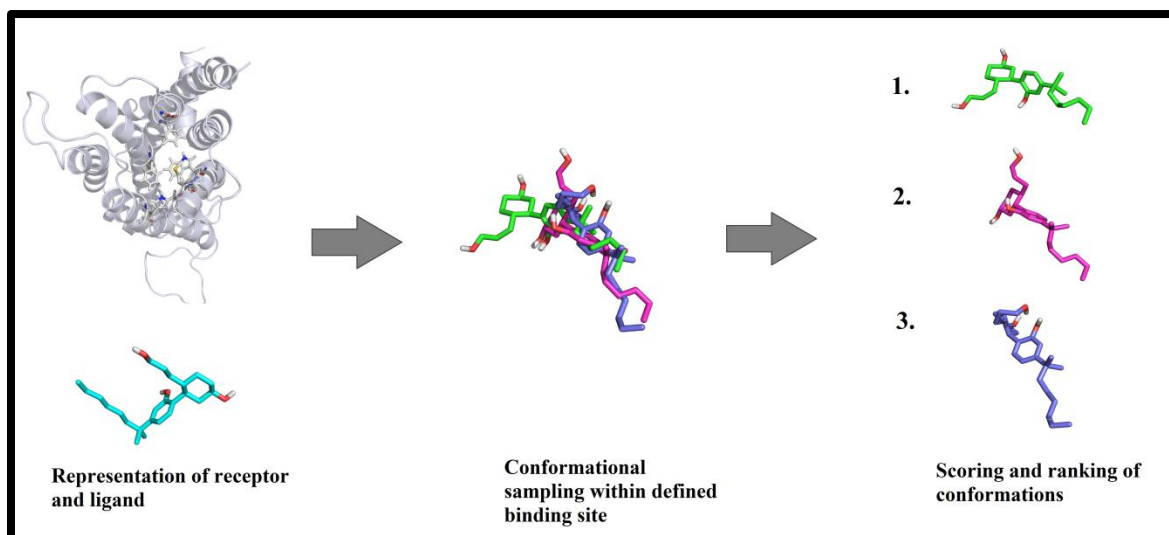
Figure 1-12 General process of computational docking.

The challenges in computational docking are well documented, the most prominent of which involve current empirical scoring functions which are unable to account fully for entropic and solvation effects and may perform poorly in estimating exact binding affinities when evaluated over a large sample of diverse protein-ligand complexes (142,143). Various studies comparing current scoring functions have concluded in general that they perform better in identifying correct binding poses in protein-ligand complexes than estimating binding affinities, and that no one single scoring function outperforms the others in all cases, though consensus scoring may be of some value (143–148). Other challenges such as the accuracy of the receptor model (particularly homology models) and the incorporation of receptor flexibility without increasing computational cost may further influence results, and thus hypotheses-driven approaches utilizing available experimental information about the target are invaluable in analysing the results of any docking study (142,149)

1.3.2 Molecular modelling studies of the cannabinoid receptors

These studies are broadly divided into two categories: (i) primarily computational studies which are typically used to investigate receptor structure, deduce ligand binding, and for virtual screening, and (ii) studies complementing mutagenesis and pharmacological investigations.

1.3.2.1 Computational studies elucidating receptor structure and ligand binding

The first homology model of the cannabinoid receptors was described by Bramblett *et al* in 1995, where the authors used a variety of methods such as hydrophobic and variability moment vectors to identify the transmembrane helices of the CB1 receptor and delineate the orientation of each helix within the lipid membrane. A tentative helix bundle arrangement was then obtained that was consistent with the then-proposed helix arrangement of rhodopsin (150). Mahmoudian *et al* subsequently constructed a model of CB1 with the transmembrane helices based on the electron density map of bacteriorhodopsin, which is a seven-transmembrane protein but not a GPCR, and refined the model using energy minimization and molecular dynamics with the CHARMm forcefield. AUTODOCK was then used to dock Δ^9-THC into this model and a binding site for this ligand was proposed (151).

Following the release of the crystal structure of bovine rhodopsin, Xie *et al* constructed a model of the CB2 receptor utilizing the aforementioned crystal structure as a template for the transmembrane regions (152). A multiple sequence alignment involving ten GPCRs was used, and the loop regions were generated by searching the Protein Data Bank (PDB) for homologous Cα backbone sequences (122). Residue side chains were positioned using rotamer library searches, minimization and simulated annealing methods. This model was then used to identify helix tilt angles, conserved residues, hydrogen-bond networks, and potential disulfide bonds.

Shim *et al* constructed a model of the CB1 receptor based on bovine rhodopsin in order to study the binding of several non-classical cannabinoid agonists (153). A docking method combining Monte Carlo and molecular dynamics simulations highlighted two possible binding conformations based on the placement of the ligand. The authors then proposed one conformation as being more probable, based on calculated binding energies and their correlation with experimental data, and proceeded to identify key interacting residues.

The high levels of constitutive activity of the CB1 receptor was studied by Singh *et al*, who following comparison of CB1 with rhodopsin, hypothesized that this was due to the lack of aromatic residues around the key residue W6.48 (154). Employing a biased Monte Carlo method known as Conformational Memories, the authors showed that W6.48 in CB1 had greater conformational flexibility, and that F3.36 helps constrain W6.48 in the inactive state, leading to the suggestion of a W6.48/F3.36 'toggle switch' for cannabinoid receptor activation. These findings were subsequently supported in a study by Latek *et al*, whose docking of agonists and antagonists to CB1 and CB2 models predicted binding in which the ligand type matched the state of this rotamer toggle switch; agonists changed the state of the switch while antagonists maintained it (155).

Utilizing these findings regarding this interaction and others involving the β2 adrenoceptor, Tuccinardi *et al* modified inactive state models of the CB1 and CB2 receptors by adjusting the conformation of the toggle switch, rotating TM3 and TM6, and straightening TM6 (156). The resultant 'active state' models were subjected to docking analysis with the agonist WIN55212-2 in order to study CB2/CB1 selectivity. Further docking of several other ligands into the CB2 model produced a good correlation between experimental and estimated binding energies, confirming its reliability. This validated model was subsequently used by Durdagi *et al* to study conformations of the synthetic cannabinoid AMG3 **17** in solution and in the binding pocket (157). A follow-up study, where homology models constructed using the β2 adrenergic receptor were compared with the rhodopsin-based models, confirmed the ligand binding pocket that was previously derived (158).
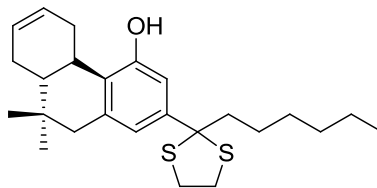
AMG3 **17**

Figure 1-13 Structure of synthetic cannabinoid AMG3

Another successful example of the modelling of an 'active state' cannabinoid receptor based on the modification of an inactive state model was shown by Renault *et al* (159). By rotating the TM6 of their inactive state model, an active state model was produced following docking and MD with a known agonist. A 2D ligand-based Bayesian network was then computed to enrich a commercial library for virtual screening using their model and a consensus scoring approach. The selection of 150 compounds from the top 1% of the compounds screened resulted in 13 compounds showing good binding to the CB2 receptor in pharmacological assays, the majority of which behaved as agonists and included two novel full agonists. This select discovery of agonists demonstrated the validity of their active state model for the subsequent identification of key interactions in agonist binding.

While most homology models have focused on the TM region in which the majority of the key ligand interactions occur, Shim *et al* have previously examined the role of the second extracellular loop E2 in CB1 receptor ligand binding (160). Using a combination of secondary structure prediction algorithms and molecular dynamics with simulated annealing, the authors determined the structures of E2 taking into consideration different oxidation states of two key cysteine residues within the loop. Distinct E2 structures were found to interact differently with the TM helices and had a significant effect on the binding site topology. The more biologically-relevant disulphide form of E2 was found to favour an agonist bound state, while the dithiol form favoured antagonist binding, revealing the possible significance of this loop in stabilizing receptor structure.

One particularly ambitious study by Hurst *et al* sought to test the hypothesis that the endogenous cannabinoid 2-AG gains access to the binding site of the CB2 receptor via the lipid bilayer (161). To achieve this, the authors employed an all-atom molecular dynamics simulation of 2-AG and the CB2 receptor embedded in a palmitoyl-oleoyl-phosphatidylcholine (POPC) lipid bilayer in the microsecond time scale. The resulting trajectories suggested that 2-AG is able to enter the receptor binding pocket by partitioning out of the bulk lipid and passing through the TM6/TM7 interface. Following entry of the 2-AG headgroup into the binding pocket, the intracellular ionic lock between TM3 and TM6 is broken, leading to inter-helical motions that are associated with receptor activation. Subsequently, D3.49/D6.30 protonation and further ligand entry into the binding pocket results in a change in W6.48 toggle switch conformation and an influx of water. This elaborate study represented the first demonstration via molecular dynamics simulations of a ligand accessing the binding pocket of a GPCR via the lipid bilayer and triggering receptor activation.

More recently, Cichero *et al* combined typical homology modelling and docking methods with 3D-QSAR analyses to depict the agonist binding site of the CB2 receptor and guide design of a series of CB2-binding indol-3-yl-tetramethylcyclopropyl ketone derivatives (162). A theoretical model based on the β2 adrenoceptor crystal structure was employed for the docking and MD of WIN55212-2 to identify key interactions for agonist binding. The subsequent docking of the novel class of agonists and Comparative Molecular Fields Analysis (CoMFA) and Comparative Molecular Similarity Indices Analysis (CoMSIA) resulted in a highly predictive model and the derivation of guidelines in the synthesis of indoles showing high CB2 affinity.

Taking into account that CB1 ligands are structurally diverse, Ai *et al* studied the hypothesis that the CB1 receptor may undergo significant conformational changes to accept different ligands (163). Four CB1 receptor models were constructed based on four distinct ligands (HU210, arachidonyl-2-chloroethylamide **18** (ACEA), WIN55212-2 and SR141716A) and two

crystal structures (β2 adrenoceptor and adenosine A2A). The models were optimized using molecular dynamics simulations, and were subjected to a docking analysis using known binders, structurally similar binders, and random compounds. Their results indicated that while each model was able to accept most CB1 ligands as the binding site remained similar, the key interactions derived from each model varied slightly according to the class of ligand the model was based upon. Thus, the authors concluded that models optimized for a particular ligand class may be more accurate in virtual screening.
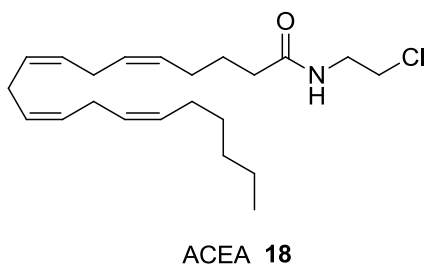
ACEA **18**

Figure 1-14 Structure of ACEA

1.3.2.2 Modelling studies complementing pharmacological data

Homology models of the cannabinoid receptors are being increasingly used in conjunction with experimental mutagenesis data in order to form hypotheses regarding aspects of cannabinoid receptor function and ligand binding. In some studies, computational models of the cannabinoid receptors have been used to explain the findings of mutagenesis experiments in more detail. The reverse is also true, as computational models have also been used to highlight potential residues of interest for mutagenesis studies.

Tao *et al* investigated the fact that mutation of the conserved lysine K3.28 in CB2 did not affect the binding of HU210 and CP55940 binding as in the CB1 receptor (164). Modelling of the CB2 receptor with CP55940 revealed an alternate binding mode that meant mutation of K3.28 did not affect ligand binding energy to a significant extent. Simultaneously, S3.31 was identified as a possible key interacting residue for CP55940, and this was subsequently proven via a S112G mutagenesis study.

Song *et al* docked the aminoakylindole ligand WIN55212-2 into a model of CB2 in order to investigate its selectivity for CB2 over CB1 (165). It was found that besides aromatic stacking with F3.25, F3.36, and W5.43 there is an additional fourth aromatic interaction with F5.46 in CB2, with the corresponding residue in CB1 being a valine. Subsequent mutation of F5.46 to valine decreased WIN55212-2 binding by 14 fold with no effect on other ligand classes, while mutation of the corresponding valine in CB1 to phenylalanine increased WIN55212-2 binding by 12-fold, highlighting the importance of this residue in the CB2 selectivity of WIN55212-2.

McAllister *et al* applied Monte Carlo/Stochastic Dynamics to models of CB1 with Y5.39F and Y5.38I mutations to investigate the importance of aromaticity and hydrogen-bonding capability on these residues (166). The modelling studies showed that loss of aromaticity resulted in a rearrangement of key residues within the receptor. They then tested this hypothesis in the lab by studying Y5.39I mutants of CB1, which showed loss of ligand binding and signal transduction, supporting their modelling observations. The same group then created an active-state model of CB1 using the Conformational Memories technique which was aided by experimental data (167). Docking of the several ligands into both the inactive and active state models revealed several residues of interest, such as F3.25, F3.36, Y4.64, W5.43 and W6.48 which were then mutated in ligand-binding studies. A detailed functional analysis was carried out in a follow-up study, where modelling results suggested that F3.36 and W6.48 formed a toggle switch that is broken during receptor activation, supporting the results of previous studies (168).

Another study utilizing the Conformational Memories technique by Kapur *et al* following mutagenesis studies of S2.60A and S7.39A in CB1 predicted that S7.39 induces a helix bend in TM7 that provides space for the binding of CP55940 (169). Modelling studies with the mutant receptor predicted an alteration to this binding space that precluded CP55940 binding.

Gouldson *et al* mutated S4.53 and S4.57 in CB2 to alanine and found that this reduced its affinity for SR144528 (170). The docking of SR144528 into a model of CB2 led to the proposal of a binding pose of SR144528 that involved hydrogen bonds with both the serines studied. Similarly, Zhang *et al* mutated W5.43 in the CB2 receptor to tyrosine, phenylalanine, and alanine following modelling studies by Montero *et al* that highlighted W5.43 as a possible interaction site for SR144528 (171,172). The W5.43Y mutant retained CP55940 binding but had reduced affinity for WIN55212-2 and SR144528; the W5.43F and W5.43A mutations significantly affected the binding affinities of all three ligands. The authors then predicted the binding mode of CP55940, WIN55212-2, and SR144528 leading to the conclusion that both aromaticity and hydrogen bonding plays a role in ligand binding at W5.43. More recently, Sitkoff *et al* mutated F200 and S383 in CB1 and proposed a binding mode for a new inverse agonist chemotype, the tetrahydroquinolines, based on the mutagenesis results and structure-activity relationships observed (173).

1.4 Fenofibrate derivatives as cannabinoid receptor ligands

1.4.1 Fibrates: Therapeutic use as PPARα agonists

The fibrates are a class of small molecules that structurally resemble short chain fatty acids. The first fibrate to be used medicinally for hypercholesterolemia was clofibrate **19**, which was discovered in 1961 and followed by gemfibrozil **20** and fenofibrate **21** (see Figure 1-15) (174). Fenofibrate itself is a prodrug, and is converted via ester hydrolysis to its active form fenofibric acid **22**. The prominence of fibrates in hyperlipidaemia therapy fell following less than stellar performances in major clinical trials, safety concerns, and the emergence of HMG-CoA reductase inhibitors (more popularly known as statins) as the preferred drug of choice in such conditions (174). The use of fibrates, particularly gemfibrozil and fenofibrate, are currently supported for specific variants of metabolic disorders such as hypertriglyceridemia, mixed dyslipidemia, and isolated low levels of HDL (174).

Clofibrate **19**

Gemfibrozil **20**

Fenofibrate **21**

Low activity at PPAR
Active at CB1 (pK_i = 6.32)
Active at CB2 (pK_i = 6.91)

Fenofibric acid **22**

High activity at PPAR
Inactive at CB1
Inactive at CB2

GW409544 **23**
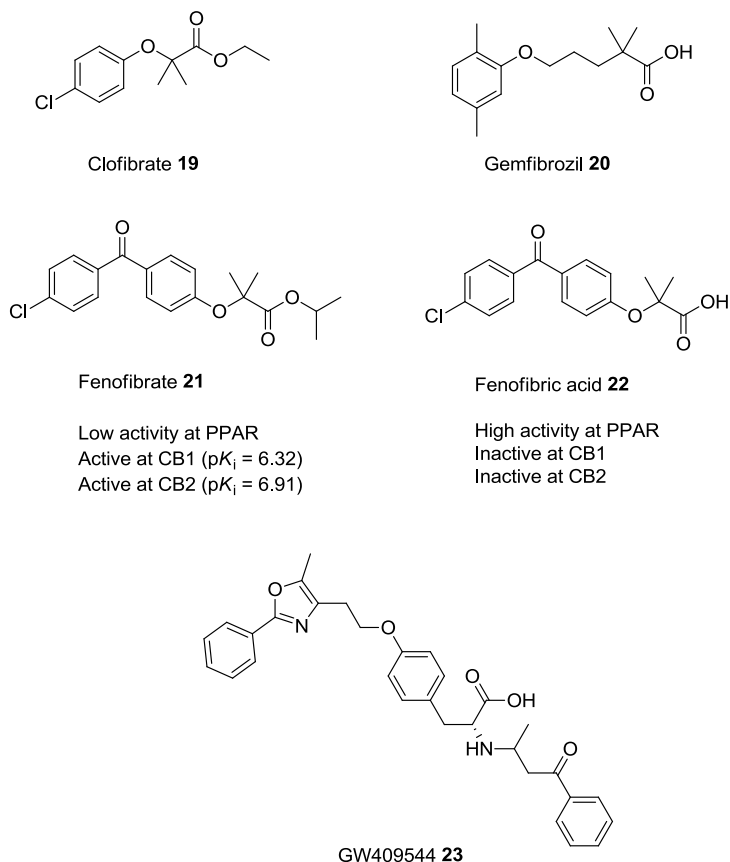
Figure 1-15 Structure of fibrates

The mechanism of action of fibrates is complex, but primarily involves the activation of a group of receptors known as the peroxisome proliferator-activated receptors (PPARs), particularly PPARα (175). The PPARs are nuclear receptors that modulate various physiological processes such as lipid metabolism, blood pressure, glucose control and insulin resistance. Activation of PPARα by the fibrates results in the expression of genes involved in multiple metabolic pathways, resulting in decreased triglyceride and very low density lipoprotein (VLDL) levels, as well as increased HDL levels (176). The structure of the ligand binding domain of PPARα (the receptor also contains a DNA binding domain and a ligand-dependent activating domain) in complex with a ligand GW409544 **23** and co-activator peptide was first solved via X-ray crystallography in 2001; its structure is shown below in Figure 1-16 (177).
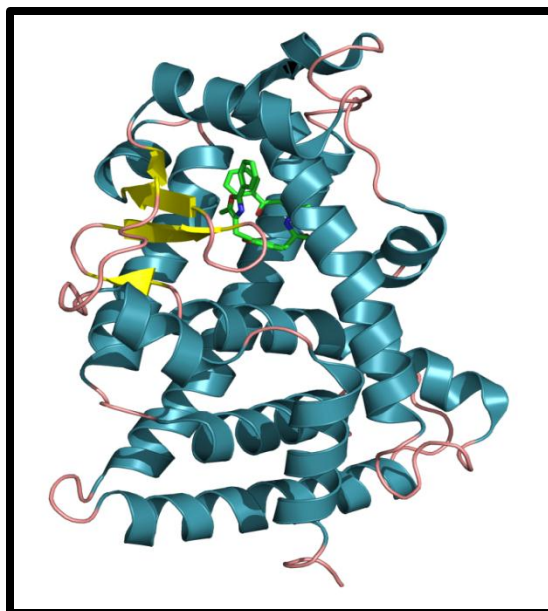
Figure 1-16 Crystal structure of PPARα with bound GW409544

1.4.2 Fenofibrate amide derivatives as cannabinoid receptor ligands

It has been recently shown that fenofibrate, but not its active metabolite fenofibric acid, possesses agonist activity at both of the cannabinoid receptors with a binding affinity (pK_i) of 6.32 at CB1 and 6.97 at CB2 (K_i 480nM and 108nM respectively) (178,179). While it followed that a dual ligand, possessing agonist activity at the PPARα receptor and antagonist activity at the CB1 receptor would have potential benefit in the treatment of obesity and associated hyperlipidemias, novel amide fenofibrate derivatives investigated were found to possess significant affinity for both cannabinoid receptors but lost PPARα activity (179). These derivatives along with their pharmacological properties at the cannabinoid receptors are shown in Table 1-2 and Table 1-3.
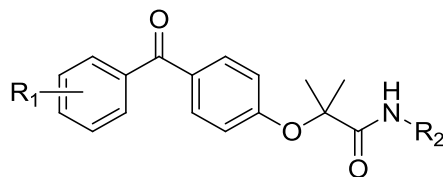
No	R$_1$	R$_2$	pK$_i$ at CB1[a]	% CB1 activation at 10 μM [b]	pK$_i$ at CB2[a]	% CB2 activation at 10 μM [b]
24a	4-Cl	(CH$_2$)$_2$OH	-	112 ± 7	< 5	93 ± 9
24b	4-Cl	(CH$_2$)$_4$OH	-	110 ± 29	6.42	144 ± 14
24c	4-Cl	(CH$_2$)$_6$OH	-	125 ± 8	6.20	113 ± 6
24d	4-Cl	*i*-Pr	-	105 ± 19	6.36	121 ± 3
24e	4-Cl	(CH$_2$)$_5$CH$_3$	-	87 ± 13	5.92	84 ± 2
24f	4-Cl	CH$_2$Ph	-	113 ± 11	6.66 ± 0.02	84 ± 23
24g	4-Cl	piperidin-1-yl	6.99 ± 0.11	137 ± 6	7.82 ± 0.10	152 ± 10
24h	4-Cl	morpholin-4-yl	6.82 ± 0.16	149 ± 7	7.80 ± 0.06	153 ± 2
24i	4-Cl	2-(pyrrolidin-1-yl)eth-1-yl	-	101 ± 20	-	89 ± 15
24j	4-Cl	2-(morpholin-4-yl)eth-1-yl	-	123 ± 15	-	87 ± 8
24k	4-Cl	*t*-Bu	-	108 ± 9	-	69 ± 10
24l	4-Cl	4-methyl-piperazin-1yl	-	94 ± 10	-	78 ± 10
24m	4-Cl	4-(2-hydroxyethyl)-phen-1-yl	-	101 ± 8	-	73 ± 10
24n	4-Cl	Ph	-	87 ± 8	6.84 ± 0.16	104 ± 3

Table 1-2 Pharmacological properties of an initial set of novel amide derivatives of fenofibrate at the cannabinoid receptors (179). *Data represents mean values ± SEM of three independent experiments. If no SEM is shown a single experiment was performed.* [a] *Displacement of [³H]CP55940 in membrane homogenates of CHO cells transfected with human CB1 or CB2 receptors over 10 concentration values; binding affinities (pK$_i$) were determined using experimental IC$_{50}$ values and the Cheng-Prusoff equation (21).* [b] *Measurement of enhancement of [35S]GTPγS binding in membrane homogenates of CHO cells transfected with human CB1 or CB2 receptors, expressed as % of basal binding at a single concentration of 10μM.*
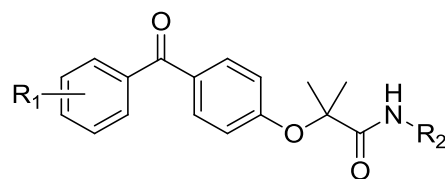
No	R_1	R_2	pK_i at CB1[a]	% CB1 activation at 10 μM [b]	pK_i at CB2[a]	% CB2 activation at 10 μM [b]
25a	4-Cl	CH$_2$(2-F-Ph)	-	83 ± 21	6.23 ± 0.11	75 ± 6
25b	4-Cl	CH$_2$(3-F-Ph)	-	87 ± 11	6.37 ± 0.08	69 ± 10
25c	4-Cl	CH$_2$(4-F-Ph)	-	100 ± 17	6.62 ± 0.06	80 ± 2
25d	4-Cl	CH$_2$(2-Me-Ph)	-	61 ± 18	5.94 ± 0.04	68 ± 9
25e	4-Cl	CH$_2$(3-Me-Ph)	-	85 ± 14	5.63 ± 0.11	39 ± 5
25f	4-Cl	CH$_2$(4-Me-Ph)	-	76 ± 15	5.88 ± 0.14	40 ± 2
26a	4-Cl	2-F-Ph	-	69 ± 16	5.94 ± 0.18	90 ± 4
26b	4-Cl	3-F-Ph	-	111 ± 11	5.48 ± 0.01	97 ± 10
26c	4-Cl	4-F-Ph	-	91 ± 2	5.87 ± 0.13	89 ± 6
26d	4-Cl	2-Me-Ph	-	100 ± 8	5.81 ± 0.03	89 ± 5
26e	4-Cl	3-Me-Ph	-	114 ± 8	6.12 ± 0.14	87 ± 4

Table 1-3 Pharmacological properties of a second set of novel amide derivatives of fenofibrate at the cannabinoid receptors (179). *Data represents mean values ± SEM of three independent experiments. If no SEM is shown a single experiment was performed.* [a] *Displacement of [^{3}H]CP55940 in membrane homogenates of CHO cells transfected with human CB1 or CB2 receptors over 10 concentration values; binding affinities (pK_i) were determined using experimental IC$_{50}$ values and the Cheng-Prusoff equation.* [b] *Measurement of enhancement of [35S]GTPγS binding in membrane homogenates of CHO cells transfected with human CB1 or CB2 receptors, expressed as % of basal binding at a single concentration of 10μM.*
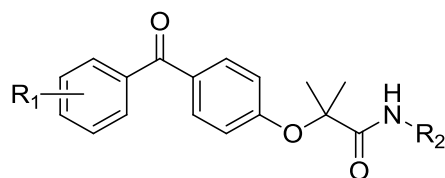
No	R$_1$	R$_2$	pK_i at CB1	% CB1 activation at 10 μM	pK_i at CB2	% CB2 activation at 10 μM
27a	2-Me	morpholin-4-yl	-	99 ± 10	7.25 ± 0.12	148 ± 24
27b	3-Me	morpholin-4-yl	-	99 ± 7	-	104 ± 5
27c	4-Me	morpholin-4-yl	-	103 ± 18	6.51 ± 0.02	160 ± 9
27d	3-CN	morpholin-4-yl	-	107 ± 11	-	98 ± 1
27e	3-Cl	morpholin-4-yl	-	101 ± 6	-	82 ± 4
27f	2-F	morpholin-4-yl	7.04 ± 0.07	130 ± 19	6.84 ± 0.07	119 ± 19
27g	3-F	morpholin-4-yl	-	89 ± 9	-	116 ± 5
27h	4-F	morpholin-4-yl	-	89 ± 7	6.64 ± 0.15	135 ± 7
27i	3-NO$_2$	morpholin-4-yl	-	92 ± 14	-	106 ± 14
27j	H	morpholin-4-yl	-	92 ± 18	6.52 ± 0.01	137 ± 8
28a	2-Me	piperidin-1-yl	-	105 ± 9	-	102 ± 23
28b	3-Me	piperidin-1-yl	-	102 ± 14	-	77 ± 14
28c	4-Me	piperidin-1-yl	7.59 ± 0.15	174 ± 20	7.54 ± 0.14	155 ± 4
28d	3-CN	piperidin-1-yl	-	112 ± 12	-	108 ± 1
28e	4-CN	piperidin-1-yl	-	104 ± 4	-	114 ± 19
28f	3-Cl	piperidin-1-yl	-	97 ± 8	-	82 ± 18
28g	2-F	piperidin-1-yl	-	119 ± 13	-	134 ± 4
28h	3-F	piperidin-1-yl	-	87 ± 15	-	110 ± 9
28i	4-F	piperidin-1-yl	7.34 ± 0.15	140 ± 22	7.85 ± 0.08	129 ± 9
28j	H	piperidin-1-yl	-	127 ± 6	-	124 ± 3

Table 1-3 (cont.) Pharmacological properties of a second set of novel amide derivatives of fenofibrate at the cannabinoid receptors.

The initial set of compounds **24a-n**, intended as a broad structural exploration, revealed some preliminary structure-activity relationships. Compounds with cyclic carboxamide N-substituents (**24f-h,n**) showed higher binding affinities to CB2 than their alkyl and hydroxyalkyl counterparts (**24a-e**), alluding to possible steric constraints within the binding site. Similar conclusions could not be made for CB1 due to the limited data available. These compounds also displayed varied efficacy, evidenced by the fact that the four compounds with the highest binding affinities (**24f-h,n**) consisted of two agonists, one inverse agonist and one neutral antagonist for both receptors. These four compounds were subsequently developed further to explore substitution effects at the R_1 and R_2 regions of the fenofibrate scaffold.

Introduction of a fluoro or methyl substituent to the benzyl functionality **25a-f** did not improve CB2 affinity, although the methyl analogues showed lower binding, once again suggesting some possible steric constraints. However, this effect was not replicated in the phenyl analogues **26a-e**, as substitution of the phenyl decreased CB2 affinity in an analogous manner regardless. Substitution of the benzophenone moiety in the morpholinyl and piperidinyl analogues **27a-28j** similarly did not improve CB2 affinity significantly compared to **24g** and **24h**, although most of the compounds assayed showed comparable nanomolar affinity. Taking into account the varied affinities of **24a-n**, the relevance of the carboxamide substituent towards CB2 receptor affinity is clearly evident. Functionally, **25a-26e** all displayed inverse agonism at CB2 and either inverse agonism or neutral antagonism at CB1, indicating that the efficacy of these analogues may be dependent more on the predominantly aromatic nature of the carboxamide substituent rather than any specific substitution effects. Modification of the benzophenone moiety appears to be slightly more significant in this respect, as demonstrated by the fact that the morpholinyl and piperidinyl analogues displayed more varied efficacy at the CB2 receptor. All compounds substituted at position 2 and 4 of the R_1 aryl exhibited some degree of agonist activity, while the 3-substituted compounds, with the exception of the 3-fluoro compounds **27g** and **28h**, exhibited neutral

antagonist or inverse agonist character. In contrast, substitution effects had less of an influence on CB1 activity, with all morpholinyl and piperidinyl derivatives displaying neutral antagonist/inverse agonist activity, with the exception of the fluoro substituted **27f**, **28g**, **28i**, the 4-methyl substituted **28c**, and the unsubstituted **28j**, which showed some degree of agonist activity.

While the findings of this study serves as a useful starting point in the development of the fenofibrate scaffold as a new class of cannabinoid receptor ligands, the structure-activity relationships derived were not particularly distinct. A molecular modelling study incorporating the pharmacological data obtained would allow for the rationalization of these findings and a more focused approach in developing further fenofibrate amide derivatives as cannabinoid receptor ligands. This effort to employ a structure-based approach within this research area represents the main focus of this doctoral dissertation.

2   AIMS AND OBJECTIVES

This project aims to construct validated homology models of the human cannabinoid receptors CB1 and CB2, which will be refined using molecular dynamics simulations in a fully-hydrated lipid bilayer, for use in rational drug design. Specifically, these models are constructed with a view to study the binding of novel cannabinoid receptor ligands that are based on the PPARα agonist fenofibrate. The information obtained from analysing their binding will be used to rationalize previous pharmacological data and to design further novel derivatives using a structure-based approach. These novel derivatives will subsequently be synthesized and their pharmacological properties determined in order to evaluate our modelling predictions for improved future drug design.

3 MOLECULAR MODELLING OF THE CANNABINOID RECEPTORS AND STRUCTURE VALIDATION

3.1 Construction and assessment of homology models

3.1.1 Template selection and sequence alignment

The amino acid sequences of both cannabinoid receptors and all GPCRs whose crystal structure had been solved to date were obtained from the UniProt Knowledgebase (UniProt Accession Numbers: P21554 (human CB1), P34972 (human CB2), P02699 (bovine rhodopsin), P31356 (squid rhodopsin), P07700 (avian adrenoceptor β2), P07550 (human adrenoceptor β2), P29274 (human adenosine A2A), P35462 (human dopamine D_3), P61073 (human chemokine $CXCR_4$), and P35367 (human histamine H_1)) (180). In order to determine which GPCR would be the most suitable template, the amino acid sequence of each GPCR was individually aligned against the cannabinoid receptors using the EMBOSS Water tool (a modified Smith-Waterman algorithm) available through the European Bioinformatics Institute server (181). The results of these pairwise alignments are presented in Table 3-1.

GPCR with known structure	% Identity with CB1	% Identity with CB2
Bovine rhodopsin	25.4	21.1
Squid rhodopsin	23.5	23.2
Avian adrenoceptor β1	25.9	26.5
Human adrenoceptor β2	25.7	25.0
Human adenosine A2A	**28.0**	**27.1**
Human dopamine D3	21.6	20.5
Human chemokine CXCR4	20.8	23.4
Human histamine H1	18.9	17.6

Table 3-1 Pairwise sequence alignment of the CB1 and CB2 cannabinoid receptors against GPCRs with known crystal structures. *The highest sequence identities are highlighted in bold.*

Overall, sequence identity between the cannabinoid receptors and the other GPCRs was found to be poor with all pairwise sequence identities below 30%, a critical level in protein-sequence analysis where conventional sequence alignment methods are more likely to produce errors (135). However, in the case of GPCRs this low sequence identity is compensated by their well-defined seven transmembrane structure; sequence similarity in the transmembrane regions are generally high, with insertions and deletions being much more likely to occur in the loop regions. The adenosine A2A receptor showed the highest sequence identity with both cannabinoid receptors (28.0% identity with CB1 and 27.1% identity with CB2 respectively). This is in agreement with the phylogenetic analysis results presented by Fredriksson *et al*, where the cannabinoid and adenosine receptors are classified in the same subgroup (1). As such, the adenosine A2A receptor was selected as the template for our homology modelling and for further refinement of the sequence alignment.

A multiple sequence alignment of the human CB1, CB2 and A2A receptors was then done using CLUSTALW2 (182), with the Gonnet protein weight matrix and a gap open penalty set to 25. The resulting alignment was then manually edited using JALVIEW (183), in order to remove gaps and maximize sequence similarity in the TM regions. This final sequence alignment, with the N and C termini (residues 1-112 and 418-473 of CB1, residues 1-29 and 320-360 of CB2) omitted, is presented in Figure 3-1.

The sequence alignment produced showed the most conserved residues in each helix, as defined by Ballesteros-Weinstein (N1.50, D2.50, R3.50, W4.50, P5.50, P6.50, P7.50), to be present and aligned (47). The exception to this was P5.50, which is not conserved in either cannabinoid receptor. The second most conserved residue within TM5 is Y5.58, and consequently using the 'structural alignment' detailed in Bramblett *et al* (150), Y5.58 in the A2A receptor was aligned with Y294 in CB1 and Y209 in CB2. Other highly conserved motifs, such as the DRY motif in TM3, the CWXP motif in TM6, and the NPXXY motif in TM7 were also found to be present and aligned. Cysteine residues involved in disulfide bridge formation in the A2A receptor were not found to be

conserved. Previous mutagenesis experiments, however, have shown that a disulfide bridge is likely to exist between C257-C264 for CB1 and C174-179 for CB2 respectively (170,184).

```
CB1    NFMDIECFMVLNPSQQLAIAVLSLTLGTFTVLENLLVLCVILHSRSLRCR
CB2    ----MKDYMILSGPQKTAVAVLCTLLGLLSALENVAVLYLILSSHQLRRK
A2A    ----------MPIMGSSVYITVELAIAVLAILGNVLVCWAVWLNSNLQN-
                  :     . .  .:    :. :: * *: *    :  . .*:

CB1    PSYHFIGSLAVADLLGSVIFVYSFIDFHVFHRKDSRNVFLFKLGGVTASF
CB2    PSYLFIGSLAGADFLASVVFACSFVNFHVFHGVDSKAVFLLKIGSVTMTF
A2A    VTNYFVVSLAAADIAVGVLAIPFAITISTGFCAAC-HGCLFIACFVLVLT
         :   *: *** **:   .*:      : :  .    .     *:     *

CB1    TASVGSLFLTAIDRYISIHRPLAYKRIVTRPKAVVAFCLMWTIAIVIAVL
CB2    TASVGSLLLTAIDRYLCLRYPPSYKALLTRGRALVTLGIMWVLSALVSYL
A2A    QSSIFSLLAIAIDRYIAIRIPLRYNGLVTGTRAKGIIAICWVLSFAIGLT
          :*: **:   *****:.:: *   *: ::*   :*    : : *.::  :.

CB1    PLLGWNCEKLQSVCSDIFP---------------HIDETYLMFWIGVTSV
CB2    PLMGWTCCPRP--CSELFP--------------LIPNDYLLSWLLFIAF
A2A    PMLGWNNCGQPKEGKNHSQGCGEGQVACLFEDVVPMNYMVYFNFFACVLV
       *::**.             .:              :     : ::    .

CB1    LLLFIVYAYMYILWKAHSHAVRMIQRGTQKSIIIHTSEDGKVQVTRPDQA
CB2    LFSGIIYTYGHVLWKAHQHVASLSGHQDR-------------QVPGMARM
A2A    PLLLMLGVYLRIFLAARRQLKQMESQPLP-------------GERARSTL
        :   :: .*   ::  *:  :    :  :

CB1    RMDIRLAKTLVLILVVLIICWGPLLAIMVYDVFG-KMNKLIKTVFAFCSM
CB2    RLDVRLAKTLGLVLAVLLICWFPVLALMAHSLAT-TLSDQVKKAFAFCSM
A2A    QKEVHAAKSLAIIVGLFALCWLPLHIINCFTFFCPDCSHAPLWLMYLAIV
        : ::: **:* ::: :: :** *:   :  .       ..      : :. :

CB1    LCLLNSTVNPIIYALRSKDLRHAFRSMFPSCEG-----------TAQPLD
CB2    LCLINSMVNPVIYALRSGEIRSSAHHCLAHWKK-----------CVRGLG
A2A    LSHTNSVVNPFIYAYRIREFRQTFRKIIRSHVLRQQEPFKAAGTSARVLA
       *.   ** ***.*** *   ::*  : :   :               .: *
```

Figure 3-1 Sequence alignment of human cannabinoid CB1, cannabinoid CB2 and adenosine A_{2A} receptor, with N and C termini excluded for clarity. * *indicates residue identity, : high residue similarity, and . low residue similarity. The TM regions, as defined in reference* (28)*, are highlighted yellow. The most conserved residues of each TM helix are highlighted turquoise. The 2nd most conserved residue of TM5, Y5.58, is highlighted red. Disulfide bridges were constructed between the cysteine residues highlighted in green.*

3.1.2   Initial model construction and assessment

The coordinates of the crystal structure of the adenosine A2A receptor bound to an inverse agonist was obtained from the PDB (PDB code: 3EML) (28). Using these coordinates as a template and the sequence alignment described in section 3.1.1, MODELLER (185), was used to generate an initial model of the human CB1 and CB2 receptors. The N-termini (residues 1-112 of CB1 and 1-29 of CB2) and C-termini (residues 418-473 of CB1 and 320-360 of CB2) of both receptors were truncated. A disulfide bridge was constructed between C257-C264 and C174-179 for CB1 and CB2 respectively. 50 models were generated for both CB1 and CB2. Models were evaluated using high-resolution DOPE scores, which are based on a statistical potential, generated by MODELLER, and the models with the best DOPE score was selected for further refinement.

As the template structure 3EML did not possess a 3rd intracellular loop due to its replacement with T4L, this loop (30 and 17 residues long in CB1 and CB2 respectively) was subject to further refinement using the loop modelling class within MODELLER. 25 loop conformations were generated for each model. These conformations were then visually inspected to ensure a reasonable loop conformation (defined as the absence of breaks or knots within the loop, and the loop not intruding into the transmembrane region). The models possessing reasonable loop conformations with the best DOPE scores were then selected as our initial structures for the next stage of molecular dynamics.

The selected structures were then subject to energy minimization to relieve any steric clashes that could have arisen during model construction. The stereochemical quality of each structure was then assessed by generating Ramachandran plots using PROCHECK (128). The energy-minimized structures and their respective Ramachandran plots are shown in Figure 3-2.
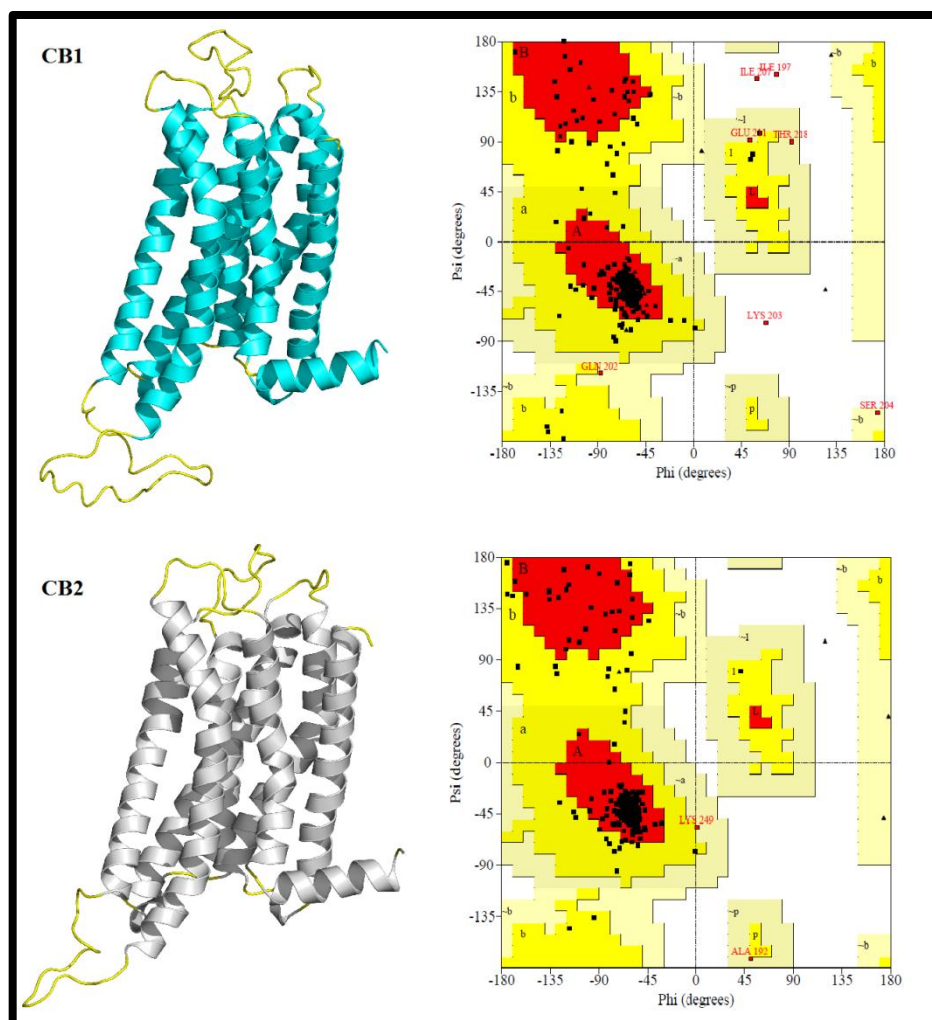
Figure 3-2 Homology models of the cannabinoid receptors and their corresponding Ramachandran plots. *The contours on each plot were derived from the phi and psi angles of 118 protein crystal structures. The red, yellow, beige, and white regions represent the most favoured, additionally allowed, generously allowed and disallowed regions respectively. Glycine and proline residues are represented as triangles, whereas all other residues are represented as squares.*

In both cases, energy minimization converged to acceptable potential energy values before all iterations were completed. The Ramachandran plot of CB1 showed 84.4% of residues to be in the most favoured regions, with 13.1% in the additional allowed regions, 1.4% in the generously allowed regions, and 1.1% in disallowed regions. The Ramachandran plot of CB2 showed 89.3% of residues to be in the most favoured regions, with 10.0% in additionally allowed regions, 0.7% in the generously allowed regions, and 0.0% in the disallowed regions.

Our results show 98.9% of residues in CB1 and 100% of the residues in CB2 to be in conformations observed in typical crystal structures, although ideally at least 90% of these residues should be in the most favoured regions (186). Further visual analysis of residues in the disallowed regions revealed that these residues were all located in the 3rd intracellular loop of which our adenosine A2A crystal structure did not provide a template, and is not known to participate in ligand binding. As such, these structures were deemed to be of sufficient quality to be further refined via molecular dynamics simulations.

3.2   Molecular dynamics simulations of the cannabinoid receptors

3.2.1   Selection of force field parameters

Taking into consideration the computational resources available and the length of simulations to be run, the GROMOS 53a6 united-atom force field (140) was selected as the primary force field for all molecular dynamics simulations. The united-atom approach (non-polar hydrogens are not explicitly represented) substantially reduces computational cost, and is particularly advantageous in the simulation of lipid bilayers. The GROMOS 53a6 force field has been parameterized to reproduce the free enthalpies of solvation of amino acid analogues in cyclohexane and water, and the thermodynamic properties in the liquid phase of a range of small polar molecules (140). This force field has also been subsequently validated for simulations of protein, peptides and DNA in water (187). However, it has been shown that this force field parameter set does not adequately reproduce the correct area per lipid, which is the primary property used in the validation of computational models of lipid bilayers (188). Over the years additional parameters for the treatment of lipids using the GROMOS force fields have been proposed, such as those presented by Berger *et al* (a combination of parameters from the GROMOS and OPLS force field), Kukol *et al*, and Poger *et al* (188–190). The parameters presented by Poger *et al* have been shown to not only reproduce the correct area per lipid for various lipid simulations, but have also validated against other experimental data, such as volume per lipid, bilayer thickness, isothermal area compression modulus, deuterium order parameters, acyl chain conformations, and headgroup orientation and hydration (191). These parameters were therefore selected to supplement the parameters within the GROMOS 53a6 force field (see section 8.1 for details on all parameters used in molecular dynamics simulations).

3.2.2 Lipid bilayer construction and equilibration

The coordinate file of a hydrated, equilibrated 128 lipid POPC (Figure 3-3) bilayer along with additional lipid parameters for the GROMOS 53a6 force field were obtained from Poger *et al* (188).
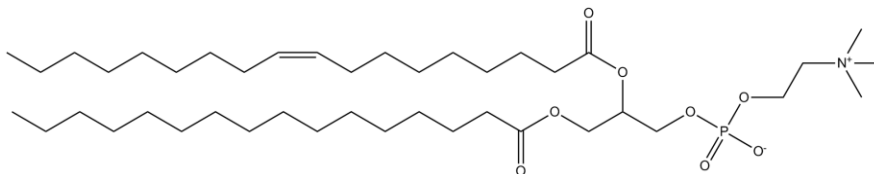
**Figure 3-3** Structure of 1-palmitoyl-2-oleoyl-sn-glycero-3-phosphocholine (POPC) **29**

This coordinate file was then resized using the tools available within GROMACS to produce a fully hydrated, 316 lipid bilayer of dimensions 124 x 124 x 114 Å. This system then was subject to energy minimization. The minimized structure was then subjected to 100ps of molecular dynamics using the NVT (constant number of atoms, volume, and temperature) ensemble, followed by 25ns using the NPT (constant number of atoms, pressure and temperature) ensemble. The results of this simulation are presented in Figure 3-4.
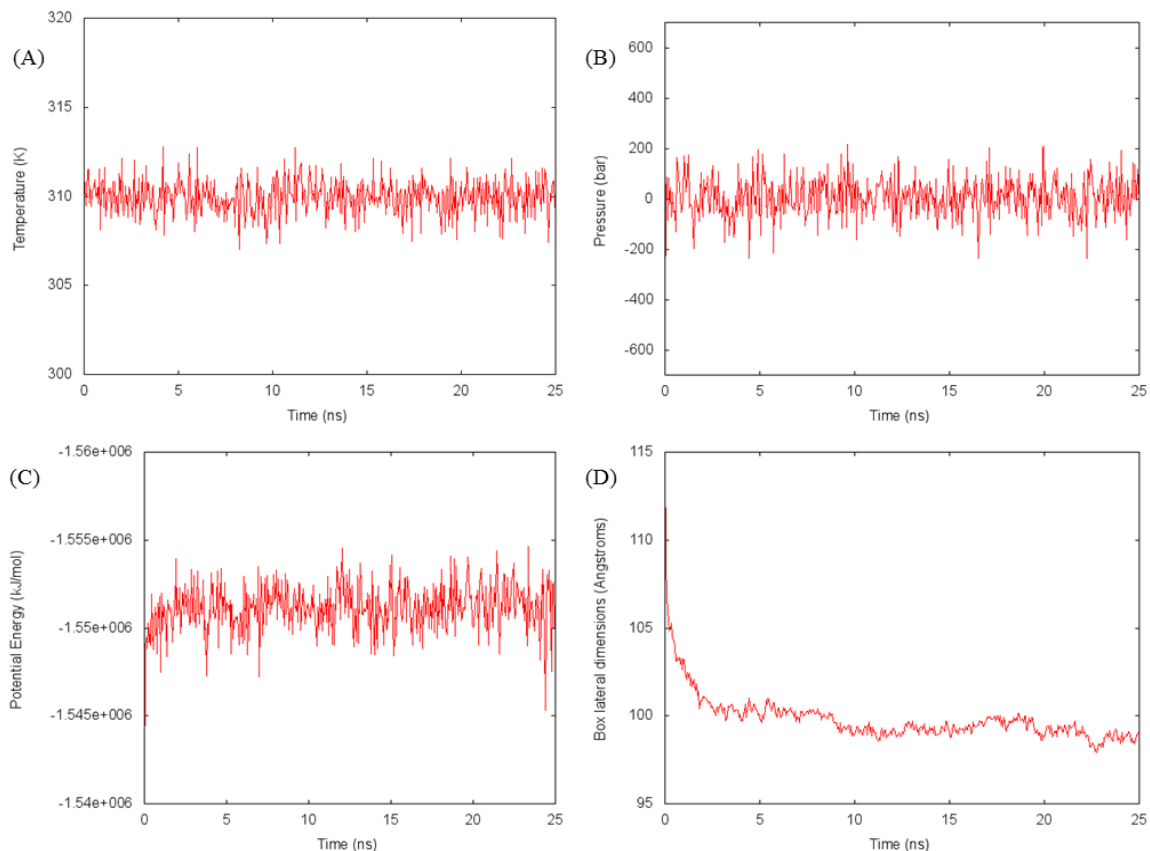
Figure 3-4 Fluctuations in: (A) Temperature (B) Pressure (C) Potential Energy (D) Box lateral dimensions of a POPC bilayer during 25ns of NPT molecular dynamics simulation.

Energy minimization converged to acceptable potential energy levels before all iterations of energy minimization were completed. The temperature, pressure, and potential energy of the lipid bilayer showed almost immediate equilibration and remained stable throughout the simulation. Lateral dimensions of the bilayer decreased for the first 10ns of dynamics and remained stable thereafter. Final dimensions of the lipid bilayer were 98.9 x 98.9 x 128 Å. This translated to an area per lipid (calculated as the lateral area of the box divided by the number of lipids in a single leaflet of the bilayer) of approximately 62.0 Å^2. This value is comparable to that obtained by Poger *et al* of 63.8 Å^2, and is also well within the experimental data range of 54.0 – 68.3 Å^2 (191–195). Visual inspection of final coordinates showed the lipid bilayer to be well-structured, with the absence of

any water molecules within the membrane, as shown in Figure 3-5. As our results indicated that the lipid bilayer constructed was equilibrated, these final coordinates were used for the subsequent embedding of our homology models.
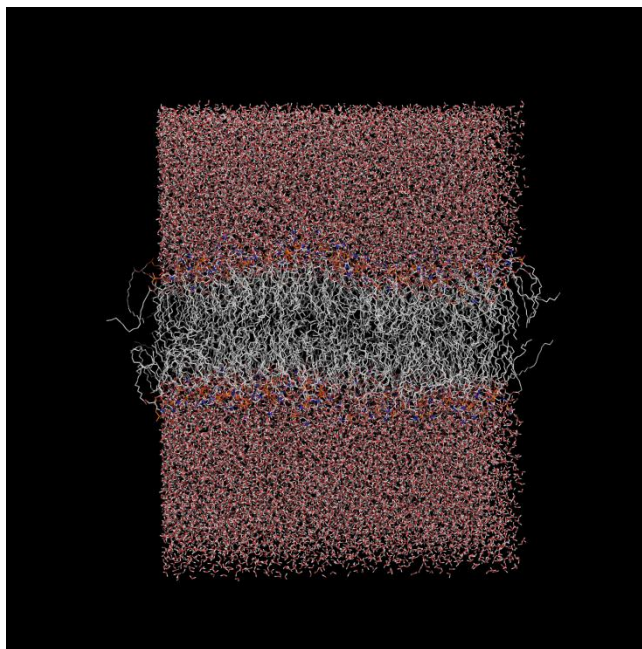

Figure 3-5 The hydrated POPC lipid bilayer system

3.4.1   Embedding of homology models into the lipid bilayer

Models of each cannabinoid receptor were manually placed in the POPC bilayer using the Visual Molecular Dynamics (VMD) program (196). Placement was guided by the alpha-helicity of the transmembrane regions and arginine/lysine patches at the membrane interface that are hypothesized to anchor the helices via interaction with the phospholipid head groups (150). The receptor was then embedded within the POPC bilayer using the *g_membed* tool within GROMACS (197). Embedding was conducted over 1000 MD steps, using a scaling factor of 0.5. Counter-ions where then added to the system before it was subject to energy minimization.

Embedding of the CB1 and CB2 receptors resulted in the removal of 36 and 30 lipid molecules respectively. Energy minimization converged to acceptable potential energy levels before all iterations were completed. The resulting structures are shown in Figure 3-6.
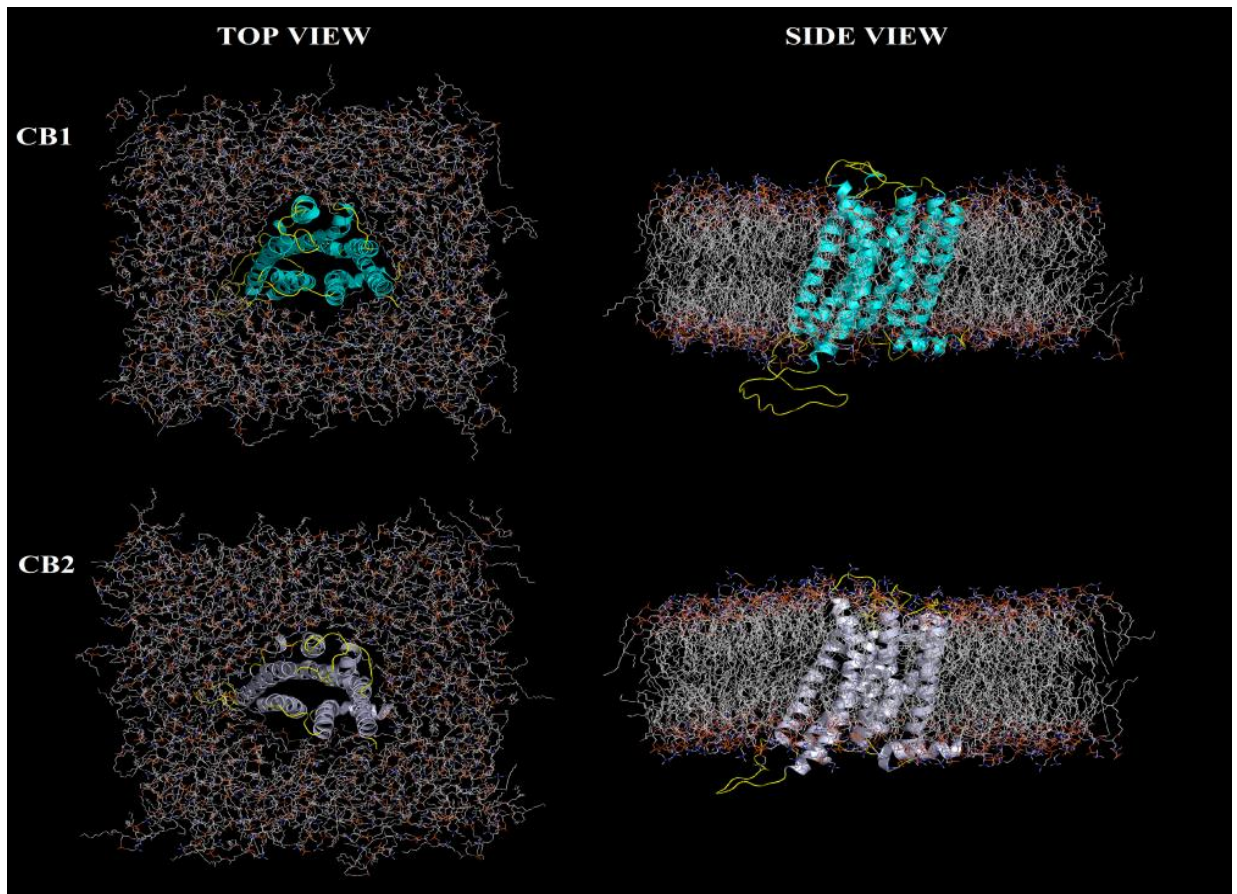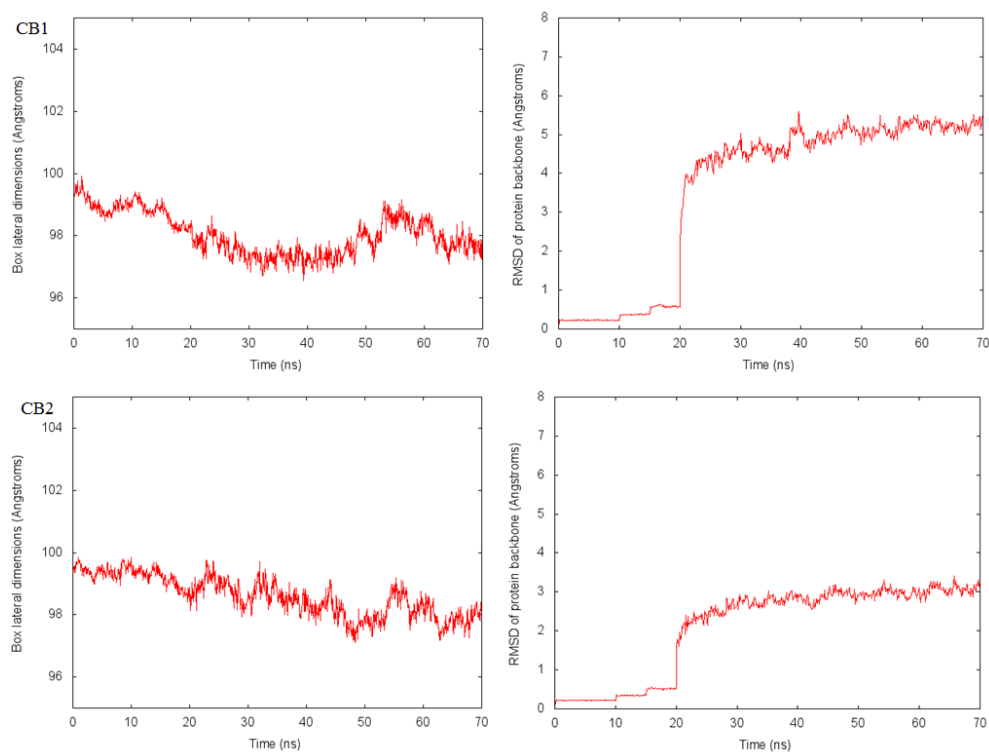

Figure 3-6 The cannabinoid receptors embedded within a POPC bilayer.

3.2.4 System equilibration

In order to equilibrate both proteins within the POPC bilayer, each system was subject to 100ps of molecular dynamics using the NVT ensemble, followed by 70ns using the NPT ensemble. Position restraints with a force constant of 1000 kJ/mol/nm^2 were initially applied on the protein and released in stages over the first 20ns of simulation (see Figure 3-7). The results of these simulations are presented in Figure 3-8.
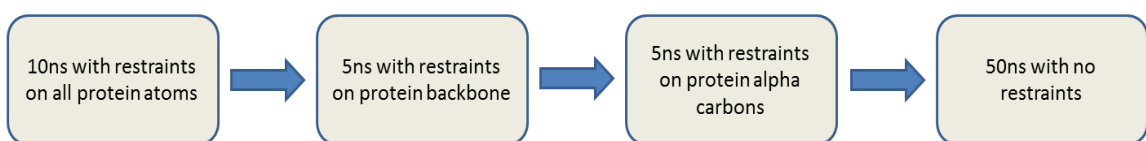
**Figure 3-7** Schematic representation of molecular dynamics for system equilibration

Figure 3-8 Equilibration of the cannabinoid receptors in a POPC bilayer

Temperature and pressure of both simulations showed almost immediate stabilization and remained as such throughout the simulation, whereas potential energy decreased with release of the position restraints and remained stable after 20ns (see Appendix 1). Box lateral dimensions stabilized after 30ns for CB1 and 50ns for CB2, with slight fluctuations within approximately 2Å. The root mean square deviation (RMSD) of the protein backbone for both receptors increased significantly at 20ns following release of position restraints and stabilized after 50ns of simulation, with an RMSD deviation from the initial structure of approximately 5Å for CB1 and 3Å for CB2. Such values indicate significant deviation from the initial structure but are typical of molecular dynamics simulations of homology models, as the overall structure of the initial model would be more similar to the structure of the template used. Movement of the loop regions, rather than the transmembrane helices, likely contributed significantly more to the RMSD deviations observed.

The lateral dimensions of a lipid bilayer system present an indirect measurement of the area per lipid. While our results thus indicate the area per lipid to be stable, the presence of the receptor disallows calculation of area per lipid directly from the lateral dimensions of the system. Area per lipid was thus derived using GridMAT-MD (198), with the final area per lipid, taking into account protein atoms, calculated to be 58.6Å for the CB1 system and 59.0Å for the CB2 system. While these values are much lower than those obtained for the pure lipid system, it should be noted that the effect of a membrane protein on area per lipid is currently still unknown, and they remain within the range of experimental data of $54.0 - 68.3$ Å^2 (192–195). Protein backbone RMSD, which is a commonly used parameter to infer protein stabilization in molecular dynamics, showed both receptors to be stable after 50ns of simulation. Interestingly, the average RMSD deviation for CB1 was significantly higher compared to CB2, indicating a starting structure that was further from its stable state. These results thus indicated both protein and lipid bilayer to be equilibrated.

3.2.5   Production simulations

In order to generate the conformational ensemble required to produce a validated model, the equilibrated systems were each given fresh velocities and subjected to further molecular dynamics until a stable protein backbone RMSD was achieved. The lowest energy conformations following protein stabilization where then extracted from this ensemble to undergo structure validation. The results are presented in Figure 3-9.
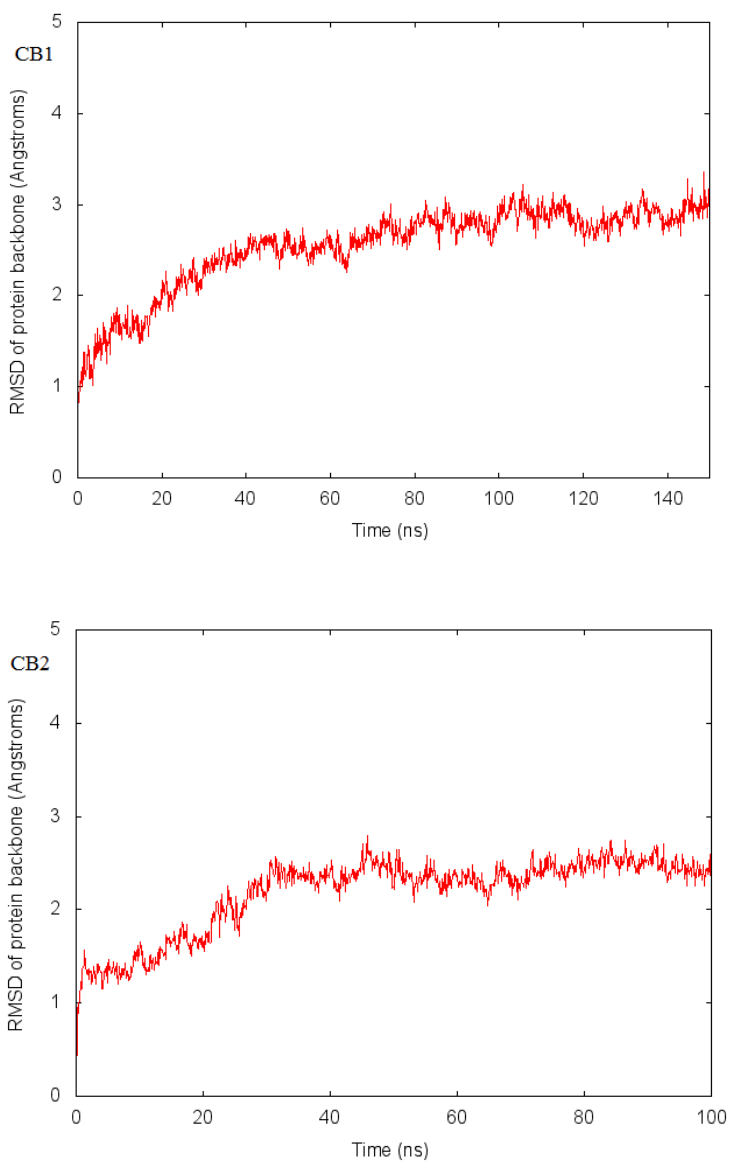

Figure 3-9 Production run of the cannabinoid receptors

For CB1, total production simulation time was 150ns. RMSD of protein backbone showed protein stabilization after approximately 80ns of simulation. For CB2, total production simulation time was shorter at 100ns as the receptor appeared to stabilize after approximately 40ns of simulation. The stabilization of protein backbone RMSD following only minor deviation from the initial structure possibly indicate that the dynamics were sampling local minima in their respective energy landscapes. The lowest energy conformations for CB1 were extracted from the time steps of 80.6ns, 109.8ns, 135.9ns, 145.5ns, while the lowest energy conformations for CB2 were extracted from the time steps of 81.2ns, 98.6ns, 58.2ns, and 96.0ns.

3.2.6   Molecular dynamics of the CB1 cannabinoid receptor with bound antagonist

Preliminary analysis of the CB1 receptor however, revealed that the binding site closes during molecular dynamics, thus precluding ligand docking and model validation. The molecular surface of the CB1 receptor binding site is shown in comparison to the CB2 receptor in Figure 3-10. Several strategies were subsequently employed to facilitate docking to our CB1 models, such as docking with flexible protein side chains, scaling of van der Waals radii, and active site pressurization (199). None of these methods proved to be particularly successful at keeping the binding site open and facilitating the docking of ligands. As such, both the equilibration and production simulations for the CB1 receptor were rerun, but with the CB1-selective antagonist SR141716 (rimonabant) bound to the keep the active site open.
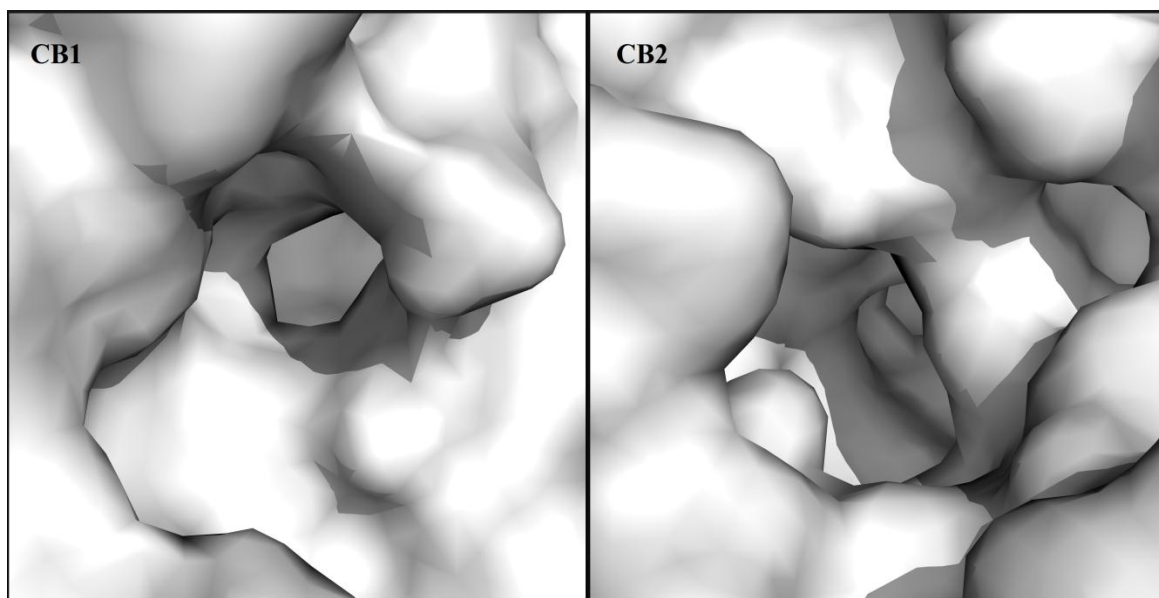
Figure 3-10 Molecular surface of the CB1 and CB2 receptor binding site. *The closed nature of the CB1 receptor binding site precluded ligand docking.*

Initial placement of the ligand was done using docking analysis and guided by mutagenesis data (167,184). The ligand was docked into the pre-equilibration model of the CB1 receptor using AutoDock4 (see section 8.1 for docking procedure and parameters used), and the lowest energy conformation that showed the best agreement with mutagenesis data was selected. The chosen conformation is shown in Figure 3-11, where SR141716 shows interaction with F3.36 and W6.48, with C7.42 in close proximity. Residue W5.43 did not appear to be within interacting distance in this model.
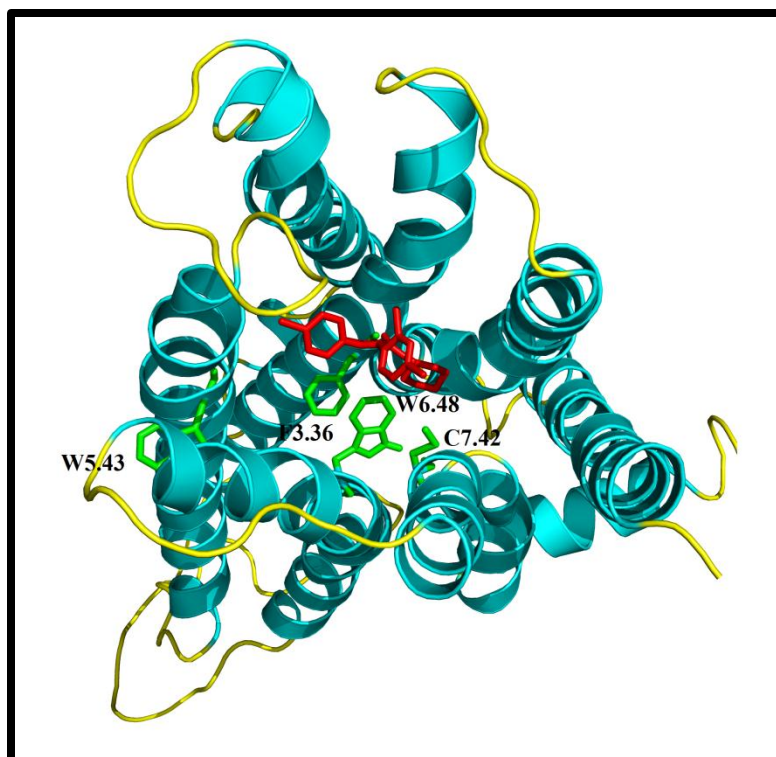
Figure 3-11 Initial placement of SR141716 binding to the CB1 binding pocket. *The ligand is shown in red while residues known to affect SR141716 through mutagenesis studies are shown in green.*

Partial charges used in ligand topology were assigned by combining the partial charges of individual functional groups available within the GROMOS 53a6 force field. For functional groups that were not parameterized in GROMOS 53a6, partial charges were obtained using the Automated Topology Force Field Builder (ATB) repository, which combines quantum-mechanical calculations with a knowledge-based approach to ensure compatibility with a specific GROMOS force field parameter set as far as possible (see Appendix II for full description of partial charges) (200).

Simulation of the receptor with bound SR141716 successfully kept the binding pocket open throughout all molecular dynamics runs. During equilibration, temperature and pressure stabilized almost immediately, while the lateral dimensions of the lipid bilayer and protein backbone RMSD stabilized after approximately 50ns of simulation (see Appendix I).

The results for the production run of the CB1 receptor with SR141716 bound are shown in Figure 3-12. Total simulation time was 350ns, and RMSD of the protein backbone in the transmembrane regions showed protein stabilization after approximately 220ns of simulation. The lowest energy conformations were extracted from the time steps of 240.7ns, 246.2ns, 262.9ns, 271.5ns, and 344.2ns. Analysis of the protein secondary structure showed slight unwinding of the alpha helices which was not seen in the CB2 simulations and have been previously associated with the GROMOS 53a6 force field (201).
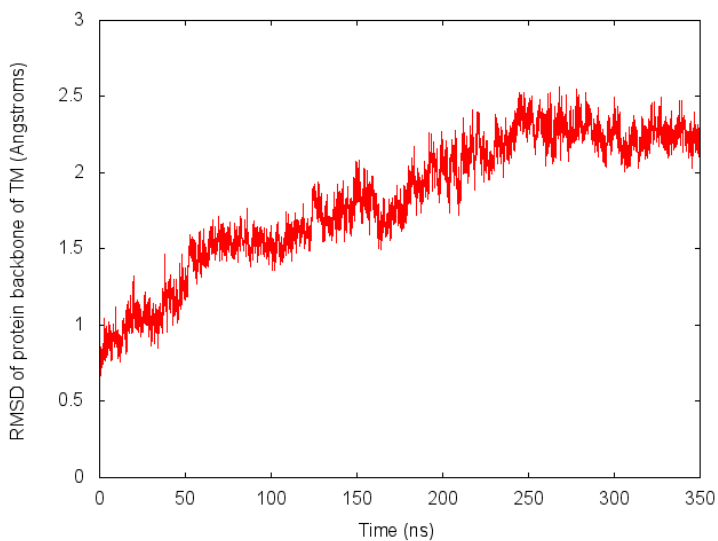

Figure 3-12 Production run of cannabinoid CB1 receptor with bound SR141716

3.3 Model validation

All structures extracted from the conformational ensemble generated via molecular dynamics simulations, in addition to the pre-equilibration structures, were then subjected to docking analysis in order to assess the ability of each model to reproduce experimental data. Ideally, for the purpose of binding mode prediction, one would validate a homology model via the reproduction of the experimentally determined binding mode of another ligand. In the absence of any crystal structure of either receptor this was not possible, and as such we have validated our models using docking evaluations and enrichment studies that demonstrated the ability of our model to predict the binding affinities of known ligands and distinguish between known ligands and decoys. Each model was assessed for its ability to correctly rank ligands according to their relative potency, as measured via the Spearman's rank correlation coefficient (ρ), and their ability to predict ligand binding affinities, as measured via the coefficient of determination (R^2). The models were then assessed in their ability to distinguish between known binders and a set of drug-like decoys in a virtual screening exercise, which was evaluated by plotting their corresponding Receiver Operating Characteristic (ROC) curves and area under the curve (AUC). Additionally, the predicted binding poses of several well characterized ligands were analysed in order to assess their agreement with mutagenesis data.

3.3.1 Binding affinity prediction of known ligands

A series of ligands, comprising of both agonists and antagonists capable of binding to each cannabinoid receptor, with experimental K_i values ranging over approximately 5 logarithmic values, were collected from literature (see Appendix III for full list of ligands and experimental pK_i values) (64,69,80,202–239). These ligands were individually docked to each receptor model extracted from the molecular dynamics simulations (see section 8.1 for full docking procedure and parameters used). The results from the best-performing model of the CB1 receptor (time step of 240.7ns) and CB2 receptor (time step of 96.0ns) are shown in Figure 3-13.
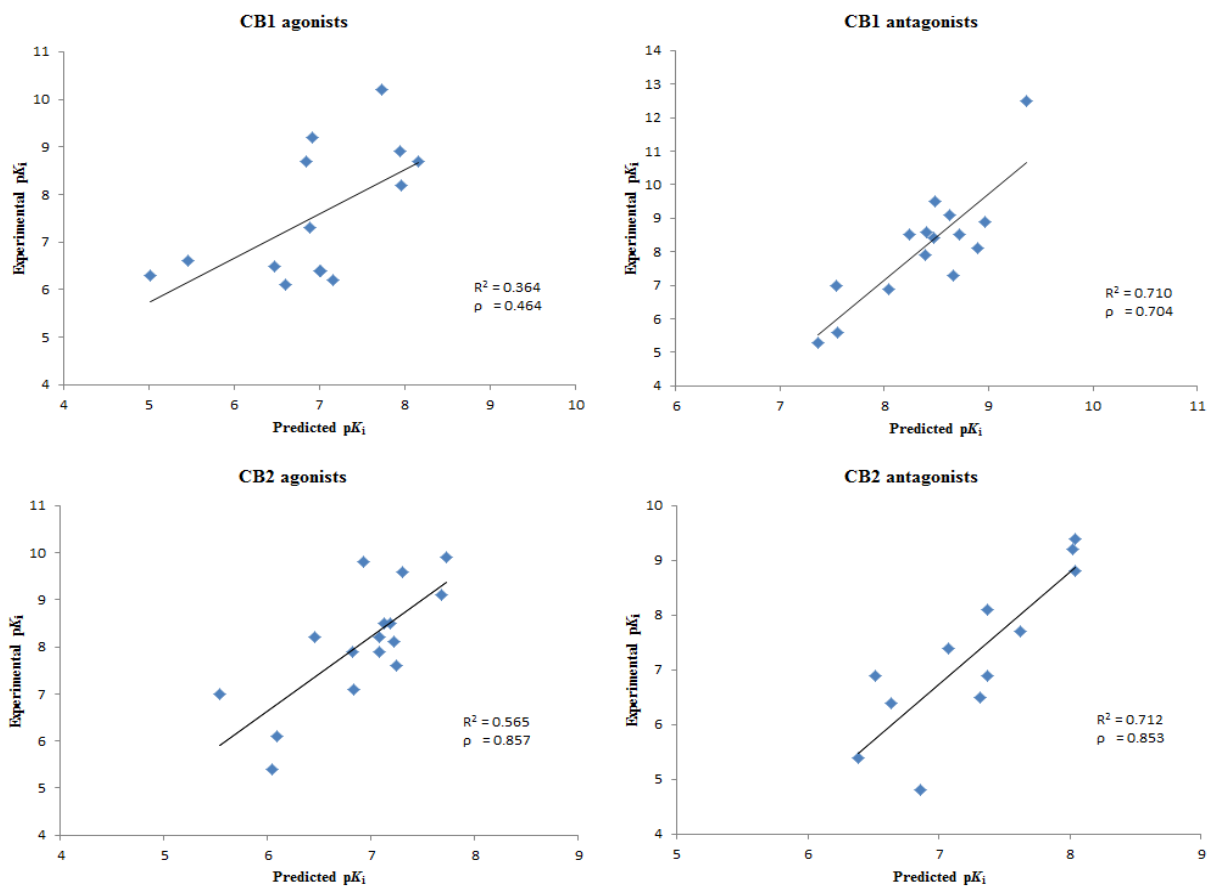
Figure 3-13 Correlation between predicted pKi values and experimental data. *Models were extracted from time step of 240.7ns and 96.0ns for the CB1 and CB2 receptor respectively. R^2 values and ρ values are displayed for each ligand set. For both coefficients, a value of 1.0 indicates perfect positive correlation, while a value of 0.0 indicates random distribution.*

For CB1, after removal of outliers, the R^2 value was 0.364 and the ρ value 0.464 for agonists, while for antagonists the R^2 value was 0.710 and the ρ value 0.704. For CB2, after removal of outliers, the R^2 value was 0.565 and the ρ value 0.857 for agonists, while for antagonists the R^2 value was 0.712 and the ρ value 0.853. These values indicated significant predictive power in the ranking of ligands based on potency and in predicting binding affinities, particularly for antagonist ligands. An analysis of the outliers removed showed that they consisted mostly of compounds with non-typical cannabinoid ligand scaffolds, or were compounds with significantly higher experimental binding affinities compared to other structurally similar compounds, thus likely indicating the scoring function applied was unable to account for the specific interactions that governed their high experimental binding affinity.

The higher correlation between predicted and experimental binding affinities of antagonist ligands (0.710 for antagonists versus 0.364 for agonists in CB1; 0.712 for antagonists versus 0.565 for agonists in CB2) was not entirely unexpected, as both models were constructed based on the inactive-state structure of the adenosine A2A receptor bound to an inverse agonist, and would arguably therefore be more likely to remain in a conformation favouring antagonist binding considering the nanosecond time scale of the simulations. Moreover, CB1 was simulated with the antagonist SR141716 bound, likely further biasing the conformations sampled towards the inactive state. These values were comparable with those from previous studies that assessed scoring functions using a wide range of protein-ligand crystal complexes, showing that even using experimental structures gave correlations of 0.5-0.7 at best (145–147). One interesting observation was that the ranges of predicted pK_i values were much smaller than their corresponding experimental range. This is also consistent with previous findings highlighting the fact that many scoring functions are unable to adequately predict the binding affinities of complexes with very high or very low affinities, and frequently underscore or overscore these complexes (147).

It should be noted that the ability of any particular docking evaluation to successfully predict binding affinities is a complex function governed by several factors besides the accuracy of the protein structure, such as the docking algorithm employed, scoring function used, and the ligand sets tested (144,145,240). While it would therefore be imprudent to conclude on the accuracy of our CB1 and CB2 models based on these results alone, they do provide some degree of confidence on the ability of our models to be used as a predictive tool in rational drug design.

3.3.2   Enrichment studies

All ligands described in section 3.3.1 were used as the active set (i.e. known binders), regardless of whether they were agonists or antagonists. For the decoys, a set of 1000 drug-like decoys which have been used in previous enrichment studies was downloaded from Schrödinger (132). In order to make the decoy set more comparable to the active set, due to the inherent limitation of current scoring functions which are biased towards compounds with high molecular weight (144,147,240,241), we applied a molecular weight cut-off of 500 Daltons to the decoy set, which resulted in a final decoy set of 837 molecules.

Both sets of ligands were then docked into both receptor models using the same procedure and docking parameters as previously described. The docked molecules were then ranked according to the lowest predicted binding energy obtained. ROC curves were then plotted and their corresponding AUCs calculated using GraphPad Prism. The results are presented in Figure 3-14.
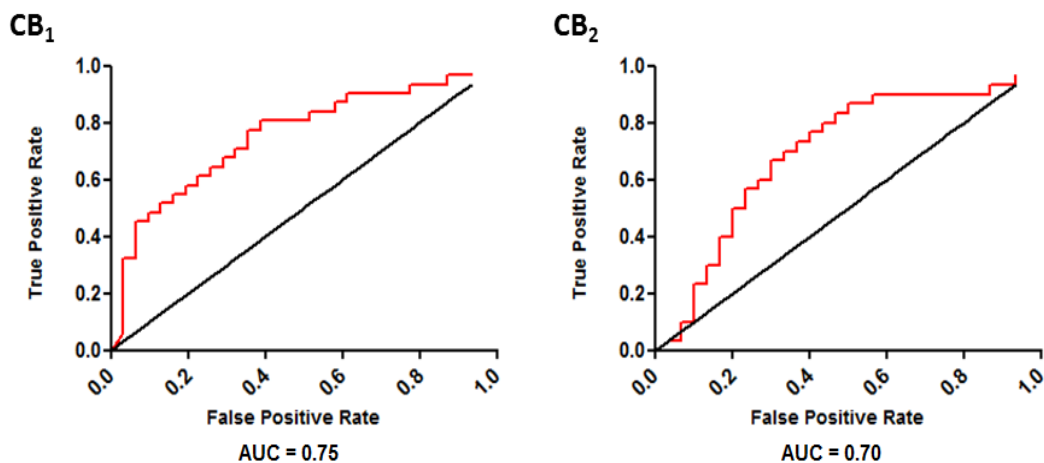
Figure 3-14 ROC curves for CB1 and CB2 receptor models. *The line of identity (black) represents the expected line in completely random selection, which would result in an AUC of 0.5.*

The AUC obtained for the ROC curves for CB1 and CB2 were 0.75 and 0.70 respectively, which indicate a significant ability to distinguish between the active compounds and the decoys. The higher AUC for CB1 compared to CB2, particularly when focusing on the top ranking compounds, was slightly unexpected considering the CB2 model performed better in binding affinity prediction and ranking power. An analysis of the top ranking decoys which contributed significantly to the false positive rate at the initial part of the test revealed them to be mostly compounds of high molecular weight (in excess of 450 Daltons), once again highlighting the limitations of current scoring functions and the need to account for such biases in enrichment/virtual screening protocols. The fact that our CB2 model was in the *apo* form, with an open binding pocket, as compared to our CB1 model which was simulated with a bound ligand (subsequently removed), resulting in a tighter binding pocket, could have contributed to these findings as these compounds likely experienced more penalties due to steric clashes when scored in the CB1 model. Based on the ROC curves obtained and taking into consideration the diversity the active set used which also included compounds with moderate binding affinities (pK_i values between 5 and 7), these enrichment studies provided additional support to the validity of our models in providing a reasonable representation of each receptor.
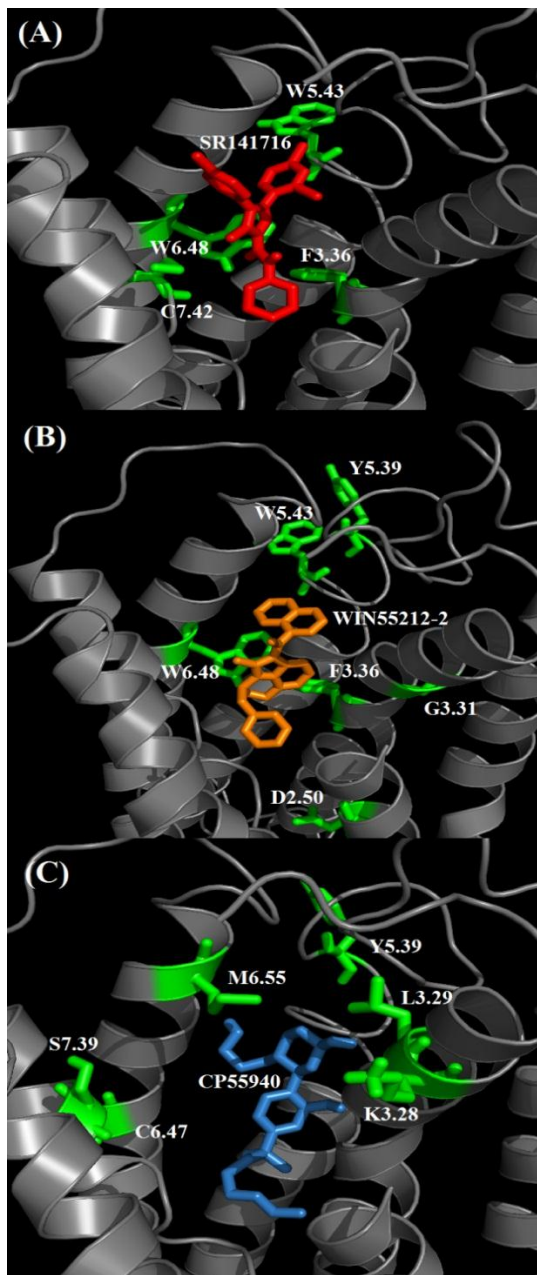
3.3.3   Binding mode assessment

3.3.3.1 Predicted binding of SR141716, WIN55212-2, and CP55940 to the CB1 receptor

The predicted binding poses of SR141716, WIN55212-2 and CP55940 in the CB1 receptor are shown in Figure 3-15, along with residues known to affect their binding through mutagenesis studies (see Appendix IV for full list of residues and references) (166,167,169,184,242–248). SR141716 showed interaction F3.36 and W6.48, with C7.42 in the close vicinity, but not W5.43. WIN55212-2 also showed interaction with F3.36 and W6.48, but not with D2.50, G3.31, W5.43, and Y5.39. CP55940 showed interaction with M6.55, but not with K3.28, L3.29, Y5.39, C6.47, and S7.39.

The predicted binding poses only showed interactions with some of the residues implicated via mutagenesis studies. In most cases, especially for agonists, many of these key residues did not appear to form part of the binding pocket or were not within interacting distance. For SR141716, which was re-docked and essentially reproduced the binding mode adopted throughout the simulations, only W5.43 did not interact with the ligand, and appeared to be directed towards the lipid bilayer. For WIN55212-2, the aromatic residues Y5.39 and W5.43 appeared to be directed towards the lipid bilayer, D2.50 was located deep within the binding pocket while G3.31 was also located on the side of TM3 facing the membrane. The interaction of SR141716 and WIN55212-2 with both F3.36 and W6.48 was encouraging, as there is strong evidence suggesting these two residues form a toggle switch that plays a crucial role in CB1 receptor activation (168). For CP55940, the only non-interacting residue forming part of the binding pocket was L6.52, while K3.28, Y5.39, C6.47 and S7.39 had conformations that precluded interaction with the ligand. Once again considering the bias of our model towards antagonist binding, these findings were not entirely unexpected. The conformation of K3.28, which seemed to be interacting with the phospholipid

headgroups of the lipid bilayer, is agreement with the hypothesis that arginine/lysine patches help anchor the receptor to the membrane (150).
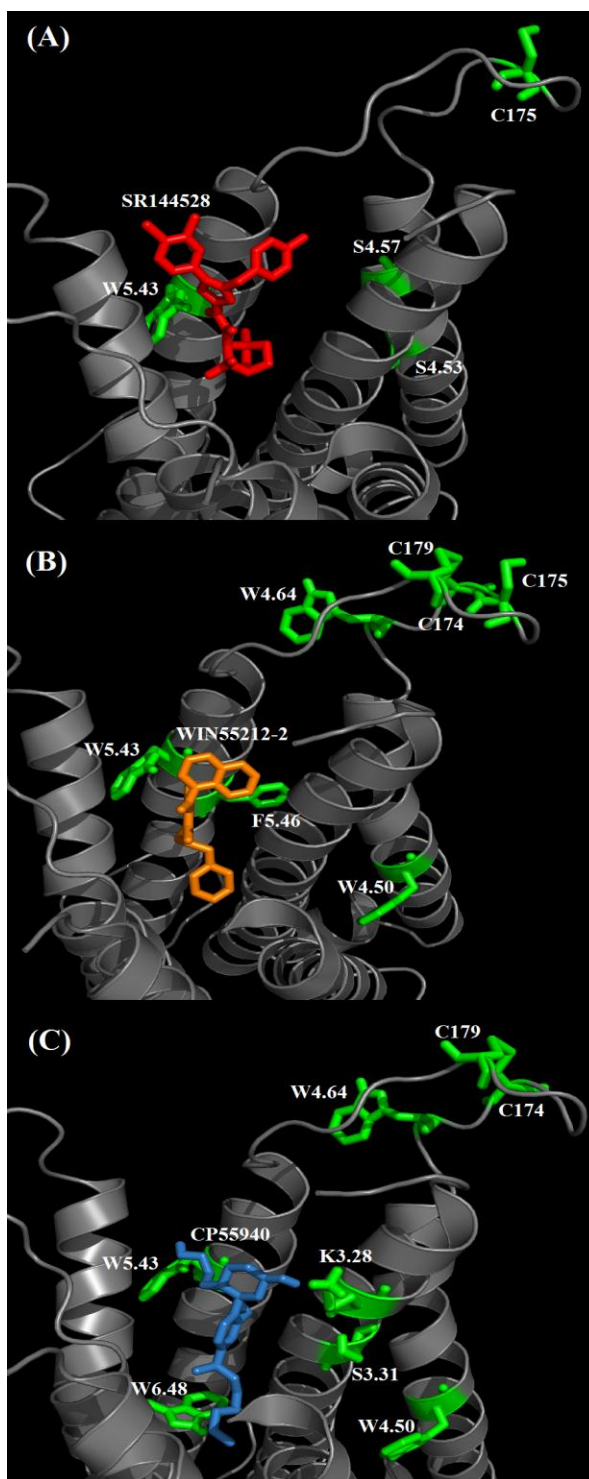

Figure 3-15 The predicted binding poses of selective CB1 antagonist SR141716 (A), CB1 agonist WIN55212-2 (B), and non-selective agonist CP55940 (C) to the cannabinoid CB1 receptor. *Residues known to affect ligand binding in mutagenesis studies are highlighted in green. Several residues in TM2 of the receptor have been removed to aid visualization. Only polar hydrogens are shown.*

Analysis of the predicted binding poses of other antagonist ligands of the diarylpyrazole class, such as SR144528, SR147778, and AM281, showed similar predicted binding poses to SR141716 (data not shown).

3.3.3.2 Predicted binding of SR144528, WIN55212-2, and CP55940 to the CB2 receptor

The predicted binding poses of SR144528, WIN55212-2 and CP55940 in the CB2 receptor are shown in Figure 3-16, along with residues known to affect their binding through mutagenesis studies (see Appendix IV for full list of residues and references) (164–166,170,171,249–255). The binding mode for SR144528 showed interaction with W5.43 but not S4.53, S4.57, and C175. WIN55212-2 showed interaction with W5.43, but not C174, C175, C179, F5.46, W4.50 and W4.64. CP55940 showed interaction with W5.43 and W6.48, but not C174, C179, K3.28, S3.31, W4.50 and W4.64.

Figure 3-16 The predicted binding poses of selective CB2 antagonist SR144528 (A), selective CB2 agonist WIN55212-2 (B), and non-selective agonist CP55940 (C) to the cannabinoid CB2 receptor. *Residues known to affect ligand binding in mutagenesis studies are highlighted in green. Several residues in TM2 of the receptor have been removed to aid visualization. Only polar hydrogens are shown.*

As in the CB1 receptor, the predicted binding poses showed interaction with only some of the residues implicated in their binding. However, the predicted interaction of all three ligands with W5.43, particularly hydrogen bonding between W5.43 and CP55940, was highly encouraging as this residue has been shown to be crucial in the binding of all three ligands (171). Several key residues were not located within the binding pocket and were not within interacting distance. For SR144528, S4.53 and S4.57 appeared to be interacting with and stabilizing TM3, while the conformation of the 2nd extracellular loop did not allow interaction of C175 with the ligand in the binding pocket. Loop conformations, particularly of those longer than ten residues, are extremely hard to predict due to their flexibility, and are thus often missing from crystal structures. Similarly, for WIN55212, C174, C175, C179 and W4.64 are all located within the second extracellular loop and not within range for ligand interaction. F5.46 and W4.50 did not appear to be extending into the binding pocket, though F5.46 was found to be within interacting range with F3.36, which was in turn found to be interacting with the ligand. These residues, along with F3.25 and W5.43, have been previously proposed to form an aromatic stacking network with WIN55212-2 (165). For CP55940, the residues K3.28, S3.31, and W4.50 were all either not located in the binding pocket or had side chain orientations that did not allow for interaction with the ligand. Interestingly, both agonists WIN55212-2 and CP55940 were here found to be individually interacting with both residues of the F3.36/W6.48 toggle switch, which themselves were interacting as expected in our inactive state model.

Analysis of the predicted binding poses of other antagonist ligands of the same diarylpyrazole class as SR144528, such as SR141716, SR147778, and AM281, showed similar predicted binding poses (data not shown). Additionally, most of the ligands docked showed interactions with V6.51, L6.52, M6.55 and L6.59, which have been experimentally shown to be accessible within the ligand binding site crevice (252).

3.3.3.3 Binding mode assessment conclusions

While it is possible to attribute the ability of some of the key residues described to affect ligand binding in mutagenesis studies to subtle changes in the global conformation of the receptor rather than conclude that they are in an incorrect conformation in our model, in the absence of a crystal structure neither claim can be positively confirmed. Certainly, residues in the second extracellular loop such as C174 and C179 in the CB2 receptor, which have been postulated to form a disulphide bridge, have been predicted to likely affect the receptors helix conformation rather than influence ligand binding directly (160,170). An additional point of note is that the predicted poses did not take into account possible hydrogen bonding networks through water molecules in the binding site, due to the difficulty in predicting the location of structural waters. As such, based on the evidence presented here, we conclude that although predicted binding modes should be treated with some degree of caution, our constructed models were found to generally be in agreement with experimental data.

3.3.4   Further investigations into the construction of a validated CB1 homology model

In light of the poorer validation results of our CB1 model in the prediction of binding affinities, particularly for CB1 agonists, we attempted to extract and validate further models from our molecular dynamics simulations of CB1 using different selection criteria, widening the scope of our initial conformational search.

Receptor conformations of the CB1 receptor in our MD simulations were first clustered using a RMSD tolerance of 0.95Å. The 8 largest clusters, including those formed before protein backbone RMSD stabilization, were selected for analysis. The lowest energy conformation and the conformation with the lowest average distance to other conformations within the cluster were extracted from each of the eight clusters selected. An additional 8 conformations were also

extracted randomly from the simulation, bringing the total number of structures to 24. Known ligands were then docked into structure in the same validation procedure.

While the majority of the structures extracted showed extremely poor correlations between experimental and predicted binding affinities, one model (time step of 245.1ns) performed reasonably with a R^2 value of 0.83 for antagonist ligands. However, correlation for agonist ligands was significantly poorer at 0.01, once again highlighting the likelihood of our treatment of the CB1 receptor with SR141716 in the binding site biasing the simulation towards inactive-state dynamics. It was also noteworthy that the simulation time this model was extracted from was similar to our previous best-performing model (time step of 240.7ns, R^2 of 0.36 for agonists and 0.71 for antagonists). Taking into account that the fenofibrate derivatives to be investigated include agonist and antagonist ligands, the previously validated model was deemed more suitable for further use.

4 STRUCTURE-BASED DESIGN OF NOVEL FENOFIBRATE DERIVATIVES AS POTENTIAL CANNABINOID RECEPTOR LIGANDS

4.1 Binding mode prediction of fenofibrate amide derivatives

A series of fenofibrate amide derivatives, consisting of a mixture of agonists and antagonists with varied binding affinities to the cannabinoid receptors, as described in Tables 1-2 and 1-3, was docked into our validated models using the procedure described in section 8.1. The lowest energy conformations of each derivative obtained from docking were then extracted; applying a consensus approach in conjunction with binding affinity and mutagenesis data from literature allowed us to determine the most probable binding modes. Analysis of the lowest energy conformations of these derivatives at the CB2 receptor in particular yielded a prominent binding mode and key interactions supported by pharmacological data, and will therefore be discussed first.
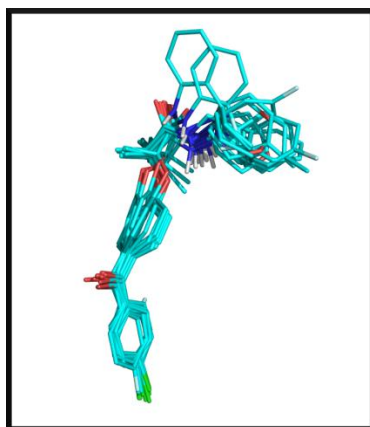
4.1.1 Binding of fenofibrate derivatives to the CB2 receptor

The binding site for fenofibrate derivatives to the CB2 receptor appeared to be a Y-shaped pocket located primarily between TM2, TM3, TM5 and TM6, as shown in Figure 4-1. All ligands docked were predicted to bind within this pocket, with an orientation such that the benzophenone moiety was located at the bottom of the pocket, while the carboxamide N-substituent resided in either branch at the upper end of the pocket. No obvious differences were noted in the predicted binding modes of agonists and antagonist derivatives.
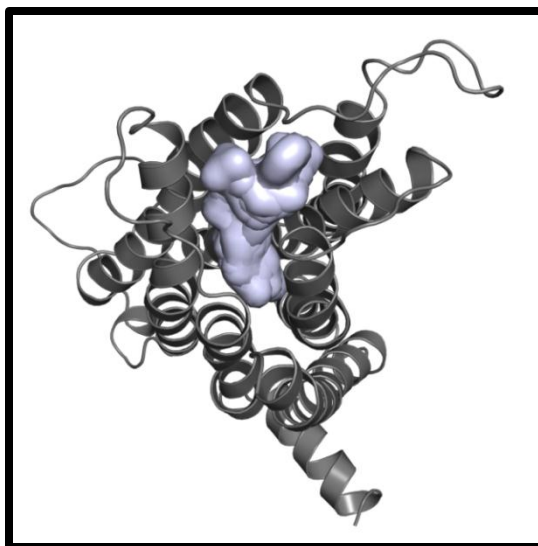
Figure 4-1 The predicted binding pocket for fenofibrate derivatives in the CB2 receptor

Analysis of the lowest energy poses obtained from the docking of derivatives where experimental binding affinities were available revealed one particularly prominent conformation, which was adopted by 80% of the most potent compounds ($pK_i > 7$) and 50% of all derivatives with good agreement. In this predicted binding mode, the ligands adopted a curved conformation with their carboxamide N-substituent directed towards TM3. The excellent overlap between all compounds adopting this predicted conformation is shown in Figure 4-2.

Figure 4-2 Overlap between all fenofibrate derivatives predicted to adopt a curved conformation when binding to the cannabinoid CB2 receptor.

Visualization of the surrounding residues allowed the identification of possible key interactions in maintaining this conformation. This binding mode and the postulated key interactions are shown in Figure 4-3, using a single reference compound **24g** as an example.
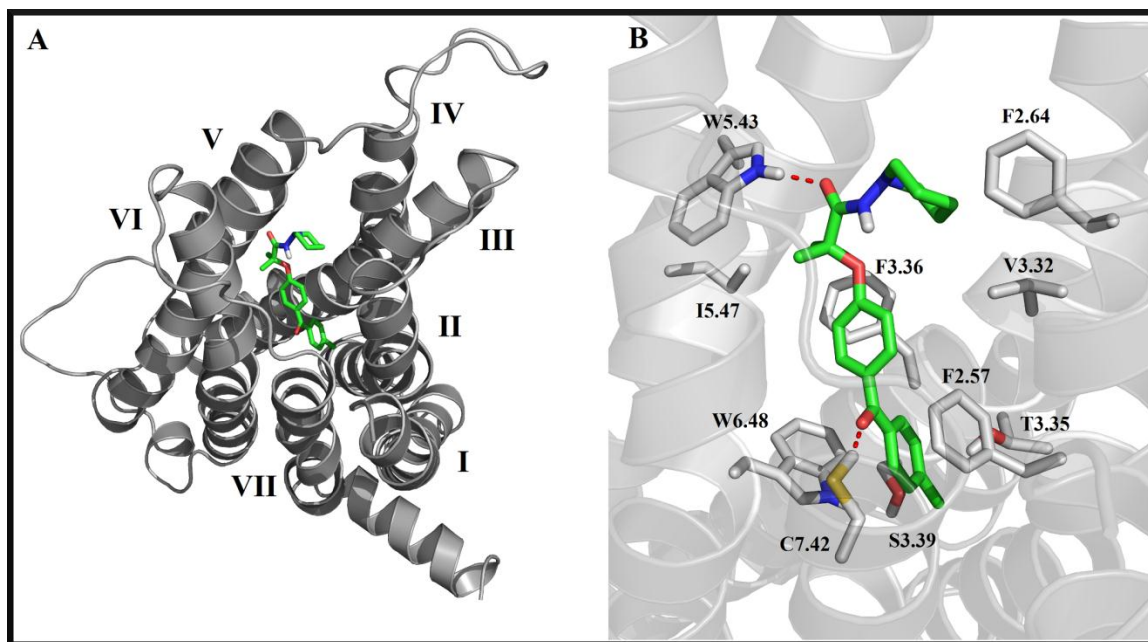

Figure 4-3 Predicted binding conformation of fenofibrate derivatives to the CB2 receptor (A), along with the key interactions involved (B). *The reference structure shown is compound **24g**. Hydrogen bonds are shown in red dashed lines. Only polar hydrogens are explicitly shown.*

Firstly, in this conformation key hydrogen bonding interactions are formed between the carboxamide of each derivative and W5.43, as well as the benzophenone carbonyl with C7.42. Mutagenesis studies have recently shown W5.43 to play a critical role in the binding of CP55940, WIN55212-2 and SR144528 to the CB2 receptor, further supporting our prediction of a key hydrogen bond between fenofibrate derivatives and this residue (171). On the other hand, C7.42A mutation in the CB1 receptor did not affect ligand binding, but labeling of this residue using methanethiosulfonate precluded antagonist binding, possibly by introducing steric bulk, indicating

that C7.42 may be involved in ligand binding but may not be crucial (184). Although the study did not include the equivalent CB2 mutant, the conserved nature of both receptors would suggest that by extension, C7.42 may play a role in ligand binding in CB2 or is at least accessible within the binding site, as found in our model. Secondly, both benzophenone rings engage in aromatic (π-π) stacking interactions with F2.57, F3.36 and W6.48. Site-directed mutagenesis data involving W6.48 in CB2 have shown that it is likely involved in the binding of CP55940 (256). Data for these residues in CB1 was also suggestive of their importance, with the binding of SR141716 and WIN55212-2 shown to be affected by both F3.36A and W6.48A mutations (167). Furthermore, it is widely accepted that the formation of aromatic microdomains play an important role in ligand binding at the cannabinoid receptors, reinforced by modeling studies that postulate a F3.36/W6.48 rotamer toggle switch is involved in receptor activation (154,168). The predicted interaction of fenofibrate derivatives with both of these residues was therefore encouraging, although the similar poses obtained for both agonist and antagonist derivatives (some of which differed in structure only by the position of a single substituent) indicated that our model was unable to capture some of the minor intricacies that impart efficacy to these compounds. Thirdly, the carboxamide N-substituent of each derivative appeared to reside in a hydrophobic pocket demarcated primarily by F2.64 and V3.32, which did not possess any corresponding mutagenesis data. Derivatives with the more lipophilic cyclic substituents attached to the carboxamide nitrogen docked more readily into this region. Along with interaction of the dimethyl group with I5.47, this indicates that hydrophobic contacts with these residues may also be central to maintaining the predicted conformation, which is line with previous findings of many potent cannabinoid ligands being high molecular weight compounds with substantial hydrophobic character (83,257). Finally, the contrasting presence of polar residues such as T3.35 and S3.39 at the bottom of binding pocket was noteworthy, with derivatives possessing *para* substitutions on the benzophenone ring showing the greatest steric complement. Pharmacological data of the known fenofibrate amide derivatives showed derivatives

with substitutions in the *ortho* and *para* positions all displayed some degree of agonism, suggesting interaction with these polar residues may play a role in imparting functional activity.

An alternate "extended" conformation was also observed, and is shown in Figure 4-4 using a different reference compound, though this conformation was less prominent in terms of its frequency of occurrence and key interactions involved. The key interactions appeared to be mainly a hydrogen bond formed between the carboxamide bond and D5.38 and aromatic stacking of the second benzophenone ring with F2.57 and W6.48.
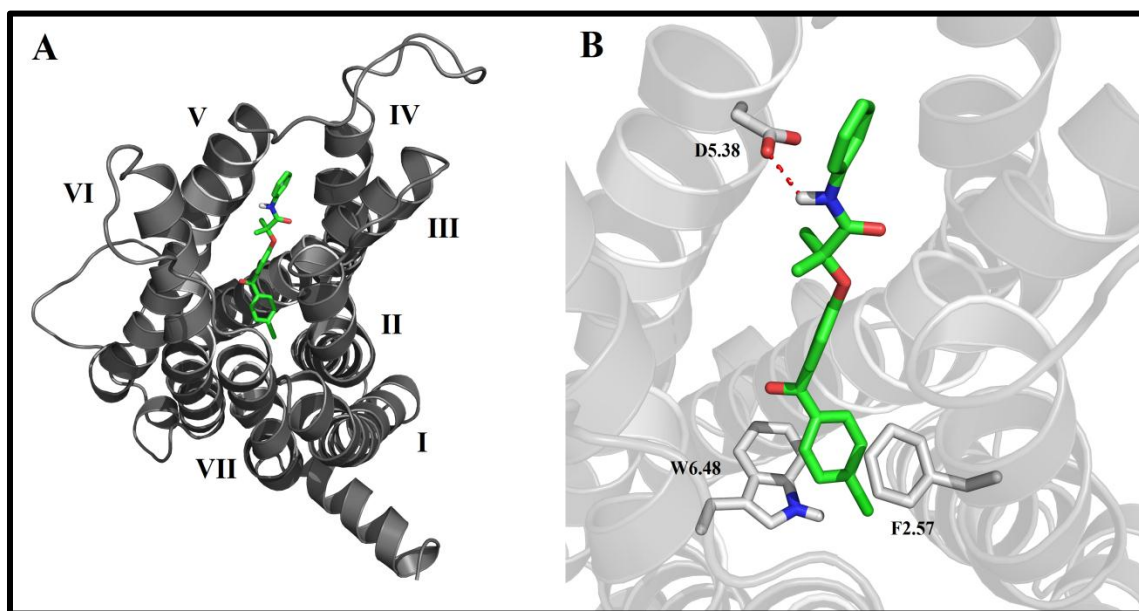

Figure 4-4 Alternate "extended" conformation for fenofibrate derivatives binding to the cannabinoid CB2 receptor. A) Position of extended conformation within the binding pocket. B) Key interactions involved in maintaining the extended conformation. *The reference compound shown is compound 24n.*

While we have successfully identified a possible binding mode for fenofibrate derivatives to the CB2 receptor, there were inevitably several caveats of note. For one, our model showed no significant difference in the binding of agonist and antagonist fenofibrate derivatives as previously

highlighted. Secondly, the correlation between experimental pK_i values and those predicted by docking these derivatives was generally poor, with a corresponding R^2 value of 0.16, as almost all compounds were predicted to bind with high affinity ($pK_i > 7$). Both these observations are attributable to the fact that most of these derivatives are very similar in terms of structure, having been based on the same fenofibrate scaffold. The inherent limitations of current docking programs and the protocol chosen, in this case the utilization of grid-based potentials (i.e. docking to a rigid receptor), the use of an empirical scoring function, and the standard error in calculating binding free energies (~ 2.5kcal/mol) may have also contributed to these findings.
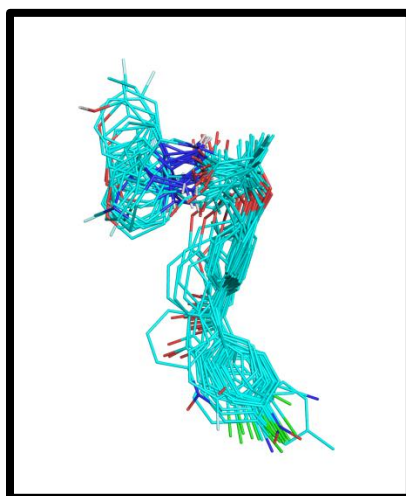
4.1.2 Binding of fenofibrate derivatives to the CB1 receptor

In contrast to the CB2 receptor, docking of fenofibrate derivatives to the CB1 receptor did not produce any particularly prominent conformation. All derivatives bound to a T-shaped binding pocket located between TM2, TM3, TM5, TM6, and TM7 (Figure 4-5). As experimental data on binding affinity was scarce for the CB1 receptor, all derivatives were taken into account when analyzing the conformations extracted.
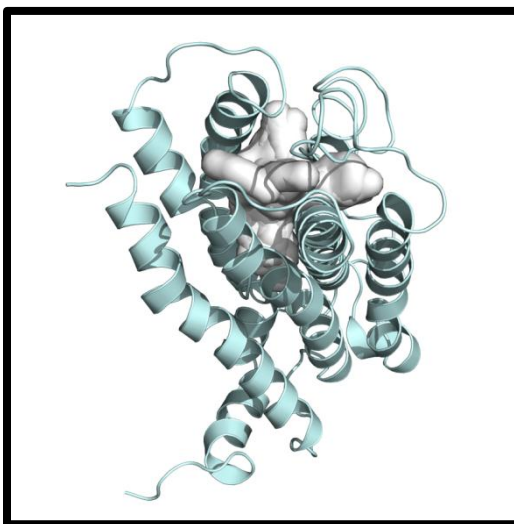
Figure 4-5 The predicted binding pocket for fenofibrate derivatives in the CB1 receptor

The lowest energy conformations of the fenofibrate derivatives did not exhibit any prominent consensus in terms of binding mode, and bound in a variety of orientations within the binding pocket. Some of these conformations were also deemed improbable, such as those found with the ligand protruding out of the helix bundle through the interhelical space between TM3 and TM5. Efforts were thus focused mainly on low energy conformations with an orientation such that the benzophenone moiety was located at the bottom of the binding pocket, based on previous observations with the CB2 receptor. Applying this criterion, the conformation that occurred at the highest frequency (75% of derivatives) was found to be a curved conformation similar to that observed in the CB2 receptor, but with the carboxamide N-substituent oriented towards TM6 instead of TM3. Overlap between the derivatives possessing this conformation was found to be relatively poor when compared to the predicted binding mode in the CB2 receptor (Figure 4-6).

Figure 4-6 Overlap between all fenofibrate derivatives predicted to adopt a curved conformation when binding to the cannabinoid CB1 receptor.

This binding conformation and the key interactions involved in this conformation are shown in Figure 4-7. The carboxamide N-substituent of the fenofibrate derivatives were once again placed in a hydrophobic pocket, which in CB1 were formed by residues F5.42, W6.48, L6.51, L6.52 and M6.55. For the residues L6.51, L6.52 and M6.55, the corresponding CB2 residues have been shown to be on the solvent-accessible surface in the binding site crevice, suggesting that their position in CB1 is likely to be similar (252). Site-directed mutagenesis studies have also shown W6.48 to play a role in SR141716A and WIN55212-2 binding (167). The carboxamide group did not appear to make any specific interactions, while the dimethyl group was found to interact mainly with V3.32 and T3.33. The only other interactions of note were between the benzophenone carbonyl and W6.48, and aromatic stacking of the second benzophenone ring with F2.57. The residue F3.36, which was also linked to SR141716A and WIN55212-2 binding, interactions between ligand and residue appeared to be non-specific in nature (167). The bottom of the binding pocket was found to be also predominantly polar in nature, formed mainly by D2.50, S3.39, N7.45, and S7.46. Overall, while this constitutes key interactions and a possible binding mode for fenofibrate derivatives to the CB1 receptor, the lack of a defined orientation for the derivatives, poor overlap between derivatives predicted to adopt this conformation, and limited support from site-directed mutagenesis studies indicated that these findings should be at the very least treated with some degree of caution.
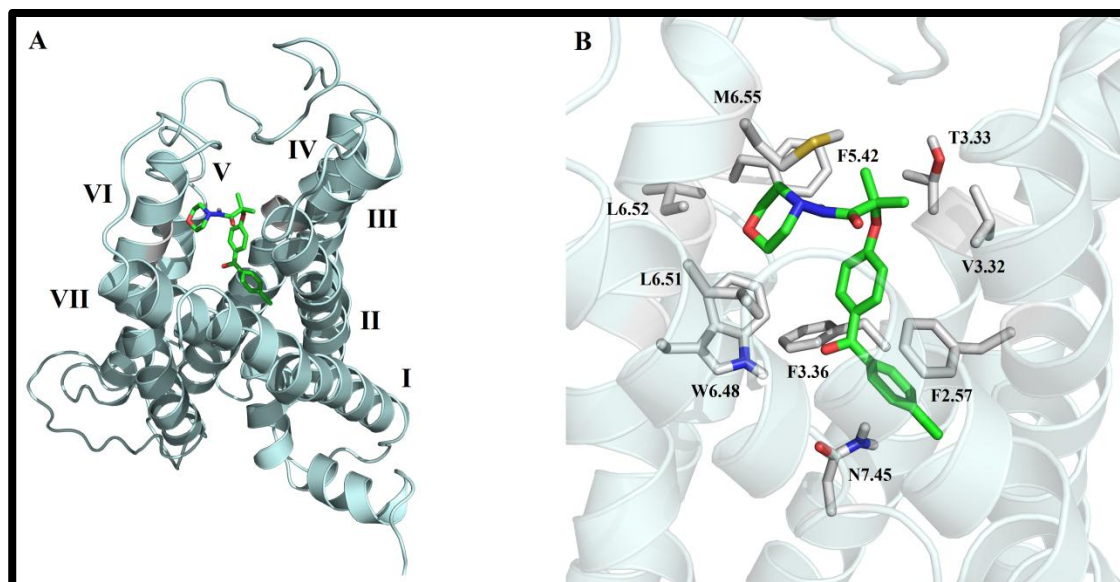
Figure 4-7 Predicted binding conformation of fenofibrate derivatives to the CB1 receptor (A), along with the key interactions involved (B). *The reference compound shown is **24h**. Only polar hydrogens have been explicitly shown.*
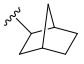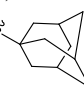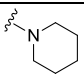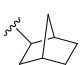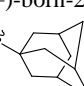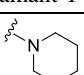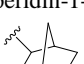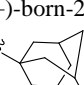
4.2 Structure-based design of novel ligands potentially binding to the CB2 receptor

In light of these findings and taking into consideration the robustness of the binding mode predictions for both receptors, efforts in designing novel ligands were focused primarily on the CB2 receptor. Utilizing compound **24g** as a lead, modifications were made to the ligand in order to increase the complement between ligand and receptor whilst maintaining the predicted binding mode and key interactions. Specifically, compound **24g** was revised with a view to:

- Increase the hydrophobic bulk of the carboxamide N-substituent using cyclic moieties
- Increase the polarity and hydrogen-bonding capacity of the 4-substituted benzophenone in order to complement the polar region of the binding pocket.
- Reduce loss of configurational entropy upon binding by rigidifying derivatives in the predicted conformation

A series of compounds was thus derived using these strategies and were subsequently modelled and docked into the validated CB2 receptor model using the previously established protocol. The final series of compounds selected for synthesis was made following assessment of their ability to allow for a detailed evaluation of the binding mode hypothesis and the structure-based design strategies employed, ease of synthesis, and the commercial availability of starting materials; this selection is shown in Table 4-2 and Figure 4-8.
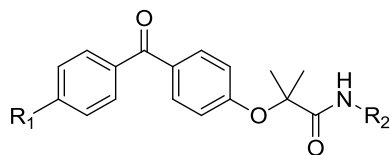
No	R_1	R_2
30a	Cl	*exo*-norborn-2-yl
30b	Cl	*R*(+)-born-2-yl
30c	Cl	adamant-1-yl
31a	CF_3	piperidin-1-yl
31b	CF_3	*exo*-norborn-2-yl
31c	CF_3	*R*(+)-born-2-yl
31d	CF_3	adamant-1-yl
32a	OH	piperidin-1-yl
32b	OH	*exo*-norborn-2-yl
32c	OH	*R*(+)-born-2-yl
32d	OH	adamant-1-yl

Table 4-2 Novel fenofibrate derivatives selected for synthesis and pharmacological evaluation. *Derivatives were designed with an aim to increase the hydrophobic bulk of the carboxamide N-substituent with cyclic moieties and to increase polarity in the benzophenone 4-position.*
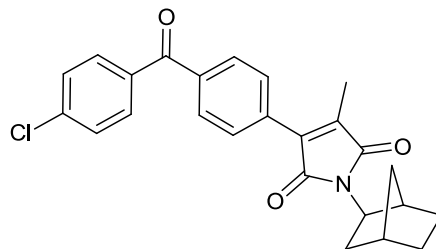
33

Figure 4-8 Novel maleimide derivative designed to reduce loss of conformational entropy upon binding to the CB2 receptor.

Figure 4-9 illustrates the predicted binding of several of these compounds when compared to reference compound **24g**. The piperidinyl and norbornyl compounds (**30a, 31a, 32a-b**), with the exception of **31b,** were all predicted to maintain the binding conformation and the associated key interactions. Conversely, the bornyl and adamantly derivatives (**30b-c, 31c-d, 32c-d**) did not bind similarly, only accessed the predicted binding mode at higher energy levels, and even then were frequently unable to maintain key hydrogen bonds with W5.43 and C7.42. Nevertheless these compounds were still selected for synthesis and pharmacological evaluation, as previous work by Pasquini *et al.* and Baraldi *et al.* have shown the carboxamide-adamantyl moiety to be advantageous in developing potent CB2-selective agonists (115,116). The inclusion of these compounds would also serve to highlight the importance of some degree of leniency, expert intervention, or the utilization of a consensus approach in interpreting the docking results obtained, particularly since a rigid receptor model was employed.
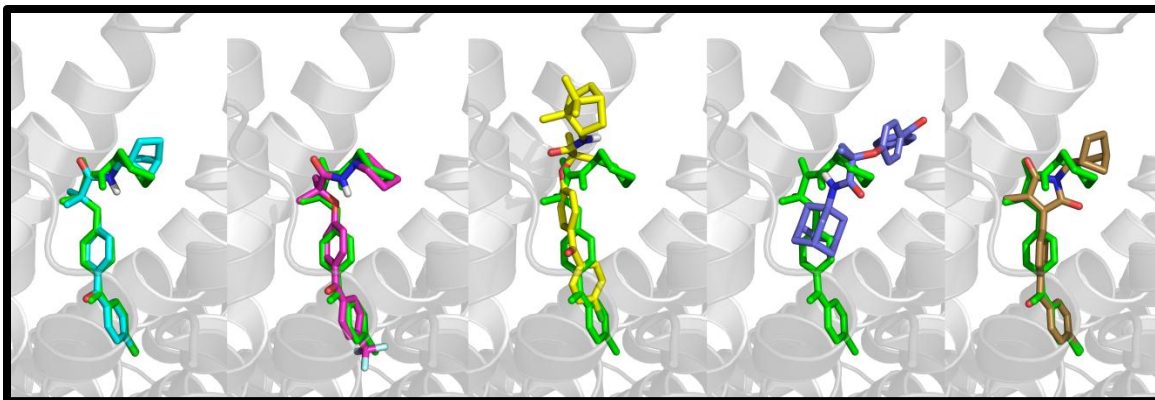
Figure 4-9 Predicted binding conformation of **30a** (cyan), **31a** (magenta), **30b** (yellow), **32d** (purple) and **33** (brown) in reference to **24g** (green).

Compound **33** was also of particular interest, as fusion of the amide bond and dimethyl ether linkage into a maleimide ring did not affect the predicted binding mode when this compound was docked into our CB2 model. The amide bond is a consistent feature of many prominent CB1 and CB2 ligands, particularly when coupled to a group with high hydrophobicity, as seen in SR141716A, SR144528, GW842166X, and previously described CB2 selective 4-quinolone-3-carboxylic acid, oxazinoquinolone, and heteroarylpyridine/ heteroarylpyrimidine derivatives (115–117). The synthesis and pharmacological characterization of **33** would not only represent a successful case of structure-based design providing a new scaffold for the derivation for further structure-activity relationships, but would also lend further support to the hypothesized binding mode due to its reduced structural flexibility and propensity to adopt the predicted conformation.

5 SYNTHESIS OF NOVEL FENOFIBRATE DERIVATIVES AS POTENTIAL CB2 RECEPTOR LIGANDS

5.1 Synthesis of novel amide derivatives of fenofibrate

34a: R = Cl
34b: R = CF$_3$

35a: R = Cl
35b: R = CF$_3$

36a: R = Cl
36b: R = CF$_3$
36c: R = OH

37a: R = Cl
37b: R = CF$_3$
37c: R = OH

22: R = Cl
38a: R = CF$_3$
38b: R = OH

30a: R$_1$ = Cl, R$_2$ = *exo*-norborn-2-yl
30b: R$_1$ = Cl, R$_2$ = *R*(+)-born-2-yl
30c R$_1$ = Cl, R$_2$ = adaman-1-tyl
31a: R$_1$ = CF$_3$, R$_2$ = piperidin-1-yl
31b: R$_1$ = CF$_3$, R$_2$ = *exo*-norborn-2-yl
31c: R$_1$ = CF$_3$, R$_2$ = *R*(+)-born-2-yl
31d: R$_1$ = CF$_3$, R$_2$ = adaman-1-tyl
32a: R$_1$ = OH, R$_2$ = piperidin-1-yl
32b: R$_1$ = OH, R$_2$ = *exo*-norborn-2-yl
32c: R$_1$ = OH, R$_2$ = *R*(+)-born-2-yl
32d: R$_1$ = OH, R$_2$ = adaman-1-tyl
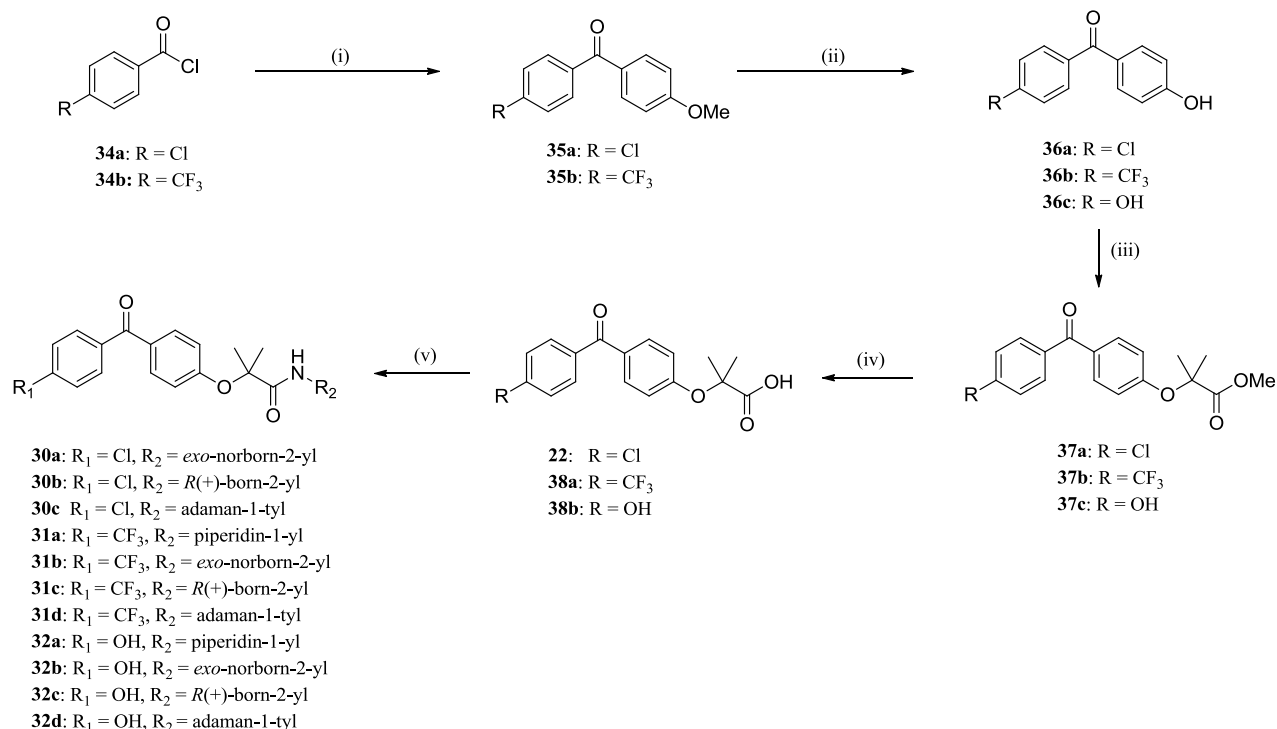
Scheme 1 Synthesis of fenofibrate derivatives **30a** to **32d.** Reagents and conditions: i) AlCl$_3$, anisole, DCM, N$_2$, 24h; ii) Pyridine.HCl, microwave irradiation, 16 min; iii) Methyl-2-hydroxyisobutyrate, PPh$_3$, DIAD, N$_2$, MeCN, reflux, 15h; iv) NaOH, THF/water 1:1, 6-24h; v) Selected amine, Et$_3$N, HBTU, 4-24h

The synthesis of the novel compounds designed retaining the original fenofibrate amide scaffold was achieved as outlined in **Scheme 1**. The synthetic route employed had previously been demonstrated to be successful in the synthesis of other fenofibrate amide derivatives (179). Starting from the commercially available 4-substituted benzoyl chlorides (**34a,b**), these were reacted with anisole in the presence of AlCl$_3$, under standard Friedel-Crafts conditions to produce the required 4,4'-disubstituted benzophenone. While the methoxy group of anisole is electron-donating and

would therefore be expected to be both 2- and 4-directing in electrophilic aromatic substitution, the desired 4,4'-disubstituted benzophenone isomers **35a,b** was obtained in good yield (~80%) in both cases, likely due to steric effects hindering substitution at the 2-position.

Subsequent demethylation of aryl methyl ether using more conventional methods (BBr$_3$ in DCM) have been previously shown to be unsuccessful, and as such was achieved via neat microwave irradiation in the presence of pyridine hydrochloride as first demonstrated by Kulkarni *et al* (179,258). Yields were inconsistent when the reaction was conducted in a conventional microwave oven at constant power of 220W as espoused by the original study. Utilization of a specialized microwave reactor at variable power and constant temperature subsequently improved reaction efficiency. It was noteworthy that while reaction temperatures were initially selected solely based on the melting point of the substituted benzophenone in order to allow mixing with pyridine hydrochloride, there appeared to be a critical temperature for the reaction to progress that was independent of the melting point of the reactant and microwave power. This observation was consistent with the findings of studies attributing the contribution of microwave irradiation to accelerate certain reactions to be completely thermal in nature (259). 4,4'-Dihydroxybenzophenone (**36c**) was obtained commercially.

Alkylation of the exposed phenol through Williamson ether synthesis to generate the required fenofibric acid derivatives, although previously demonstrated by Spencer *et al* (179), proved to be unsuccessful, and can be attributed to the tertiary nature of the alkyl halide required in the reaction precluding effective S$_N$2 nucleophilic substitution. Consequently, syntheses of the corresponding methoxy esters **37a-c** were achieved using a variant of the Mitsunobu reaction (with DIAD and triphenylphosphine) at *elevated* temperatures of 80-100°C that has been previously shown to be successful in the synthesis of tertiary alkyl-aryl ethers (260). Due to solubility issues, the solvent was changed from toluene in the original study to acetonitrile, and the reaction was

conducted under reflux. The reaction gave moderate yields of 50-70% following purification for the halogenated derivatives **37a,b** but was poorer (~30%) for the hydroxyl substituted derivative **37c**; this resulting from the formation of the disubstituted alkyl-aryl ether and difficulty in purification owing to the product possessing a R_f similar to that of reduced DIAD from the reaction. Cleavage of the methoxy ester in base-catalysed ester hydrolysis then afforded fenofibric acid **22** or its derivatives **38a,b**.

The final desired compounds **30a-32d** were then obtained via amide coupling between the fenofibric acid derivative and the corresponding amine using HBTU in the presence of triethylamine. Excellent yields (> 90%) were once obtained for the halogenated derivatives **30a-31d** but was poorer (~30%) for the hydroxyl derivatives **32a-d**. Following purification using a combination of radial thin layer chromatography and recrystallization, the structures of the final compounds were confirmed using NMR, FTIR, and HRMS, while purity of 95% or higher was confirmed using analytical HPLC.

5.2　Synthesis of a novel maleimide derivative of fenofibrate
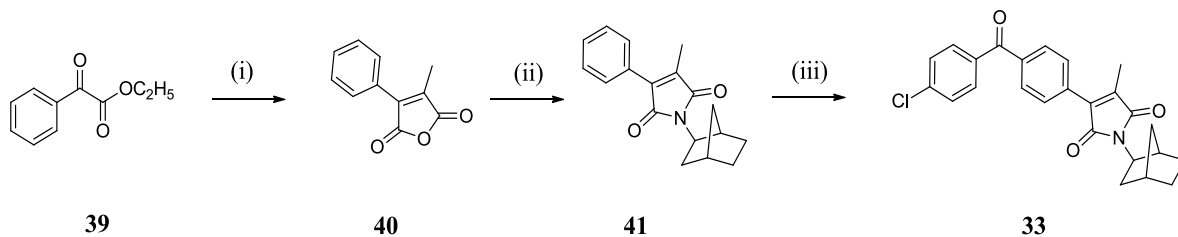
Scheme 2 Synthesis of fenofibrate maleimide derivative **33.** Reagents and conditions: i) propionic anhydride, TiCl$_4$, *n*-Bu$_3$N, DCE, reflux, 12h; ii) *exo*-2-aminonorbornane, HMDS, ZnI$_2$, toluene, reflux, 3.5h; iii) 4-chlorobenzoyl chloride, AlCl$_3$, DCM, r.t.

The synthesis of the novel maleimide derivative of fenofibrate **33** was attempted using the synthetic route shown in Scheme 2. As previously demonstrated by Kishorebabu *et al* (261), 2-methyl-3-phenylmaleic anhydride **40** was synthesized from ethyl benzoylformate and propionic anhydride using a titanium (IV) chloride/tributylamine system. Despite identical reaction conditions, the yield obtained was significantly lower than that reported in the original study (28% vs 81%). Conversion of the maleic anhydride to a maleimide and coupling of norbornyl moiety was achieved in a single step using the method shown by Reddy *et al* (262), with ZnI$_2$ as a Lewis acid and 1,1,1,3,3,3-hexamethyldisilazane (HMDS), giving the maleimide **41** in an excellent yield of 86%.

Subsequently, we attempted to synthesize **33** from **41** using the same classic Friedel Crafts conditions that were previously successful in the synthesis of substituted benzophenones. This proved unsuccessful, with no reaction progress recorded even after doubling the reaction time to 48 hours. This observation could possibly be attributed to the highly conjugated nature of the maleimide deactivating the aryl via electron delocalization, precluding nucleophilic attack on the acylium ion intermediate. As such, we attempted to utilize variations of the Friedel Crafts reaction that have been shown to be more efficient and effective even on deactivated systems. Microwave

irradiation in the presence of zinc powder (263) produced several products, none of which showed a mass/charge ratio consistent with the desired product in HRMS analysis. A neat reaction with zinc oxide, which has been previously shown to be effective even with highly deactivated compounds such as nitrobenzene (264), was also unsuccessful with no reaction progress recorded. At the time of writing the synthesis **33** was incomplete, and will be discussed in future publications.

6 PHARMACOLOGICAL EVALUATION OF NOVEL FENOFIBRATE DERIVATIVES AT THE CB2 RECEPTOR

6.1 [^{3}H]CP55940 competition binding assay and [^{35}S]GTPγS binding assay

Compounds **30a-32d** (Table 4-2) were assayed for binding affinity and functional activity at the human CB2 cannabinoid receptor. Binding affinity was determined in a competition binding assay using [^{3}H]CP55940 as the radioligand. Efficacy was determined using the [^{35}S] GTPγS binding assay. All assays were conducted using membrane homogenates of CHO cells transfected with recombinant human CB2 receptors, using the same protocol as Spencer *et al* (179) to ensure consistency and comparability of results, with the exception that full response curves were generated for the functional assay. The results of this assay were additionally expressed as a percentage of the maximum response achievable to provide an indication of the degree of agonist response obtained, which was indeterminable from the study by Spencer *et al*. The results of both assays are presented in Tables 6-1.
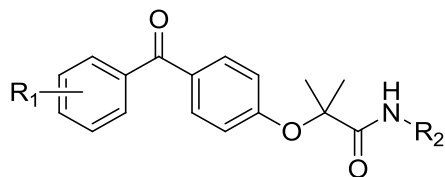
No	R_1	R_2	pK_i at CB2 [a]	% Maximal displacement	% CB2 activation at 10 μM	pEC_{50}/pIC_{50} [b]	E_{max} (%) [b]
30a	4-Cl	exo-norborn-2-yl	7.20 ± 0.05	96 ± 1	235 ± 41	7.50 ± 0.14	68 ± 3
30b	4-Cl	R-(+)-born-2-yl	6.06 ± 0.12*	40 ± 5	45 ± 4	5.72 ± 0.10	-55 ± 12
30c	4-Cl	adamant-1-yl	6.38 ± 0.02*	70 ± 3	76 ± 2	5.82 ± 0.09	-24 ± 3
31a	4-CF$_3$	piperidin-1-yl	6.93 ± 0.13	96 ± 2	282 ± 6	7.34 ± 0.04	90 ± 1
31b	4-CF$_3$	exo-norborn-2-yl	6.58 ± 0.05	83 ± 6	145 ± 8	7.05 ± 0.05	25 ± 0
31c	4-CF$_3$	R-(+)-born-2-yl	6.38 ± 0.12*	45 ± 5	59 ± 7	6.13 ± 0.13	-23 ± 6
31d	4-CF$_3$	adamant-1-yl	7.04 ± 0.16*	49 ± 5	60 ± 11	6.78 ± 0.11	-27 ± 7
32a	4-OH	piperidin-1-yl	6.63 ± 0.10	99 ± 8	282 ± 48	6.94 ± 0.09	94 ± 5
32b	4-OH	exo-norborn-2-yl	6.01 ± 0.03	107 ± 2	301 ± 80	6.51 ± 0.13	80 ± 4
32c	4-OH	R-(+)-born-2-yl	5.26 ± 0.07*	46 ± 9	84 ± 3	- [c]	- [c]
32d	4-OH	adamant-1-yl	5.72 ± 0.05*	56 ± 2	133 ± 4	7.06 ± 0.15	21 ±2

Table 6-1 Binding affinity and efficacy of compounds designed based on modelling data at the CB2 receptor. *Data represent mean values ± SEM of three independent experiments. [a] Displacement of [³H]CP55940 in membrane homogenates of CHO cells transfected with human CB2 receptors over 10 concentration values; binding affinities (pK$_i$) were determined using experimental IC$_{50}$ values and the Cheng-Prusoff equation. [b] Measurement of enhancement of [³⁵S]GTPγS binding, assayed over 10 concentrations values. E$_{max}$ is expressed as a percentage of the maximum agonist-enhanced response, which was defined as the response elicited by 1μM CP55940 under identical conditions. [c] Not converged. * Apparent pKi; compounds displayed only partial displacement of [³H]CP55940.*

Compounds **30a**, **31a-b**, and **32a-b** were all able to displace [^{3}H]CP55940 completely (with the exception of **31b** which showed near-full (83%) displacement) in the competition binding assay and showed binding affinities (pK_i) of 7.20, 6.93, 6.58, 6.63, and 6.01 respectively. Compounds **30b-c**, **31c-d**, and **32c-d** were not able to displace [^{3}H]CP55940 completely even at high concentrations; their apparent binding affinities (pK_i) were 6.06, 6.38, 6.38, 7.04, 5.26, and 5.72 respectively. In the [^{35}S] GTPγS binding assay, compounds **30a**, **31a-b**, and **32a-b, d** all showed agonist activity with E_{max} values of 68%, 90%, 25%, 94%, 80%, and 21% respectively. Compounds **30b-c** and **31c-d** showed inverse agonist activity with E_{max} values of -55%, -24%, -23%, and -27% respectively. Only compound **32c** showed neutral antagonist activity.

The piperidinyl and norbornyl derivatives **30a**, **31a-b**, and **32a-b** all showed moderate to good CB2 receptor affinity in the nanomolar range. Affinity of the norbornyl derivatives were all slightly lower compared to their piperidinyl counterparts, while in both cases affinity decreased depending on the benzophenone 4-substituent in the order of Cl > CF$_3$ > OH, which was roughly in line with modelling data (predicted binding affinities were in the order of Cl > CF$_3$ = OH). This effect of the N-substituent could once again be attributed to steric factors, although the lack of N-N functionality in the norbornyl analogues affecting electronic distribution of the amide and hydrogen-bonding capacity cannot be ruled out. The effect of the benzophenone substitution on affinity was less clear; in general it seems that increasingly polar 4-substituents have a detrimental effect on binding. Functionally, the compounds **30a**, **31a**, and **32a-b** demonstrated a level of agonist activity significantly higher (% activation above basal of 235, 282, 282, and 301 respectively) than the compounds presented by Spencer *et al* (179). It was noteworthy that **31a** and **32a-b** were able to elicit a response comparable to that of the full agonist CP55940, an effect in line with our modelling predictions that ligand interaction, particularly hydrogen bonding, with polar residues such as T3.35 and S3.39 at the bottom of the binding pocket may play a role in the functional response of the CB2 receptor towards these derivatives.

Increasing hydrophobic bulk of the carboxamide N-substituent further had an intriguing effect on the pharmacology of these derivatives. The bornyl and adamantyl compounds **30b-c**, **31c-d**, and **32c-d** exhibited saturable but incomplete displacement of [³H]CP55940, indicating that these compounds were likely binding to a site distinct from the orthosteric site occupied by CP55940. As the Cheng-Prusoff equation assumes both the competing ligand and the radioligand bind exclusively to the same site, the apparent pK_i values of these compounds do not provide a true indication of their binding affinities. Figure 6-1 shows the predicted binding of CP55940 in relation to our previously predicted binding mode of fenofibrate amide derivatives. The functional activity of these compounds shifted in tandem with their binding, as **30b-c** and **31c-d** were clear inverse agonists while **32c-d** showed neutral antagonist and partial agonist characteristics respectively. This shift towards allosteric binding and functional activity with increasing hydrophobic bulk of the carboxamide substituent is illustrated in Figure 6-2 with compounds **31a-d** (see Appendix VI for figures of other compounds in this series).
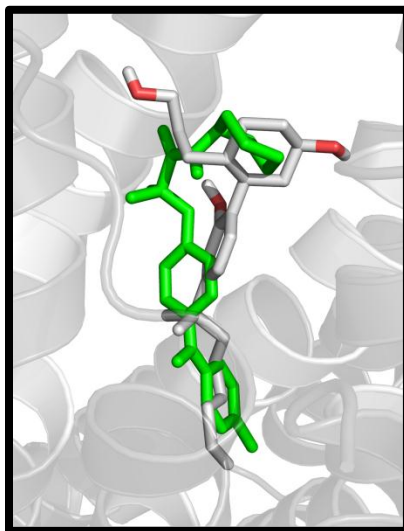
Figure 6-1 Predicted binding mode of CP55940 (grey) in reference to compound **24g** (green).
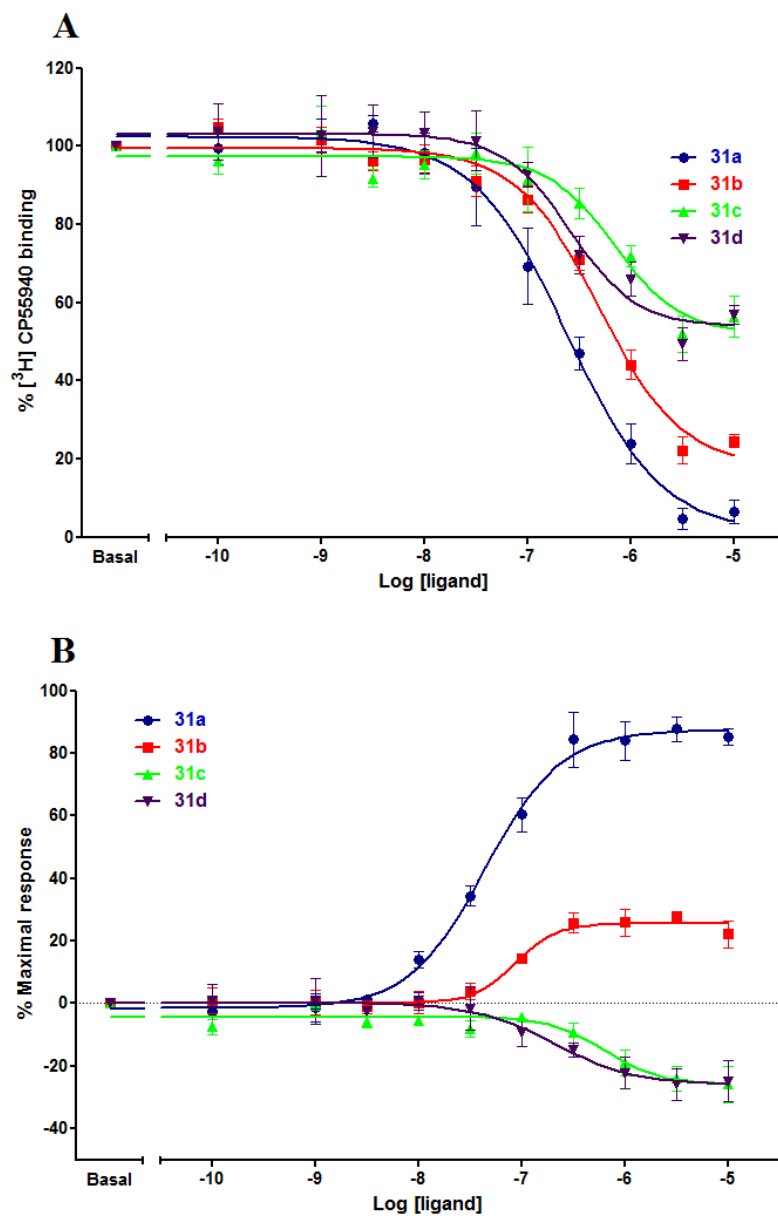
Figure 6-2 Pharmacology of several novel fenofibrate derivatives displaying a shift from orthosteric to allosteric binding. *(A) Displacement of [^{3}H]CP55940 from membrane homogenates of CHO cells expressing the human CB2 receptor. (B) Measurement of enhancement of [^{35}S]GTPγS binding in membrane homogenates of CHO cells expressing the CB2 receptor, expressed as a percentage of the response achieved by 1μM CP55940. The figures represent the means ± SEMs of three independent experiments.*

As our model had predicted that the bornyl and adamantyl derivatives were unable to adopt the same binding conformation as other fenofibrate derivatives, these findings lend credence to our modelling data, supporting the hypothesis that maintaining key hydrogen bonds with W5.43 and C7.42 as well as aromatic stacking interactions with F2.57, F3.36 and W6.48 appear crucial in stabilizing the binding of fenofibrate derivatives to the orthosteric site. Although hydrophobic cyclic carboxamide N-substituents were shown to be favourable in CB2 receptor binding, past a certain limit steric constraints appear to impair the ability of the ligand to maintain these key interactions, resulting in allosteric binding. The loss of this binding mode would also preclude interaction of the R_1 4-substituent with aforementioned polar residues such as T3.35 and S3.39 that may influence receptor activation, evidenced by the primarily inverse agonist nature of these allosteric binders. In the absence of more pharmacological data we can only speculate on the exact nature and location of this allosteric site, although the gradual shift in binding and activity with increasing hydrophobic bulk of the carboxamide substituent suggests a possible partial overlap with the orthosteric region. Such a manner of binding would be analogous to that of the CB1 allosteric modulator ORG27569 **42**, whose allosteric binding site in CB1 has recently been deduced to overlap partially with that of the orthosteric binder SR141716 (265). However, the development of these compounds together with additional investigations into their pharmacology is warranted before any concrete conclusions can be made.
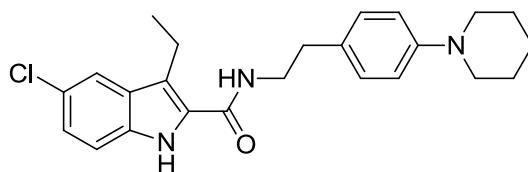
ORG27569 **42**

Figure 6-3 Structure of ORG27569

The fenofibrate derivatives **30a-32d** presented here represent a novel set of CB2 receptor ligands, ranging from orthosteric binders with high CB2 receptor affinity and agonist activity to allosteric binders with inverse agonist activity. The observed shift from orthosteric to allosteric binding with increasing cyclic hydrophobic bulk of the carboxamide N-substituent demonstrated here represents a unique and interesting structure-activity relationship not previously seen in fenofibrate derivatives binding to the CB2 receptor, and to the best of our knowledge, in other CB2 ligand series. The pharmacology of these derivatives also provides experimental evidence of our modelling predictions, demonstrating that the binding mode of fenofibrate derivatives to the CB2 receptor is indeed likely to be stabilized primarily by hydrogen bonds with W5.43 and C7.42 in addition to aromatic stacking with F2.57, F3.36 and W6.48. These findings also serve to validate our modelling protocols, demonstrating that the selection of a CB2 homology receptor model from a molecular dynamics-refined ensemble and its subsequent validation resulted in a model with significant predictive capability that can be used for the design of novel ligands. The model and binding mode predictions presented here may therefore serve as useful predictive tools in future CB2 receptor investigations, particularly in the design of novel fenofibrate amide derivatives as CB2 ligands.

7 CONCLUSIONS AND FUTURE WORK

7.1 Conclusions

7.1.1 Molecular modelling of the CB1 and CB2 receptors

We have presented here the construction of homology models of the human CB1 and CB2 cannabinoid receptors based on the crystal structure of the human adenosine A2A receptor. Molecular dynamics simulations of the receptors within a POPC bilayer have allowed us to refine both models and produce an ensemble of structures for model validation. While the CB2 receptor model remained stable throughout our simulations, the closure of the CB1 binding site was problematic and necessitated that we simulate the receptor with the known antagonist SR141716 bound.

Both simulations provided models that performed well in validation tests that included the binding affinity prediction of known ligands, virtual screening exercises, and the binding mode assessment of well-characterized ligands in conjunction with mutagenesis data. As expected the CB2 receptor model performed better in these validation tests particularly when considering agonist ligands, a likely consequence of our treatment of the CB1 receptor during MD simulations. Nevertheless, we have demonstrated that MD simulations remain a viable option in the refinement of cannabinoid receptor homology models. These cannabinoid receptor models represent potential tools in computational drug design applications beyond those presented here.

7.1.2   Structure-based design of novel fenofibrate derivatives as CB2 receptor ligands

The binding mode of fenofibrate amide derivatives with known cannabinoid receptor activity have been predicted here by the docking of these derivatives into both validated models. Predictions for the CB2 receptor were particularly robust following comparison with mutagenesis data, showing a binding mode stabilized by hydrogen-bonds with W5.43 and C7.42, aromatic stacking with F2.57, F3.36 and W6.48, and hydrophobic contacts with F2.64, V3.32 and I5.47. The contrasting presence of polar residues T3.35 and S3.39 at the bottom of the binding pocket was also of note, suggesting interaction with residues may impart functional activity. In light of these findings a series of compounds designed to test this binding hypothesis (**30a-32d**) were modelled and docked into our CB2 receptor model before being synthesized and pharmacologically evaluated.

The pharmacology of these newly designed derivatives provided evidence supporting our modelling predictions, allowed for the elucidation of further structure-activity relationships, and resulted in the discovery of novel allosteric CB2 receptor binders. With a gradual increase in hydrophobic bulk of the carboxamide N-substituent, the compounds demonstrated a shift from orthosteric to allosteric binding, validating our predicted binding mode as the compounds with highly hydrophobic (bornyl and adamantyl) carboxamide N-substituents were predicted to be unable to maintain the binding mode and key interactions, particularly hydrogen bonding with W5.43 and C7.42. These novel allosteric binders also showed primarily inverse agonist activity in contrast to the agonist orthosteric binders. Increasing the polarity and hydrogen bonding capacity of the R_1 4- substituent lowered CB2 binding affinity, but resulted in compounds with efficacies significantly higher than previously reported fenofibrate derivatives and comparable with that of the full agonist CP55940, supporting the hypothesis that the polar residues at the bottom of the binding pocket may influence receptor activation.

In conclusion, we have demonstrated here the successful use of a molecular dynamics-refined homology model of the human CB2 cannabinoid receptor in the structure-based design of novel ligands based on the fenofibrate scaffold. We have predicted the binding mode and the associated key interactions of this class of ligands, and validated these predictions by the prospective design of novel derivatives, which also provided further insight into the structure activity relationships governing their binding and efficacy. In addition, we have discovered several novel CB2 allosteric binders that demonstrate pharmacology distinct from other fenofibrate derivatives. These findings may be used to guide the design of further derivatives, and highlight the promise of the fenofibrate scaffold in developing novel CB2 receptor ligands.

7.2   Future Work

7.2.1   Molecular modelling of the CB1 and CB2 receptors

While the CB1 and CB2 cannabinoid receptor models constructed here have proven useful, there were inevitably several limitations to their predictive ability. In the context of our CB2 receptor model and fenofibrate derivatives, correlation between predicted and experimental binding affinities remained low due to the similarity between derivatives. This model can thus be used to predict the likelihood of a ligand maintaining key interactions and the relative binding affinity between derivatives, but in efforts to design increasingly potent ligands a higher degree of accuracy would be welcome. As the binding mode of these derivatives have been predicted with some confidence here, the application of other scoring functions or consensus scoring may provide the predictive ability desired, although the inherent limitations of current scoring functions have been highlighted earlier.

Our CB1 receptor model did not provide predictions that were highly supported by mutagenesis data, and in the absence of the equivalent CB1 pharmacological data for the novel

derivatives described here we make no claims on the accuracy of the predicted binding mode. However, the closing of the CB1 binding site during MD simulations, observed unwinding of the alpha helices, subsequent simulations with SR141716 bound, and positioning of certain key residues such W5.43 towards the lipid bilayer remain causes of concern. Efforts to resolve such issues may include MD simulations with different force fields such as the GROMOS 54a7, CHARMM and AMBER force fields (138,139,266). Studies on the dynamics of the receptor under such conditions using techniques such as principal component analysis may provide insight into our observations here and enhance the findings of previous studies into GPCR dynamics done by our group (267,268). Preliminary work in simulating the apo-CB1 receptor using the GROMOS 54a7 force field has shown that while this results in increased alpha helix stability as expected (the 54a7 set was parameterized to address this occurrence), the CB1 receptor binding site still closed during MD simulation. The final construction of a validated CB1 receptor model would provide an additional tool in the rational design of novel cannabinoid receptor ligands based on the fenofibrate scaffold, allowing for the prediction of properties such as CB2/CB1 receptor selectivity.

7.2.2   Chemistry and structure-based design of further novel ligands

Although the derivatives **30a-32d** have validated our binding mode predictions, the successful synthesis of the fenofibrate maleimide derivative **33** would represent the derivation of a novel scaffold for CB2 cannabinoid receptor ligand development. As it appears that the synthetic route employed in Scheme 2, specifically Friedel-Crafts reaction of the 3-phenylmaleimide **41** is unlikely to yield positive results, alternative synthetic routes would have to be employed. One possible scheme is shown below in Scheme 3, employing Weinreb ketone synthesis instead of a Friedel-Crafts reaction, although the stability of **43** in the titanium (IV) chloride/*n*-tributylamine system and the stability of Grignard reagent **46** would be a cause of concern.
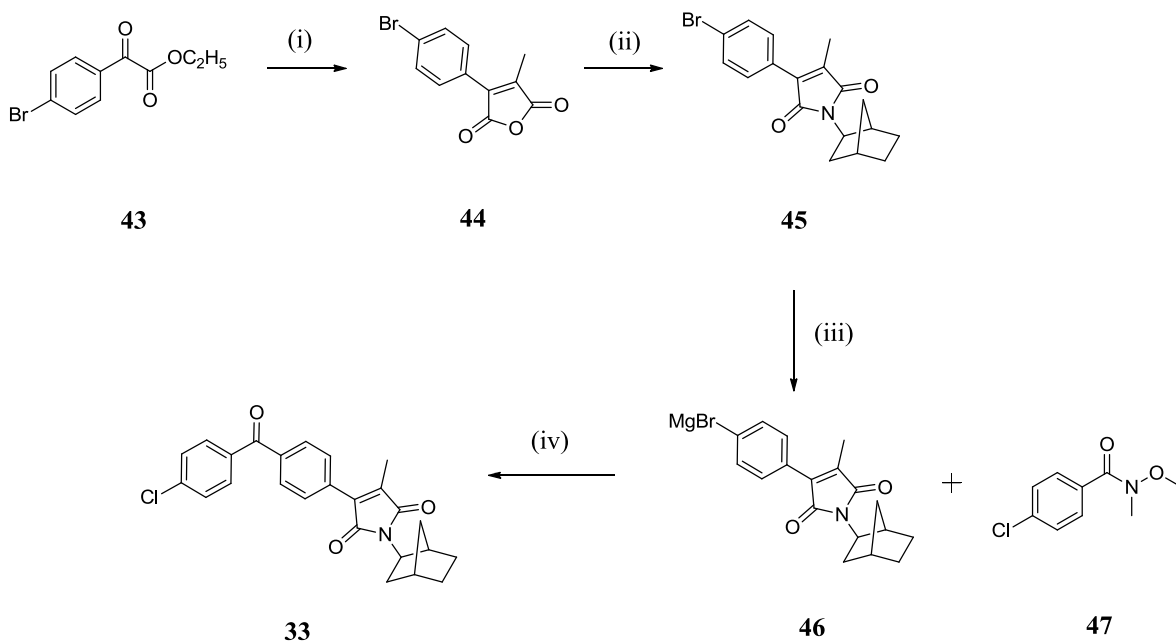
Scheme 3 Possible alternative synthesis of fenofibrate maleimide derivative **33.** Reagents and conditions: i) propionic anhydride, TiCl$_4$, *n*-Bu$_3$N, DCE, reflux, 12h; ii) *exo*-2-aminonorbornane, HMDS, ZnI$_2$, toluene, reflux, 3.5h; iii) Mg, Et$_2$O, reflux; iv) THF, 0°C.

The structure-activity relationships derived here also present the opportunity for the development of further derivatives based on the fenofibrate scaffold. Specifically, the introduction of other bulky heterocyclic substituents at the carboxamide such as piperazine, indole, and quinolone motifs combined with polar substituents at the R$_1$ 4-position may represent potential potent CB2 agonists. These derivatives could be docked into our CB2 model in order to ease the selection process. Simultaneously, the synthesis of further adamantyl, bornyl and equivalent derivatives as allosteric binders would allow for more detailed investigations into their structure-activity relationships, ideally culminating in the identification of their allosteric binding site and an equivalent binding mode prediction based on the same consensus approach applied here.
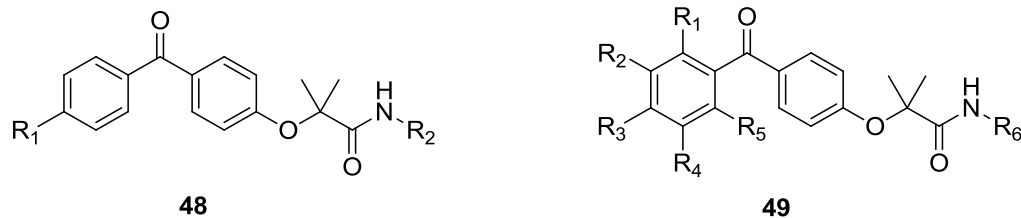
R₁ = OMe, NH₂, CH₂OH, CH₂SH, COCH₃   R₁-R₅ = F, Cl, Me, OH,CF₃, OMe, H
R₂ = piperazinyl, indoyl, quinolinyl, isoquinolinyl   R₆ = adamantyl, bornyl, isobornyl, camphoryl

Figure 7-1 Potential CB2 cannabinoid receptor ligands based on the fenofibrate scaffold investigating orthosteric (**48**) and allosteric (**49**) structure-activity relationships.

7.2.2   Pharmacology

In the context of the novel CB2 receptor ligands described here, the pharmacology of the orthosteric and allosteric binders described here may both be subject to further investigations. While the predicted binding mode of the orthosteric binders already possesses strong support from the pharmacological data available, short of crystallographic data, site-directed mutagenesis studies involving the key residues implicated in their binding such as W5.43, C7.42, F3.36 and W6.48 would provide unequivocal proof of their binding mode. In the same manner mutagenesis studies would be beneficial in the investigation of the allosteric binders by alluding to their possible binding site, although more thorough investigations are warranted as the literature regarding CB2 allosteric binding is by far less extensive. A more pertinent line of inquiry would be to describe the allosteric modulation properties of these derivatives on the binding of orthosteric ligands, if any, through assays such as binding kinetics assays.

In a typical dissociation kinetic assay the dissociation rate of a radioligand (e.g. [^{3}H]CP55940) is measured by first allowing the radiolabelled ligand to achieve equilibrium with the receptor, and then initiating dissociation by either diluting the sample or adding an excess of

unlabelled competing compound. The specific binding of the radioligand is then measured at several time points following this, allowing the dissociation pattern of the radioligand to be plotted and dissociation rate constants to be calculated (269). In the presence of allosteric modulators, this dissociation rate is altered, with positive allosteric modulators decreasing the dissociation rate and negative allosteric modulators increasing the dissociation rate of the radioligand. Conducting assays such as this would provide definite evidence of any potential modulatory properties of the allosteric compounds described here.

CB1 pharmacological data (particularly CB1 receptor binding affinity data) of the novel derivatives designed based on our modelling data in addition to those previously described by Spencer *et al* (179) would provide additional experimental input into our modelling predictions and allow us to establish more concrete structure-activity relationships than those currently available. Such data would be highly valuable in achieving our final goal of constructing validated models of both cannabinoid receptors for structure-based drug design.

8   EXPERIMENTAL

8.1   Molecular modelling

All calculations were performed on a Linux cluster consisting of 72 Intel Xeon 3.12 GHz processors. Energy minimizations and molecular dynamics simulations were conducted using the GROMACS software suite with the GROMOS 53a6 united-atom force field, supplemented with additional lipid parameters (140,270). Full periodic boundary conditions were applied. The simple point charge (SPC) water model was used (271). The maximum force tolerance for energy minimization was set at 10kJ/mol/nm. The time step used was 2fs. Cut-offs for short-range electrostatic and van der Waals (vdW) interactions were set at 14Å at 10Å respectively. Long range electrostatic interactions were treated using the Particle Mesh Ewald method (272,273). The neighbour list cut-off was set at 10Å and updated every 5 steps. All bonds lengths were constrained using LINCS, while SETTLE was used to constrain the geometry of water molecules (274,275). Temperature coupling at 310K was achieved using velocity rescaling, with a coupling constant of τ = 0.5ps (276). Semi-isotropic pressure coupling at 1 bar was achieved using the Parinello-Rahman barostat, with a coupling constant of τ = 5.0ps (277).

All docking was conducted using AUTODOCK 4.2 with a Lamarckian genetic algorithm (278,279). Ligands were initially constructed and subsequently energy minimized using ChemBioDraw Ultra 12.0 (280). The ligands and protein structures were then assigned Gasteiger charges and prepared for docking using AutoDock Tools (279). All torsions in ligands were assigned as flexible, while the receptor itself was kept rigid. 100 runs were conducted for each ligand. Population size was set at 300 for each run, while maximum number of evaluations was set at 2,500,000, and maximum number of generations set at 27,000. Grid spacing of 0.2Å was used. Cluster analysis was done using an RMSD tolerance of 1.0Å. Predicted pK_i values were extracted for the conformations with the lowest binding energies.

8.2   General chemistry

All chemicals and solvents were bought from standard suppliers and were used without further purification. Anhydrous solvents were prepared using 3Å molecular sieves (3-4 mesh, Sigma Aldrich) according to the method presented by Williams *et al* (281).

All reactions were conducted under ambient temperatures unless otherwise stated. Reactions monitored using thin layer chromatography were done using commercially available pre-coated aluminium backed plates from Merck (Merck TLC Silica Gel 60 F254, Product No HX273866), with visualization under standard UV wavelengths (254 and 366nm). All purifications using centrifugal radial TLC were conducted using a Harrison 7924T Chromatotron, with the sorbent layer prepared using Merck Silica Gel 60 PF254 containing gypsum (Product No TA1762549). Column chromatography was performed using Merck silica gel 60, 230-400 mesh (Product No TA1686285). All microwave reactions were carried out using either a Sharp R-658L(S) 800W Microwave Oven or a CEM Discover Series Microwave Reactor. All compounds were identified and characterized using a combination of NMR, HRMS, and FTIR. All melting points were recorded using a Stuart SMP10 Melting Point Apparatus and are uncorrected. Melting points for compounds were compared using data obtained from the ChemSpider database where available (282). FT-IR spectra were recorded using a Perkin Elmer Spectrum RX1 FTIR Spectrophotometer as KBr discs or thin films, with a range of 4000-400cm^{-1}. ^{1}H and ^{13}C NMR spectra were recorded in appropriate deuterated solvents using a Bruker 400 or 600 MHz spectrometer. Chemical shifts are reported relative to an internal reference of tetramethylsilane at 0.00ppm. Positive electrospray ionization (ESI) high resolution mass spectroscopy was obtained using a JMS-T100LP DART-TOF mass spectrometer. The final compounds were determined to be of at least 95% purity through analytical HPLC, using a Perkin Elmer Series 200 HPLC system with a 4.6 x 250mm Agilent Zobrax 300SB-C18 column.

All organic extracts following aqueous work-up were dried using either anhydrous Na_2SO_4 or anhydrous $MgSO_4$, filtered via gravity or vacuum filtration, and the solvent removed under reduced pressure with temperatures less than 40°C using a rotary evaporator.

8.2.1 General methods

Unless otherwise stated, all reactions were carried out using the following General Methods:

General Method A: Adapted from reference (179). To anhydrous $AlCl_3$ (1.1eq) under a N_2 atmosphere, 20mL of anhydrous DCM was added. Anisole (1.0 eq) was then added, and the reaction mixture cooled to 0°C in an ice bath. The selected benzoyl chloride (1.0 eq) was then added dropwise. The reaction mixture was kept at 0°C for 30 minutes before being slowly brought to room temperature and stirred overnight. The reaction mixture was then quenched using a 20mL mixture of ice and 2M HCl, and the aqueous layer extracted using DCM. The combined organic layers were then washed with water (twice) and brine, before being dried over anhydrous Na_2SO_4 and the solvent removed under vacuum.

General Method B: Adapted from reference (258). (1) For reactions conducted using a standard microwave oven: A mixture of the selected 4-methoxybenzophenone (1.0eq) and pyridine hydrochloride (5.0eq) were mixed in either a stoppered round bottom flask and irradiated at 240W for 16 minutes in 2 minute intervals, with the flask being cooled to room temperature in between cycles. (2) For reactions conducted using a microwave reactor: A mixture of the selected 4-methoxybenzophenone (1.0eq) and pyridine hydrochloride (5.0eq) were mixed in a microwave vial and irradiated at variable power and 200°C for 16 minutes.

The reaction mixture was then quenched using 20mL of ice water, and extracted with ethyl acetate. The organic layer was then washed with brine, dried over anhydrous Na_2SO_4, and the solvent removed under vacuum.

General Method C: Adapted from reference (260). To a mixture of the selected di-substituted benzophenone (1.0eq) and triphenylphosphine (1.2eq) under a N_2 atmosphere, 5mL of anhydrous MeCN was added and the reaction mixture refluxed. A solution of methyl-2-hydroxyisobutyrate (1.2eq) and DIAD (1.2eq) in anhydrous MeCN was then added slowly over a period of 3-4 hours. The reaction mixture was then refluxed for a further 7-14 hours. The solvent was removed under vacuum, and the remaining residue was purified without further work up.

General Method D: Adapted from reference (179). The methyl ester (1.0 eq) of the fenofibric acid derivative was dissolved in a mixture of THF and water (1:1). Sodium hydroxide (5.0 eq) was then added, and the reaction mixture stirred under a N_2 atmosphere until the complete disappearance of the ester as monitored via TLC. The THF was then evaporated, and the remaining aqueous solution was diluted with water. The solution was then acidified to pH 1 using concentrated HCl, and the resulting precipitate extracted using chloroform. The combined organic layers were then dried over anhydrous Na_2SO_4, filtered, and the solvent removed under vacuum.

General Method E: Adapted from reference (283). The fenofibric acid derivative (1.0eq) was dissolved in anhydrous DCM, and triethylamine (1.2eq), HBTU (1.2eq) and the selected amine (1.2eq) was then added, with the reaction mixture then stirred for between 4 hours to overnight. The reaction mixture was then diluted with DCM, washed with 1M HCl, water and brine. The organic layer was then dried over anhydrous Na_2SO_4, filtered, and the solvent removed under vacuum.

8.2.2 Compound characterization

(4-Chlorophenyl)(4-methoxyphenyl)methanone (35a)
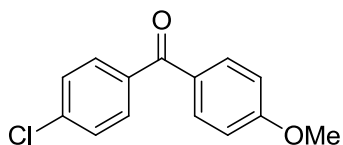
According to General Method A, 4-chlorobenzoyl chloride (1.41ml, 11.00mmol) was reacted with anisole (1.20ml, 11.04mmol) and $AlCl_3$ (1.600g, 12.00mmol) in DCM (20mL) for 24 hours to afford **35a**.

Yield: 67%

Appearance: White solid

Purification: Recrystallized from EtOAc/hexane

Melting Point: 123-124°C. Reported 123-125°C.

m/z (ESI+) [MH]+: Calculated 247.0526, found 247.0518

1H NMR (400 MHz, CDCl3): δ 7.80 (d, J = 8.8 Hz, 2H), 7.71 (d, J = 8.4 Hz, 2H), 7.46 (d, J = 8.4 Hz, 2H), 6.97 (d, J = 8.8 Hz, 2H), 3.90 (s, 3H)

FTIR (KBr): cm^{-1} 1639 (conj. ketone C=O); 1605, 1482 (aromatic C-C); 1255 (ether C-O); 760 (C-Cl)

(4-Methoxyphenyl)(4-(trifluoromethyl)phenyl)methanone (35b)

According to General Method A, 4-trifluoromethylbenzoyl chloride (0.50ml, 3.37mmol) was reacted with anisole (0.40ml, 3.7mmol) and $AlCl_3$ (0.495g, 3.7mmol) in DCM (20ml) for 24 hours to afford **35b**.

Yield: 83%

Appearance: White solid
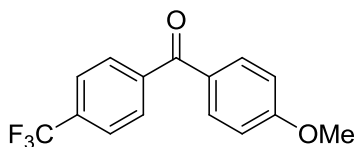
Purification: Recrystallized from EtOAc/hexane

Melting Point: 118-119°C

m/z (ESI+) [MH]$^+$: Calculated 281.0789, found 281.0794

^{1}H NMR (400 MHz, CDCl$_3$): δ 7.87 – 7.80 (m, 4H), 7.75 (d, J = 8.1 Hz, 2H), 6.99 (d, J = 8.9 Hz, 2H), 3.91 (s, 3H)

FTIR (KBr): cm^{-1} 1677 (conj. ketone C=O); 1601, 1411 (aromatic C-C); 1328 (ether C-O); 1138 (C-F)

(4-Chlorophenyl)(4-hydroxyphenyl)methanone (36a)
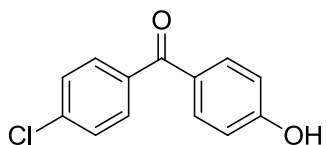
According to General Method B, **35a** (0.600g, 2.43mmol) and pyridine.HCl (1.427g, 12.40mmol) were irradiated in a standard microwave oven at 240W for 16 minutes to afford **36a**.

Yield: 71%

Appearance: White solid

Purification: Radial thin-layer chromatography. EtOAc/ hexane (1:19) to pure EtOAc

Melting Point: 178-180°C. Reported 177-182°C.

m/z (ESI+) [MH]$^+$: Calculated 233.0369, found 233.0371

^{1}H NMR (400 MHz, CDCl$_3$): δ 7.73 – 7.69 (m, 4H), 7.45 (d, J = 8.3 Hz, 2H), 6.89 (d, J = 8.6 Hz, 2H)

FT-IR (KBr): cm^{-1} 3337 (phenolic OH); 1645 (conj. ketone C=O); 1598, 1570 (aromatic C-C); 1313 (phenolic C-O); 836 (C-Cl)

(4-Hydroxyphenyl)(4-(trifluoromethyl)phenyl)methanone (36b)

According to General Method B, **35b** (0.824g, 2.84mmol) and pyridine.HCl (1.427g, 14.72mmol) were irradiated with in a microwave reactor at variable power and 200°C for 16 minutes to afford **36b**.

Yield: 67%

Appearance: White solid

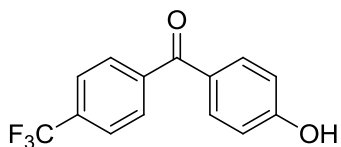**Purification:** Radial thin-layer chromatography, EtOAc/ hexane (1:19) to pure EtOAc

Melting Point: 145-146°C

m/z (ESI+) [MH]$^+$: Calculated 267.0633, found 267.0633

^{1}H NMR (400 MHz, CDCl$_3$): δ 7.84 (d, J = 8.3Hz, 2H), 7.80-7.74 (m, 4H), 6.93 (d, J = 8.8 Hz, 2H)

FT-IR (KBr): cm^{-1} 3326 (phenolic OH); 1643 (conj. ketone C=O); 1601 (aromatic C-C); 1315 (phenolic C-O); 1149 (C-F)

Methyl 2-(4-(4-chlorobenzoyl)phenoxy)-2-methylpropanoate (37a)
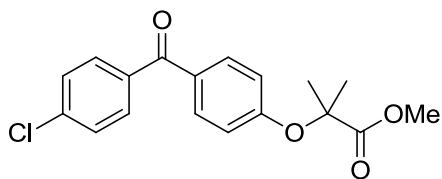
According to General Method C, **36a** (0.463g, 1.99 mmol) was reacted with methyl-2-hydroxyisobutyrate (0.280ml, 2.40mmol), PPh$_3$ (0.632g, 2.41mmol) and DIAD (0.470ml, 2.40mmol) in MeCN (5ml) for 15 hours to afford **37a**.

Yield: 52%

Appearance: Light yellow solid

Purification: Radial thin-layer chromatography, EtOAc/hexane (1:99) to pure EtOAc

Melting Point: 75-79°C

m/z (ESI+) [MH]+: Calculated 333.0888, found 333.0883

^{1}H NMR (400 MHz, CDCl$_3$): δ 7.74 (d, J = 8.5 Hz, 2H), 7.71 (d, J = 8.3 Hz, 2H), 7.45 (d, J = 8.3 Hz, 2H), 6.85 (d, J = 8.5 Hz, 2H), 3.78 (s, 3H), 1.68 (s, 6H)

FT-IR (KBr): cm^{-1} 1750 (ester C=O); 1652 (conj. ketone C=O); 1600 (aromatic C-C); 1148 (C-O); 763 (C-Cl)

Methyl 2-methyl-2-(4-(4-(trifluoromethyl)benzoyl)phenoxy)propanoate (37b)
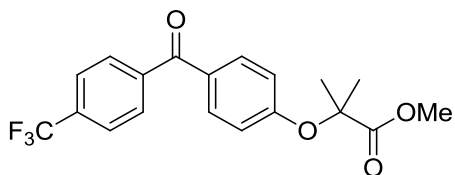
According to General Method C, **36b** (0.492g, 1.85 mmol) was reacted with methyl-2-hydroxyisobutyrate (0.28ml, 2.43mmol), PPh$_3$ (0.634g, 2.42mmol) and DIAD (0.48ml, 2.42mmol) in MeCN (5ml) for 15 hours 45 minutes to afford **37b**.

Yield: 69%

Appearance: Light yellow solid

Purification: Radial thin-layer chromatography, EtOAc/hexane (1:99) to pure EtOAc

Melting Point: 80-82°C

m/z (ESI+) [MH]+: Calculated 367.1157, found 367.1154

^{1}H NMR (400 MHz, CDCl$_3$): δ 7.84 (d, J = 8.0 Hz, 2H), 7.79 – 7.72 (m, 4H), 6.86 (d, J = 9.0 Hz, 2H), 3.78 (s, 3H), 1.68 (s, 6H)

FT-IR (KBr): cm^{-1} 1741 (ester C=O); 1661 (conj. ketone C=O); 1598 (aromatic C-C); 1318 (C-O); 1173, 1144 (C-F)

Methyl 2-(4-(4-hydroxybenzoyl)phenoxy)-2-methylpropanoate (37c)
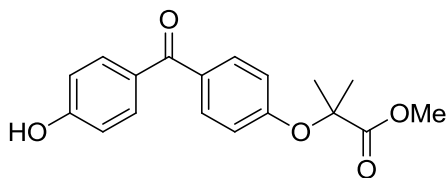
According to General Method C, 4,4'-dihydroxybenzophenone (0.501g, 2.33 mmol) was reacted with methyl-2-hydroxyisobutyrate (0.32ml, 2.80mmol), PPh$_3$ (0.733g, 2.79mmol) and DIAD (0.55ml, 2.79mmol) in MeCN (5ml) for 15 hours to afford **37c**.

Yield: 32%

Appearance: Light yellow solid

Purification: Column chromatography. EtOAc/hexane (3:7)

Melting Point: 108-115°C

m/z (ESI+) [MH]$^+$: Calculated 315.1232, found 315.1223

^{1}H NMR (400 MHz, CDCl$_3$): δ 7.77 – 7.69 (m, 4H), 6.91 (d, J = 8.7 Hz, 2H), 6.85 (d, J = 7.9 Hz, 2H), 3.78 (s, 3H), 1.67 (s, 6H)

FT-IR (KBr): cm^{-1} 3250 (phenolic OH); 1735 (ester C=O); 1621 (conj. ketone C=O); 1602, 1586 (aromatic C-C); 1286, 1252 (C-O)

Fenofibric acid/ 2-(4-(4-chlorobenzoyl)phenoxy)-2-methylpropanoic acid (22)
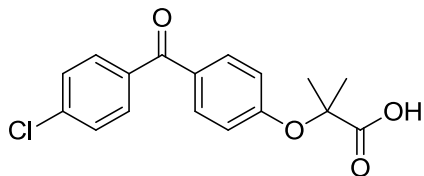
According to General Method D, **37a** (0.310g, 0.93mmol) was reacted with NaOH (0.224g, 5.60mmol) in THF/water 1:1 (10ml) for 8 hours to afford **22**.

Yield: 92%

Appearance: White solid

Purification: No purification needed

Melting Point: 174-175°C. Reported 177-179°C.

m/z (ESI+) [MH]$^+$: Calculated 319.0737, found 319.0722

^{1}H NMR (400 MHz, CDCl$_3$): δ 7.75 (d, J = 8.9 Hz, 2H), 7.71 (d, J = 8.6 Hz, 2H), 7.45 (d, J = 8.6 Hz, 2H), 6.95 (d, J = 8.9 Hz, 2H), 1.70 (s, 6H)

FT-IR (KBr): cm^{-1} 2952 (carboxylic acid OH); 1744 (carboxylic acid C=O); 1633 (conj. ketone C=O); 1599 (aromatic C-C); 1263 (C-O); 1150, 769 (C-Cl)

2-Methyl-2-(4-(4-(trifluoromethyl)benzoyl)phenoxy)propanoic acid (38a)
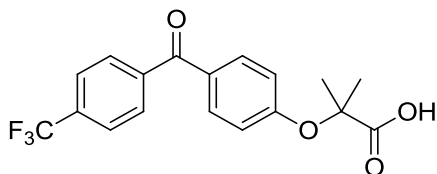
According to General Method D, **37b** (0.336g, 0.92mmol) was reacted with NaOH (0.198g, 4.95mmol) in THF/water 1:1 (10ml) for 6 hours to afford **38a**.

Yield: 96%

Appearance: White solid

Purification: No purification needed

Melting Point: 139-141°C

m/z (ESI+) [MH]$^+$: Calculated 353.1000, found 353.0979

^{1}H NMR (400 MHz, CDCl$_3$): δ 7.84 (d, J = 8.1 Hz, 2H), 7.79 – 7.72 (m, 4H), 6.95 (d, J = 7.3 Hz, 2H), 1.69 (s, 6H)

FT-IR (KBr): cm^{-1} 3046 (carboxylic acid OH); 1747 (carboxylic acid C=O); 1637 (conj. ketone C=O); 1599 (aromatic C-C); 1324 (C-O), 1155, 1129 (C-F)

2-(4-(4-Hydroxybenzoyl)phenoxy)-2-methylpropanoic acid (38b)
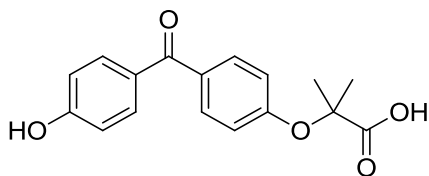
According to General Method D, **37c** (0.216g, 0.69mmol) was reacted with NaOH (0.192g, 4.80mmol) in THF/water 1:1 (8ml) for 24 hours to afford **38b**.

Yield: 91%

Appearance: White solid

Purification: Acid-base extraction

Melting Point: 176-180°C

m/z (ESI+) [MH]$^+$: Calculated 301.1076, found 301.1076

^{1}H NMR (400 MHz, CDCl$_3$): δ 7.71 (d, *J* = 8.9 Hz, 4H), 6.93 (d, *J* = 8.9 Hz, 2H), 6.88 (d, *J* = 8.8 Hz, 2H), 1.68 (s, 6H)

FT-IR (KBr): cm^{-1} 3324 (carboxylic acid OH); 1702 (carboxylic acid C=O); 1604 (conj. ketone C=O); 1583 (aromatic C-C); 1329, 1288 (C-O)

N-(*exo*-Norborn-2-yl)-2-(4-(4-chlorobenzoyl)phenoxy)-2-methylpropanamide (30a)
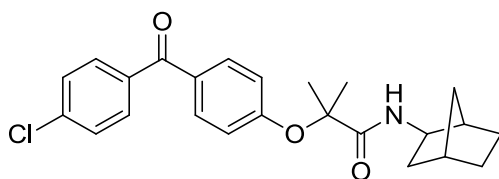
According to General Method E, fenofibric acid (0.075g, 0.24mmol) was reacted with exo-2-aminonorbornane (0.031ml, 0.26mmol), HBTU (0.098g, 0.26mmol), and Et$_3$N (0.036ml, 0.26mmol) in DCM (5ml) for 4 hours to afford **30a**.

Yield: 88%

Appearance: White solid

**Purification:** Radial thin-layer chromatography. EtOAc/hexane (1:9) to EtOAc/hexane (1:1)

Melting Point: 140-141°C

m/z (ESI+) [MH]$^+$: Calculated 412.1679, found 412.1682

^{1}H NMR (400 MHz, CDCl$_3$): δ 7.74 (dd, J = 13.9, 8.8 Hz, 4H), 7.47 (d, J = 8.7 Hz, 2H), 6.96 (d, J = 8.7 Hz, 2H), 6.23 (d, J = 6.7 Hz, 1H), 3.74 (td, J = 7.4, 3.6 Hz, 1H), 2.21 (d, J = 20.1 Hz, 2H), 1.79 (dd, J = 13.6, 8.6 Hz, 1H), 1.59 (d, J = 2.4 Hz, 6H), 1.56 – 1.40 (m, 2H), 1.30 – 1.22 (m, 1H), 1.17 – 1.07 (m, 4H)

^{13}C NMR (100 MHz, CDCl$_3$): δ 194.34, 173.03, 158.68, 138.70, 136.21, 131.95, 131.47, 131.30, 128.70, 119.37, 81.92, 52.81, 42.20, 40.18, 35.71, 35.57, 28.16, 26.45, 25.60, 25.06

FT-IR (KBr): cm^{-1} 3352 (amide NH); 1660 (amide C=O); 1637 (conj. ketone C=O); 1601 (aromatic C-C) 1248 (C-O); 1147, 763 (C-Cl)

N-(R-(+)-Born-2-yl)-2-(4-(4-chlorobenzoyl)phenoxy)-2-methylpropanamide (30b)

According to General Method E, fenofibric acid (0.070g, 0.22mmol) was reacted with R(+)-bornylamine (0.044g, 0.29mmol), HBTU (0.102g, 0.27mmol), and Et$_3$N (0.037ml, 0.26mmol) for 22 hours 45 minutes in DCM (5ml) to afford **30b**.

Yield: 91%

Appearance: White solid

Purification: Radial thin-layer chromatography. EtOAc/hexane (1:9) to EtOAc/hexane (1:1)

Melting Point: 119-121°C

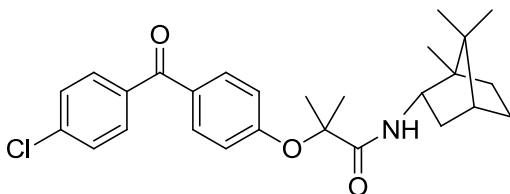**m/z (ESI+) [MH]$^+$:** Calculated 454.2149, found 454.2113

^{1}H NMR (400 MHz, CDCl$_3$): δ 7.76 (d, J = 8.7 Hz, 2H), 7.72 (d, J = 8.5 Hz, 2H), 7.46 (d, J = 8.5 Hz, 2H), 6.99 (d, J = 8.7 Hz, 2H), 6.43 (d, J = 8.8 Hz, 1H), 4.28 – 4.20 (m, 1H), 2.39 – 2.28 (m,

1H), 1.76 – 1.66 (m, 1H), 1.66 – 1.64 (m, 1H), 1.62 (d, J = 7.0 Hz, 6H), 1.37 – 1.17 (m, 2H), 1.09 – 1.02 (m, 1H), 0.95 (s, 3H), 0.85 (s, 3H), 0.78 (s, 3H), 0.70 (dd, J = 13.2, 4.5 Hz, 1H)

^{13}C NMR (100 MHz, CDCl$_3$): δ 194.30, 173.90, 158.72, 138.70, 136.23, 131.98, 131.45, 131.29, 128.69, 119.27, 82.12, 53.83, 49.57, 48.27, 44.89, 37.55, 28.36, 27.93, 25.64, 25.36, 19.82, 18.69, 13.85

FT-IR (KBr): cm^{-1} 3357 (amide NH); 1666 (amide C=O); 1651 (conj. ketone C=O); 1604 (aromatic C-C); 1247 (C-O); 1150, 764 (C-Cl)

N-(Adamantan-1-yl)-2-(4-(4-chlorobenzoyl)phenoxy)-2-methylpropanamide (30c)

According to General Method E, fenofibric acid (0.060g, 0.19mmol) was reacted with 1-adamantylamine (0.034g, 0.23mmol), HBTU (0.085g, 0.23mmol), and Et$_3$N (0.032ml, 0.23mmol) for 24 hours in DCM (5ml) to afford **30c**.

Yield: 92%

Appearance: White crystals

Purification: Recrystallized from EtOAc/CHCl$_3$

Melting Point: 167-169°C

m/z (ESI+) [MH]$^+$: Calculated 452.1992, found 452.1977

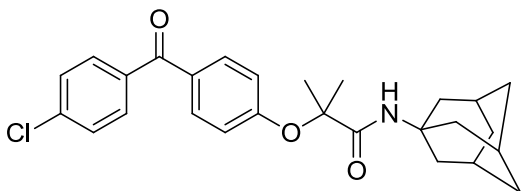**^{1}H NMR (400 MHz, CDCl$_3$):** δ 7.76 (d, J = 8.6 Hz, 2H), 7.73 (d, J = 8.3 Hz, 2H), 7.46 (d, J = 8.3 Hz, 2H), 6.97 (d, J = 8.6 Hz, 2H), 6.08 (s, 1H), 2.07 (br s, 3H), 1.96 (br s, 6H), 1.66 (br s, 6H), 1.57 (br s, 6H)

^{13}C NMR (100 MHz, CDCl$_3$): δ 194.38, 172.92, 158.81, 138.66, 136.26, 131.95, 131.31, 128.69, 119.13, 82.00, 51.84, 41.38, 36.33, 29.43, 25.27

FT-IR (KBr): cm⁻¹ 3346 (amide NH); 1665 (amide C=O); 1652 (conj. ketone C=O); 1604 (aromatic C-C); 1246 (C-O); 1151, 765 (C-Cl)

N-(Piperidin-1-yl)-2-(4-(4-(trifluoromethyl)benzoyl)phenoxy)-2-methylpropanamide (31a)
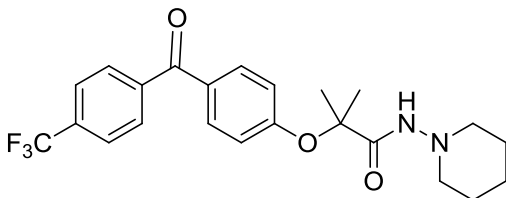
According to General Method E, **38a** (0.058g, 0.16mmol) was reacted with 1-aminopiperidine (0.028ml, 0.20mmol), HBTU (0.078g, 0.21mmol), and Et₃N (0.028ml, 0.20mmol) for 24 hours in DCM (5ml) to afford **31a**.

Yield: 91%

Appearance: White solid

Purification: Radial thin-layer chromatography. EtOAc/hexane (1:9) to pure EtOAc

Melting Point: 154-156°C

m/z (ESI+) [MH]⁺: Calculated 435.1895, found 435.1895

¹H NMR (400 MHz, CDCl₃): δ 7.85 (d, *J* = 8.1 Hz, 2H), 7.78 (d, *J* = 8.9 Hz, 2H), 7.76 (d, *J* = 8.1 Hz, 2H), 7.10 (br s, 1H), 7.00 (d, *J* = 8.9 Hz, 2H), 2.71 − 2.68 (m, 4H), 1.70 (p, *J* = 5.6 Hz, 4H), 1.63 (s, 6H), 1.44 − 1.34 (m, 2H)

¹³C NMR (100 MHz, CDCl₃): δ 194.30, 170.71, 158.91, 132.16, 129.94, 125.41, 119.21, 81.72, 56.84, 25.41, 25.31, 23.24

FT-IR (KBr): cm⁻¹ 3307 (amide NH); 1677 (amide C=O); 1648 (conj. ketone C=O); 1600 (aromatic C-C); 1313 (C-O); 1171, 1146 (CF₃)

N-(*exo*-norborn-2-yl)-2-methyl-2-(4-(4-(trifluoromethyl)benzoyl)phenoxy)propanamide (31b)
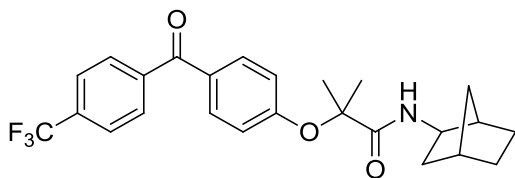
According to General Method E, **38a** (0.061g, 0.17mmol) was reacted with exo-2-aminonorbornane (0.024ml, 0.20mmol), HBTU (0.078g, 0.21mmol), and Et$_3$N (0.028ml, 0.20mmol) for 24 hours in DCM (5ml) to afford **31b**.

Yield: 88%

Appearance: White solid

Purification: Radial thin-layer chromatography. EtOAc/hexane (1:9) to EtOAc/hexane (1:1)

Melting Point: 103-106°C

m/z (ESI+) [MH]$^+$: Calculated 446.1943, found 446.1939

^{1}H NMR (400 MHz, CDCl$_3$): δ 7.85 (d, *J* = 8.1 Hz, 2H), 7.78 (d, *J* = 8.9 Hz, 2H), 7.76 (d, *J* = 8.1 Hz, 2H), 6.97 (d, *J* = 8.9 Hz, 2H), 6.21 (d, *J* = 7.6 Hz, 1H), 3.74 (td, *J* = 7.6, 3.5 Hz, 1H), 2.25 – 2.16 (m, 2H), 1.79 (ddd, *J* = 13.1, 8.0, 1.9 Hz, 1H), 1.60 (d, *J* = 2.4 Hz, 6H), 1.56 – 1.39 (m, 2H), 1.30 – 1.21 (m, 1H), 1.17 – 1.06 (m, 4H)

^{13}C NMR (100 MHz, CDCl$_3$): δ 194.33, 172.92, 159.07, 132.14, 129.95, 125.44, 119.36, 81.98, 52.83, 42.19, 40.18, 35.71, 35.57, 28.16, 26.44, 25.61, 25.06

FT-IR (KBr): cm^{-1} 3366 (amide NH); 1659 (amide C=O); 1643 (conj. ketone C=O); 1602 (aromatic C-C); 1248 (C-O); 1181, 1148 (CF$_3$)

N-(R-(+)-Born-2-yl)-2-(4-(4-(trifluoromethyl)benzoyl)phenoxy)-2-methylpropanamide (31c)
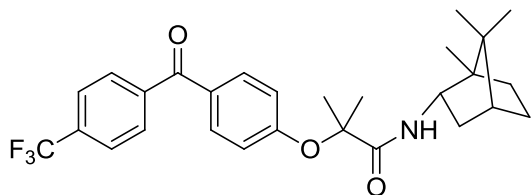
According to General Method E, **38a** (0.050g, 0.14mmol) was reacted with *R*(+)-bornylamine (0.026g, 0.17mmol), HBTU (0.065g, 0.17mmol), and Et$_3$N (0.024ml, 0.17mmol) for 23 hours in DCM (5ml) to afford **31c**.

Yield: 93%

Appearance: White solid

Purification: Radial thin-layer chromatography. EtOAc/hexane (1:9) to EtOAc/hexane (1:1)

Melting Point: 81-82°C

m/z (ESI+) [MH]$^+$: Calculated 488.2412, found 488.2406

^{1}H NMR (400 MHz, CDCl$_3$): δ 7.85 (d, *J* = 8.1 Hz, 2H), 7.79 (d, *J* = 8.9 Hz, 2H), 7.76 (d, *J* = 8.1 Hz, 2H), 7.01 (d, *J* = 8.9 Hz, 2H), 6.41 (d, *J* = 9.1 Hz, 1H), 4.30 – 4.17 (m, 1H), 2.39 – 2.28 (m, 1H), 1.78 – 1.67 (m, 2H), 1.63 (d, *J* = 7.2 Hz, 6H), 1.34 – 1.17 (m, 2H), 1.10 – 1.01 (m, 1H), 0.95 (s, 3H), 0.85 (s, 3H), 0.78 (s, 3H), 0.70 (dd, *J* = 13.4, 4.5 Hz, 1H)

^{13}C NMR (100 MHz, CDCl$_3$): δ 194.32, 173.81, 159.10, 132.18, 129.96, 125.41, 119.27, 82.18, 53.84, 49.57, 48.28, 44.88, 37.56, 28.37, 27.92, 25.65, 25.36, 19.81, 18.69, 13.85

FT-IR (KBr): cm^{-1} 3370 (amide NH); 1667 (amide C=O); 1656 (conj. ketone C=O); 1604 (aromatic C-C); 1246 (C-O); 1167, 1150 (CF$_3$)

N-(Adamantan-1-yl)-2-methyl-2-(4-(4-(trifluoromethyl)benzoyl)phenoxy)propanamide (31d)
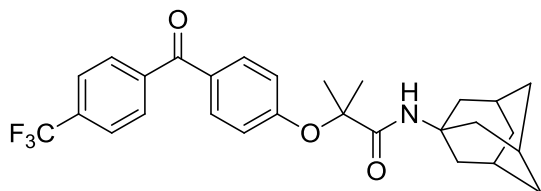
According to General Method E, **38a** (0.050g, 0.14mmol) was reacted with 1-admantylamine (0.026g, 0.17mmol), HBTU (0.065g, 0.17mmol), and Et$_3$N (0.024ml, 0.17mmol) for 24 hours in DCM (5ml) to afford **31d**.

Yield: 88%

Appearance: White solid

Purification: Radial thin-layer chromatography. DCM/hexane (1:1) to pure DCM

Melting Point: 151-152°C

m/z (ESI+) [MH]$^+$: Calculated 486.2256, found 486.2248

^{1}H NMR (396 MHz, CDCl$_3$): δ 7.86 (d, J = 8.1 Hz, 2H), 7.79 (d, J = 8.9 Hz, 2H), 7.75 (d, J = 8.1 Hz, 2H), 6.98 (d, J = 8.9 Hz, 2H), 6.06 (s, 1H), 2.07 (br s, 3H), 1.99 – 1.94 (m, 6H), 1.70 – 1.64 (m, 6H), 1.58 (br s, 6H)

^{13}C NMR (100 MHz, CDCl$_3$): δ 194.38, 172.82, 159.20, 132.14, 130.76, 129.95, 125.44, 125.40, 119.14, 82.07, 51.86, 41.38, 36.32, 29.43, 25.27

FT-IR (KBr): cm^{-1} 3422 (amide NH); 1687 (amide C=O); 1660 (conj. ketone C=O); 1597 (aromatic C-C); 1276 (C-O); 1175, 1143 (CF$_3$)

***N*-(Piperidin-1-yl)-2-(4-(4-hydroxybenzoyl)phenoxy)-2-methylpropanamide (32a)**
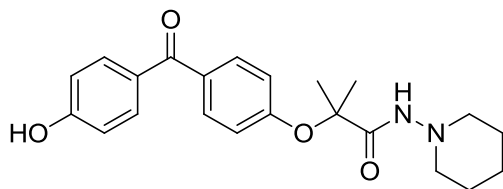
According to General Method E, **38b** (0.070g, 0.23mmol) was reacted with 1-aminopiperidine (0.030ml, 0.28mmol), HBTU (0.106g, 0.28mmol), and Et$_3$N (0.039ml, 0.28mmol) for 23 hours 30 minutes in DCM (5ml) to afford **32a**.

Yield: 29%

Appearance: White solid

Purification: Radial thin-layer chromatography. CHCl$_3$. Product then precipitated out of CHCl$_3$ upon addition of hexane.

Melting Point: 217-218°C

m/z (ESI+) [MH]$^+$: Calculated 383.1971, found 383.1968

^{1}H NMR (400 MHz, CDCl$_3$): δ 7.79 – 7.69 (m, 4H), 7.02 – 6.92 (m, 4H), 2.74 – 2.63 (m, 4H), 1.71 – 1.63 (m, 4H), 1.62 (s, 6H), 1.42 – 1.33 (m, 2H)

^{13}C NMR (100 MHz, CDCl$_3$): δ 195.32, 171.53, 161.67, 157.71, 132.72, 131.66, 128.92, 119.28, 115.15, 81.33, 56.61, 25.15, 23.05

FT-IR (KBr): cm^{-1} 3437 (phenolic OH); 3236 (amide NH); 1659 (amide C=O); 1645 (conj. ketone C=O); 1588 (aromatic C-C); 1238, 1151 (C-O)

***N*-(*exo*-Norborn-2-yl)-2-(4-(4-hydroxybenzoyl)phenoxy)-2-methyl propanamide (32b)**
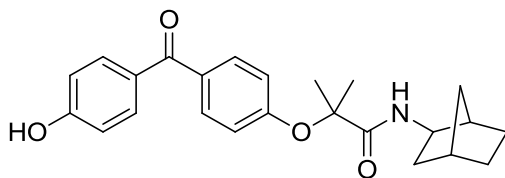
According to General Method E, **38b** (0.050g, 0.17mmol) was reacted with exo-2-aminonorbornane (0.024ml, 0.20mmol), HBTU (0.076g, 0.20mmol), and Et$_3$N (0.028ml, 0.20mmol) for 24 hours in DCM (5ml) to afford **32b**.

Yield: 30%

Appearance: White solid

Purification: Radial thin-layer chromatography. EtOAc/hexane (1:9) to EtOAc/hexane (1:1)

Melting Point: 117-119°C

**m/z (ESI+) [MH]$^+$:** Calculated 394.2018, found 394.2022

^{1}H NMR (400 MHz, CDCl$_3$): δ 7.75 (d, *J* = 8.8 Hz, 4H), 6.98 – 6.94 (m, 4H), 6.41 (d, *J* = 7.5 Hz, 1H), 3.75 (td, *J* = 7.7, 3.5 Hz, 1H), 2.27 – 2.18 (m, 2H), 1.87 – 1.75 (m, 1H), 1.59 (d, *J* = 2.6 Hz, 6H), 1.55 – 1.39 (m, 2H), 1.28 – 1.22 (m, 2H), 1.18 – 1.09 (m, 4H)

^{13}C NMR (100 MHz, CDCl$_3$): δ 194.86, 173.73, 157.85, 132.78, 131.77, 119.59, 115.36, 81.81, 52.98, 42.24, 40.16, 38.78, 35.72, 35.61, 28.15, 26.42, 25.58, 25.07

FT-IR (KBr): cm^{-1} 3281 (phenolic OH); 3281 (amide NH); 1652 (amide C=O); 1638 (conj. ketone C=O); 1605 (aromatic C-C); 1250, 1150 (C-O)

N-(R-(+)-Born-2-yl)-2-(4-(4-hydroxybenzoyl)phenoxy)-2-methylpropanamide (32c)
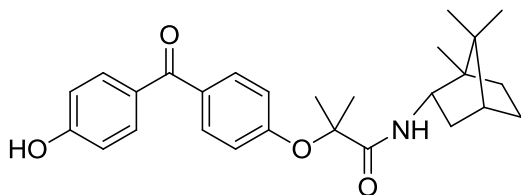
According to General Method E, **38b** (0.040g, 0.13mmol) was reacted with *R*(+)-bornylamine (0.025mg, 0.16mmol), HBTU (0.061g, 0.16mmol), and Et₃N (0.023ml, 0.16mmol) for 24 hours in DCM (5ml) to afford **32c**.

Yield: 40%

Appearance: White solid

Purification: Radial thin-layer chromatography. EtOAc/hexane (1:9) to EtOAc/hexane (1:1)

Melting Point: 82-85°C

m/z (ESI+) [MH]⁺: Calculated 436.2488, found 436.2482

¹H NMR (400 MHz, CDCl₃): δ 7.77 − 7.70 (m, 4H), 6.99 (d, *J* = 8.8 Hz, 2H), 6.90 (d, *J* = 8.7 Hz, 2H), 6.61 (d, *J* = 9.2 Hz, 1H), 4.27 − 4.20 (m, 1H), 2.39 − 2.30 (m, 1H), 1.96 (br s, 1H), 1.76 − 1.69 (m, 1H), 1.67 − 1.65 (m, 1H), 1.61 (d, *J* = 6.6 Hz, 6H), 1.34 − 1.22 (m, 2H), 1.08 (ddd, *J* = 13.4, 8.6, 5.4 Hz, 1H), 0.95 (s, 3H), 0.85 (s, 3H), 0.79 (s, 3H), 0.74 (dd, *J* = 13.4, 4.5 Hz, 1H)

¹³C NMR (100 MHz, CDCl₃): δ 194.80, 174.57, 157.91, 132.77, 131.81, 119.45, 115.33, 82.01, 53.98, 49.59, 48.28, 37.48, 28.35, 27.93, 25.65, 25.34, 19.80, 18.65, 13.84

FT-IR (KBr): cm⁻¹ 3227 (phenolic OH); 3227 (amide NH); 1652 (amide C=O); 1602 (conj. ketone C=O); 1282, 1151 (C-O)

N-(Adamantan-1-yl)-2-(4-(4-hydroxybenzoyl)phenoxy)-2-methylpropanamide (32d)

According to General Method E, **38b** (0.070g, 0.23mmol) was reacted with 1-adamantylamine (0.042mg, 0.28mmol), HBTU (0.132g, 0.28mmol), and Et$_3$N (0.049ml, 0.28mmol) for 48 hours in DCM (5ml) to afford **32d**.

Yield: 39%

Appearance: White crystals

Purification: Radial thin-layer chromatography. EtOAc/hexane (3:7). Product was then recrystallized from CHCl$_3$/hexane

Melting Point: 172-173°C

m/z (ESI+) [MH]$^+$: Calculated 434.2330, found 434.2331

^{1}H NMR (400 MHz, CDCl$_3$): δ 7.80 – 7.73 (m, 4H), 7.03 (s, 1H), 6.99 – 6.94 (m, 4H), 6.22 (s, 1H), 2.07 (br s, 3H), 1.99 (br s, 6H), 1.67 (br s, 6H), 1.58 (br s, 6H)

^{13}C NMR (100 MHz, CDCl$_3$): δ 194.98, 173.62, 160.80, 158.03, 132.81, 132.57, 131.80, 129.83, 119.34, 115.36, 81.89, 52.05, 41.34, 36.30, 29.42, 25.28

FT-IR (KBr): cm^{-1} 3207 (phenolic OH); 3207 (amide NH); 1637 (amide C=O); 1608 (conj. ketone C=O); 1283, 1150 (C-O)

2-Methyl-3-phenylmaleic anhydride (40)
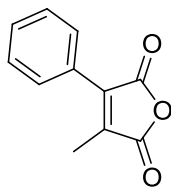
To anhydrous 1,2 dichloroethane (25ml) under a N_2 atmosphere, ethyl benzoylformate (1.00ml, 6.30mmol), propionic anhydride (1.62ml, 12.60mmol), $TiCl_4$ (2.76ml of a 1:1 solution of $TiCl_4$/DCM, 12.60mmol), and *n*-Bu$_3$N (1.80ml, 7.56mmol) were added. The reaction mixture was then refluxed for 12 hours. It was then cooled to 0°C and a saturated solution of aqueous NH_4Cl (10ml) was added, and the resulting mixture was stirred for 30 minutes. 10ml of water was added, and the organic layer was then separated. The aqueous layer was then extracted with DCM (2 x 15ml) before being discarded, and the combined organic extract was washed with 2M HCl (20ml), water (20ml), and brine (20ml) before being dried over anhydrous Na_2SO_4, and the solvent removed under vacuum.

Yield: 28%

Appearance: White solid

Purification: Column chromatography. EtOAc/hexane (1:19) to EtOAc/hexane (3:7).

Melting Point: 90-92°C. Reported 98-100°C.

m/z (ESI+) [MH]$^+$: Calculated 189.0551, found 189.0546

^{1}H NMR (400 MHz, CDCl$_3$): δ 7.66 (dd, *J* = 6.8, 3.0 Hz, 2H), 7.56 – 7.50 (m, 3H), 2.33 (s, 3H)

FT-IR (KBr): cm^{-1} 1764 (anhydride C=O); 1268 (anhydride C-O); 922 (alkene =C-H)

N-exo-Norborn-2-yl-2-methyl-3phenylmaleimide (41)
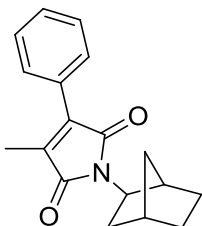
To a solution of **40** (0.030g, 0.16mmol) in anhydrous toluene (3ml) under a N_2 atmosphere, a solution of *exo*-2-aminonorbornane (0.018g, 0.16mmol) in anhydrous toluene was added dropwise. The reaction mixture was stirred for 1 hour. Anhydrous ZnI_2 (0.051g, 0.16mmol) was then added and the reaction mixture was heated to reflux. A solution of HMDS in anhydrous toluene (0.039g, 0.24mmol) was then added in three portions over 30 minutes. The reaction mixture was then refluxed for a further 2 hours. The reaction mixture was then cooled and poured into 0.5M HCl. The aqueous layer was extracted with EtOAc, and the combined organic layers was washed with saturated aq. $NaHCO_3$ and brine, dried over anhydrous Na_2SO_4 and the solvent removed under vacuum.

Yield: 86%

Appearance: Yellow oil

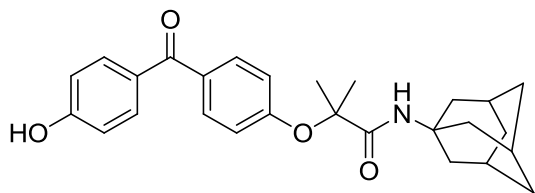**Purification:** Radial thin-layer chromatography. EtOAc/hexane (1:99) to EtOAc/hexane (1:9)

m/z (ESI+) [MH]$^+$: Calculated 282.1494, found 282.1496

^{1}H NMR (400 MHz, CDCl$_3$): δ 7.55 (dd, J = 8.2, 1.6 Hz, 2H), 7.51 − 7.38 (m, 3H), 4.07 − 3.96 (m, 1H), 2.38 (d, J = 19.9 Hz, 2H), 2.23 − 2.18 (m, 2H), 2.16 (s, 3H), 1.68 (ddd, J = 12.5, 8.9, 2.2 Hz, 1H), 1.60 − 1.49 (m, 2H), 1.32 (td, J = 8.6, 2.1 Hz, 1H), 1.26 − 1.15 (m, 2H)

FT-IR (KBr): cm^{-1} 2957 (alkyl C-H); 1698 (imide C=O); 1371 (imide C-N); 694 (alkene =C-H)

8.3 Pharmacology

8.3.1 Cell culture method

Chinese Hamster Ovary (CHO) cells stably expressing the human CB2 receptor were provided by Pfizer Neusentis Ltd. All cell culture procedures were performed under sterile conditions in a class II laminar flow cabinet. All culture reagents were warmed to 37°C prior to use. Cells were cultured in 175cm^2 culture flasks containing Dulbecco's Modified Eagle Medium: Nutrient Mixture F12 (DMEM/F12) supplemented with 10% fetal bovine serum, 2mM L-glutamine and 400 µg/ml G 418. Cells were cultured for 2-3 days in a humidified incubator (37°C, 5 % CO$_2$) until ~90% confluent, and then passaged. Cells were washed once with phosphate-buffered saline (PBS), and then incubated with a trypsin/EDTA solution for approximately 3 minutes to allow detachment of the cells from the culture flask. The cell suspension was diluted in culture medium to deactivate the trypsin, and then cells were collected by centrifugation at 200g for 3 minutes. The cell pellet was suspended in fresh culture medium, and the number of cells determined using a Bio-Rad TC10™ Automated Cell Counter. Cells were subsequently reseeded into new culture flasks containing fresh culture medium.

8.3.2 Preparation of membrane homogenates

The procedure was adapted from method previously described in (284). Once the cells were confluent, trypsin was added to the culture flasks for no more than1 minute to allow for cell detachment but to minimize proteolytic degradation of the surface proteins. Cells were then collected by centrifugation at 200g for 3 min. All subsequent steps were performed at 0 -4°C. Cell pellets were resuspended in cold homogenization buffer (50 mM Tris, 5mM MgCl$_2$, 2mM EDTA, pH 7.4), combined, and homogenized using a Polytron homogenizer. The suspension was then centrifuged (30,000g for 10 minutes at 4°C), and the supernatant discarded. The pellet was then

resuspended in fresh homogenization buffer and the process was repeated twice. The final membrane pellet was then resuspended in homogenization buffer and the protein concentration was determined by Lowry protein assay (285). The membrane concentration was then adjusted to 2.5 mg/ml protein and was stored in aliquots at -80°C.

8.3.3 [^{3}H]CP55940 competition binding assay procedure

The assay was adapted from the method previously described in (179). To assay tubes containing 850μl of assay buffer (50mM Tris, 2mM EDTA, 5mM MgCl$_2$, 0.2mg/ml BSA, pH 7.0 at 30°C), 50μl of [^{3}H]CP55940 (~0.5nM) in drug buffer (50mM Tris, 2mM EDTA, 5mM MgCl$_2$, 5mg/ml BSA, pH 7.0 at 30°C), 50μl of competing ligand (concentration range 30μM to 0.1nM) in drug buffer, and 50μl of CB2 receptor-expressing CHO cells membrane homogenate (1mg/ml) was added, giving a final assay volume of 1ml. Basal binding levels were determined using drug buffer without any competing ligand. Non-specific binding (NSB) was determined in the presence of 1μM of unlabeled CP55940. All data points were carried out in duplicate. The assay tubes were vortexed for 1-2 seconds, and were then incubated in a water bath at 30°C for 90 minutes.

Following incubation, the membranes were harvested using a cell filter harvester (M-24 Cell Harvester, Brandel) and glass fiber filters (GF/B filters, Brandel) pre-soaked with drug buffer, and were washed with cold buffer (50mM Tris, 2mM EDTA, 5mM MgCl$_2$, 0.5mg/ml BSA, pH 7.0 at 4°C) three times to separate bound and unbound ligand. The filters were then collected in scintillation vials and 3ml of scintillation fluid (Ultima Gold™ XR, Perkin Elmer) was added to each vial. The bound radioligand was then quantified using a liquid scintillation counter (Tri-Carb 2100TR Liquid Scintillation Analyzer, Packard).

Specific binding was calculated by subtracting NSB from total binding. Non-linear regression analysis was then performed using GraphPad Prism 5, and the K_i value of each ligand was determined using the Cheng-Prusoff equation. The exact concentration of [^{3}H]CP55940 was

calculated in each experiment using the mean total activity of 3 vials containing 50µl of unfiltered [³H] CP55940, while the K_d of [³H]CP55940 was previously determined to be 0.5nM.

8.3.4 [³⁵S]GTPγS binding assay procedure

The assay was adapted from the method previously described in reference (22). A mixture of CB2 receptor-expressing CHO cells membrane homogenate (50µg/ml) and GDP (0.1mM) in assay buffer (50mM Tris, 100mM NaCl, 10mM $MgCl_2$, 0.2mg/ml BSA, pH 7.4 at 30°C) was incubated in water bath at 30°C for 20 minutes. Following incubation, 0.5ml of this mixture was added to assay tubes containing 450µl of [³⁵S]GTPγS (0.044nM) and 50µl of ligand (concentration range 10µM to 0.1nM) in drug buffer (50mM Tris, 100mM NaCl, 10mM $MgCl_2$, 5mg/ml BSA, pH 7.4 at 30°C), giving a final assay volume of 1ml. Basal levels were determined using drug buffer without any ligand. Non-specific binding was determined in the presence of 10µM unlabeled GTPγS. The maximal agonist-enhanced response was determined in the presence of 1µM CP55940. All data points were carried out in duplicate. The assay tubes were vortexed for 1-2 seconds, and were then incubated in a water bath at 30°C for 90 minutes.

Following incubation, the membranes were harvested using a cell filter harvester and glass fiber filters (GF/C filters, Brandel), and were washed with cold distilled water three times. The filters were then collected in scintillation vials and 3ml of scintillation fluid was added to each vial. The bound [³⁵S] GTPγS was then quantified using a liquid scintillation counter.

Specific binding was calculated by subtracting NSB from total binding. Non-linear regression analysis was then performed using GraphPad Prism 5 in order to determine the E_{max} and the EC_{50}. Results were expressed as a % of the maximal response.

9 REFERENCES

(1)   Fredriksson, R.; Lagerstrom, M. C.; Lundin, L. G.; Schioth, H. B. The G-Protein-Coupled Receptors in the Human Genome Form Five Main Families. Phylogenetic Analysis, Paralogon Groups, and Fingerprints. *Mol. Pharmacol.* **2003**, *63*, 1256–1272.

(2)   Vauquelin, G.; von Mentzer, B. G-Protein Coupled Receptors. *Mol. Pharmacol. New Jersey Wiley* **2007**.

(3)   Civelli, O. GPCR Deorphanizations: The Novel, the Known and the Unexpected Transmitters. *Trends Pharmacol. Sci.* **2005**, *26*, 15–19.

(4)   Kolakowski Jr, L. F. GCRDb: A G-Protein-Coupled Receptor Database. *Receptors Channels* **1994**, *2*, 1.

(5)   Oldham, W. M.; Hamm, H. E. Heterotrimeric G Protein Activation by G-Protein-Coupled Receptors. *Nat. Rev. Mol. Cell Biol.* **2008**, *9*, 60–71.

(6)   Marinissen, M. J.; Gutkind, J. S. G-Protein-Coupled Receptors and Signaling Networks: Emerging Paradigms. *Trends Pharmacol. Sci.* **2001**, *22*, 368–376.

(7)   Janz, J. M.; Farrens, D. L. Rhodopsin Activation Exposes a Key Hydrophobic Binding Site for the Transducin Alpha-Subunit C Terminus. *J. Biol. Chem.* **2004**, *279*, 29767–29773.

(8)   Patrick, G. L.; Spencer, J. *An Introduction to Medicinal Chemistry*; Oxford University Press Oxford, **2001**; Vol. 134.

(9)   Hamm, H. E. The Many Faces of G Protein Signaling. *J. Biol. Chem.* **1998**, *273*, 669–672.

(10)   Sunahara, R. K.; Dessauer, C. W.; Gilman, A. G. Complexity and Diversity of Mammalian Adenylyl Cyclases. *Annu. Rev. Pharmacol. Toxicol.* **1996**, *36*, 461–480.

(11)   Krapivinsky, G.; Krapivinsky, L.; Wickman, K.; Clapham, D. E. G-Beta-Gamma Binds Directly to the G-Protein-Gated K+ Channel, IKACh. *J. Biol. Chem.* **1995**, *270*, 29059–29062.

(12)   Tang, X. W.; Downes, C. P. Purification and Characterization of G Beta Gamma-Responsive Phosphoinositide 3-Kinases from Pig Platelet Cytosol. *J. Biol. Chem.* **1997**, *272*, 14193–14199.

(13)   Camps, M.; Carozzi, A.; Schnabel, P.; Scheer, A.; Parker, P. J.; Gierschik, P. Isozyme-Selective Stimulation of Phospholipase C-Beta-2 by G-Protein Beta-Gamma-Subunits. *Nature* **1992**, *360*, 684–686.

(14)   Boyer, J. L.; Waldo, G. L.; Harden, T. K. Beta-Gamma-Subunit Activation of G-Protein-Regulated Phospholipase-C. *J. Biol. Chem.* **1992**, *267*, 25451–25456.

(15)   McDonald, P. H.; Chow, C. W.; Miller, W. E.; Laporte, S. A.; Field, M. E.; Lin, F. T.; Davis, R. J.; Lefkowitz, R. J. Beta-Arrestin 2: A Receptor-Regulated MAPK Scaffold for the Activation of JNK3. *Science.* **2000**, *290*, 1574–1577.

(16)   Hall, R. A.; Premont, R. T.; Lefkowitz, R. J. Heptahelical Receptor Signaling: Beyond the G Protein Paradigm. *J. Cell Biol.* **1999**, *145*, 927–932.

(17)   Hopkins, A. L.; Groom, C. R. The Druggable Genome. *Nat. Rev. Drug Discov.* **2002**, *1*, 727–730.

(18)   Thomsen, W.; Frazer, J.; Unett, D. Functional Assays for Screening GPCR Targets. *Curr. Opin. Biotechnol.* **2005**, *16*, 655–665.

(19)   Tate, C. G. A Crystal Clear Solution for Determining G-Protein-Coupled Receptor Structures. *Trends in Biochemical Sciences*, **2012**, *37*, 343–352.

(20)   Davenport, A. P, *Receptor Binding Techniques*; 3rd Ed.; Springer: New York, **2012**.

(21)   Cheng, Y.; Prusoff, W. H. Relationship between the Inhibition Constant (K1) and the Concentration of Inhibitor Which Causes 50 per Cent Inhibition (I50) of an Enzymatic Reaction. *Biochem. Pharmacol.* **1973**, *22*, 3099–3108.

(22)   Griffin, G.; Tao, Q.; Abood, M. E. Cloning and Pharmacological Characterization of the Rat CB(2) Cannabinoid Receptor. *J. Pharmacol. Exp. Ther.* **2000**, *292*, 886–894.

(23)   Rosenbaum, D. M.; Rasmussen, S. G. F.; Kobilka, B. K. The Structure and Function of G-Protein-Coupled Receptors. *Nature* **2009**, *459*, 356–363.

(24)   Palczewski, K.; Kumasaka, T.; Hori, T.; Behnke, C. A.; Motoshima, H.; Fox, B. A.; Le Trong, I.; Teller, D. C.; Okada, T.; Stenkamp, R. E.; et al. Crystal Structure of Rhodopsin: A G Protein-Coupled Receptor. *Science.* **2000**, *289*, 739–745.

(25)   Okada, T.; Le Trong, I.; Fox, B. A.; Behnke, C. A.; Stenkamp, R. E.; Palczewski, K. X-Ray Diffraction Analysis of Three-Dimensional Crystals of Bovine Rhodopsin Obtained from Mixed Micelles. *J. Struct. Biol.* **2000**, *130*, 73–80.

(26)   Rasmussen, S. G. F.; Choi, H. J.; Rosenbaum, D. M.; Kobilka, T. S.; Thian, F. S.; Edwards, P. C.; Burghammer, M.; Ratnala, V. R. P.; Sanishvili, R.; Fischetti, R. F.; et al. Crystal Structure of the Human beta(2) Adrenergic G-Protein-Coupled Receptor. *Nature* **2007**, *450*, 383–387.

(27)   Rosenbaum, D. M.; Cherezov, V.; Hanson, M. A.; Rasmussen, S. G. F.; Thian, F. S.; Kobilka, T. S.; Choi, H. J.; Yao, X. J.; Weis, W. I.; Stevens, R. C.; et al. GPCR Engineering Yields High-Resolution Structural Insights into beta(2)-Adrenergic Receptor Function. *Science* **2007**, *318*, 1266–1273.

(28)   Jaakola, V. P.; Griffith, M. T.; Hanson, M. A.; Cherezov, V.; Chien, E. Y. T.; Lane, J. R.; Ijzerman, A. P.; Stevens, R. C. The 2.6 Angstrom Crystal Structure of a Human A(2A) Adenosine Receptor Bound to an Antagonist. *Science* **2008**, *322*, 1211–1217.

(29)   Warne, T.; Serrano-Vega, M. J.; Baker, J. G.; Moukhametzianov, R.; Edwards, P. C.; Henderson, R.; Leslie, A. G. W.; Tate, C. G.; Schertler, G. F. X. Structure of a Beta 1-Adrenergic G-Protein-Coupled Receptor. *Nature* **2008**, *454*, 486–491.

(30)   Rasmussen, S. G. F.; Choi, H.-J.; Fung, J. J.; Pardon, E.; Casarosa, P.; Chae, P. S.; Devree, B. T.; Rosenbaum, D. M.; Thian, F. S.; Kobilka, T. S.; et al. Structure of a Nanobody-Stabilized Active State of the β(2) Adrenoceptor. *Nature* **2011**, *469*, 175–180.

(31)   Caffrey, M. Crystallizing Membrane Proteins for Structure Determination: Use of Lipidic Mesophases. *Annu. Rev. Biophys.* **2009**, *38*, 29–51.

(32)   Faham, S.; Bowie, J. U. Bicelle Crystallization A New Method for Crystallizing Membrane Proteins Yields a Monomeric Bacteriorhodopsin Structure. *J. Mol. Biol.* **2002**, *316*, 1–6.

(33)   Wu, B. L.; Chien, E. Y. T.; Mol, C. D.; Fenalti, G.; Liu, W.; Katritch, V.; Abagyan, R.; Brooun, A.; Wells, P.; Bi, F. C.; et al. Structures of the CXCR4 Chemokine GPCR with Small-Molecule and Cyclic Peptide Antagonists. *Science* **2010**, *330*, 1066–1071.

(34)   Chien, E. Y. T.; Liu, W.; Zhao, Q. A.; Katritch, V.; Han, G. W.; Hanson, M. A.; Shi, L.; Newman, A. H.; Javitch, J. A.; Cherezov, V.; et al. Structure of the Human Dopamine D3 Receptor in Complex with a D2/D3 Selective Antagonist. *Science* **2010**, *330*, 1091–1095.

(35)   Shimamura, T.; Shiroishi, M.; Weyand, S.; Tsujimoto, H.; Winter, G.; Katritch, V.; Abagyan, R.; Cherezov, V.; Liu, W.; Han, G. W.; et al. Structure of the Human Histamine H1 Receptor Complex with Doxepin. *Nature* **2011**, *475*, 65–70.

(36)   Haga, K.; Kruse, A. C.; Asada, H.; Yurugi-Kobayashi, T.; Shiroishi, M.; Zhang, C.; Weis, W. I.; Okada, T.; Kobilka, B. K.; Haga, T.; et al. Structure of the Human M2 Muscarinic Acetylcholine Receptor Bound to an Antagonist. *Nature* **2012**, *482*, 547–551.

(37)   Kruse, A. C.; Hu, J.; Pan, A. C.; Arlow, D. H.; Rosenbaum, D. M.; Rosemond, E.; Green, H. F.; Liu, T.; Chae, P. S.; Dror, R. O.; et al. Structure and Dynamics of the M3 Muscarinic Acetylcholine Receptor. *Nature* **2012**, *482*, 552–556.

(38)   Wu, H.; Wacker, D.; Mileni, M.; Katritch, V.; Han, G. W.; Vardy, E.; Liu, W.; Thompson, A. A.; Huang, X.-P.; Carroll, F. I.; et al. Structure of the Human K-Opioid Receptor in Complex with JDTic. *Nature* **2012**, *485*, 327–332.

(39)   Manglik, A.; Kruse, A. C.; Kobilka, T. S.; Thian, F. S.; Mathiesen, J. M.; Sunahara, R. K.; Pardo, L.; Weis, W. I.; Kobilka, B. K.; Granier, S. Crystal Structure of the M-Opioid Receptor Bound to a Morphinan Antagonist. *Nature* **2012**, *485*, 321–326.

(40)   White, J. F.; Noinaj, N.; Shibata, Y.; Love, J.; Kloss, B.; Xu, F.; Gvozdenovic-Jeremic, J.; Shah, P.; Shiloach, J.; Tate, C. G.; et al. Structure of the Agonist-Bound Neurotensin Receptor. *Nature* **2012**, *490*, 508–513.

(41)   Thompson, A. A.; Liu, W.; Chun, E.; Katritch, V.; Wu, H.; Vardy, E.; Huang, X.-P.; Trapella, C.; Guerrini, R.; Calo, G.; et al. Structure of the Nociceptin/orphanin FQ Receptor in Complex with a Peptide Mimetic. *Nature* **2012**, *485*, 395–399.

(42)   Zhang, C.; Srinivasan, Y.; Arlow, D. H.; Fung, J. J.; Palmer, D.; Zheng, Y.; Green, H. F.; Pandey, A.; Dror, R. O.; Shaw, D. E.; et al. High-Resolution Crystal Structure of Human Protease-Activated Receptor 1. *Nature* **2012**, *492*, 387–392.

(43)   Hanson, M. A.; Roth, C. B.; Jo, E.; Griffith, M. T.; Scott, F. L.; Reinhart, G.; Desale, H.; Clemons, B.; Cahalan, S. M.; Schuerer, S. C.; et al. Crystal Structure of a Lipid G Protein-Coupled Receptor. *Science* **2012**, *335*, 851–855.

(44)   Hollenstein, K.; Kean, J.; Bortolato, A.; Cheng, R. K. Y.; Doré, A. S.; Jazayeri, A.; Cooke, R. M.; Weir, M.; Marshall, F. H. Structure of Class B GPCR Corticotropin-Releasing Factor Receptor 1. *Nature* **2013**, *499*, 438–443.

(45)   Siu, F. Y.; He, M.; de Graaf, C.; Han, G. W.; Yang, D.; Zhang, Z.; Zhou, C.; Xu, Q.; Wacker, D.; Joseph, J. S.; et al. Structure of the Human Glucagon Class B G-Protein-Coupled Receptor. *Nature* **2013**, *499*, 444–449.

(46)   Rasmussen, S. G. F.; DeVree, B. T.; Zou, Y.; Kruse, A. C.; Chung, K. Y.; Kobilka, T. S.; Thian, F. S.; Chae, P. S.; Pardon, E.; Calinski, D.; et al. Crystal Structure of the β2 Adrenergic Receptor-Gs Protein Complex. *Nature* **2011**, *477*, 549–555.

(47)   Ballesteros, J. A.; Weinstein, H. Integrated Methods for the Construction of Three-Dimensional Models and Computational Probing of Structure-Function Relations in G Protein-Coupled Receptors. *Methods Neurosci.* **1995**, *25*, 366–428.

(48)   Venkatakrishnan, a J.; Deupi, X.; Lebon, G.; Tate, C. G.; Schertler, G. F.; Babu, M. M. Molecular Signatures of G-Protein-Coupled Receptors. *Nature* **2013**, *494*, 185–194.

(49)   Iversen, L. L. *The Science of Marijuana*; Oxford University Press, USA, **2000**.

(50)   Lambert, D. M.; Fowler, C. J. The Endocannabinoid System: Drug Targets, Lead Compounds, and Potential Therapeutic Applications. *J. Med. Chem.* **2005**, *48*, 5059–5087.

(51)   Lawrence, D. K.; Gill, E. W. The Effects of 1-Tetrahydrocannabinol and Other Cannabinoids on Spin-Labeled Liposomes and Their Relationship to Mechanisms of General Anesthesia. *Mol. Pharmacol.* **1975**, *11*, 595.

(52)   Gaoni, Y.; Mechoulam, R. Isolation, Structure, and Partial Synthesis of an Active Constituent of Hashish. *J. Am. Chem. Soc.* **1964**, *86*, 1646–1647.

(53)   Hollister, L. E. Structure-Activity Relationships in Man of Cannabis Constituents, and Homologs and Metabolites of Delta-9-Tetrahydrocannabinol. *Pharmacology* **1974**, *11*, 3–11.

(54)   Jones, G.; Pertwee, R. G.; Gill, E. W.; Paton, W. D. M.; Nilsson, I. M.; Widman, M.; Agurell, S. Relative Pharmacological Potency in Mice of Optical Isomers of [Delta] 1-Tetrahydrocannabinol. *Biochem. Pharmacol.* **1974**, *23*, 439–446.

(55)   Devane, W. A.; Dysarz, F. A.; Johnson, M. R.; Melvin, L. S.; Howlett, A. C. Determination and Characterization of a Cannabinoid Receptor in Rat-Brain. *Mol. Pharmacol.* **1988**, *34*, 605–613.

(56)   Matsuda, L. A.; Lolait, S. J.; Brownstein, M. J.; Young, A. C.; Bonner, T. I. Structure of a Cannabinoid Receptor and Functional Expression of the Cloned cDNA. *Nature.* **1990**, *346*, 561–564.

(57)   Osei-Hyiaman, D.; DePetrillo, M.; Pacher, P.; Liu, J.; Radaeva, S.; Batkai, S.; Harvey-White, J.; Mackie, K.; Offertaler, L.; Wang, L.; et al. Endocannabinoid Activation at Hepatic CB1 Receptors Stimulates Fatty Acid Synthesis and Contributes to Diet-Induced Obesity. *J. Clin. Invest.* **2005**, *115*, 1298–1305.

(58)   Cavuoto, P.; McAinch, A. J.; Hatzinikolas, G.; Janovska, A.; Game, P.; Wittert, G. A. The Expression of Receptors for Endocannabinoids in Human and Rodent Skeletal Muscle. *Biochem. Biophys. Res. Commun.* **2007**, *364*, 105–110.

(59)   Cota, D.; Marsicano, G.; Tschop, M.; Grubler, Y.; Flachskamm, C.; Schubert, M.; Auer, D.; Yassouridis, A.; Thone-Reineke, C.; Ortmann, S.; et al. The Endogenous Cannabinoid System Affects Energy Balance via Central Orexigenic Drive and Peripheral Lipogenesis. *J. Clin. Invest.* **2003**, *112*, 423–431.

(60)   Juan-Pico, P.; Fuentes, E.; Bermudez-Silva, F. J.; Diaz-Molina, F. J.; Ripoll, C.; de Fonseca, F. R.; Nadal, A. Cannabinoid Receptors Regulate Ca2+ Signals and Insulin Secretion in Pancreatic Beta-Cell. *Cell Calcium* **2006**, *39*, 155–162.

(61)   Munro, S.; Thomas, K. L.; Abushaar, M. Molecular Characterization of a Peripheral Receptor for Cannabinoids. *Nature.* **1993**, *365*, 61–65.

(62)   Suarez, J.; Javier Bermudez-Silva, F.; Mackie, K.; Ledent, C.; Zimmer, A.; Cravatt, B. F.; Rodriguez de Fonseca, F. Immunohistochemical Description of the Endogenous Cannabinoid System in the Rat Cerebellum and Functionally Related Nuclei. *J. Comp. Neurol.* **2008**, *509*, 400–421.

(63)   Roche, R.; Hoareau, L.; Bes-Houtmann, S.; Gonthier, M.-P.; Laborde, C.; Baron, J.-F.; Haffaf, Y.; Cesari, M.; Festy, F. Presence of the Cannabinoid Receptors, CB1 and CB2, in Human Omental and Subcutaneous Adipocytes. *Histochem. Cell Biol.* **2006**, *126*, 177–187.

(64)   Pertwee, R. G.; Howlett, A. C.; Abood, M. E.; Alexander, S. P. H.; Di Marzo, V.; Elphick, M. R.; Greasley, P. J.; Hansen, H. S.; Kunos, G.; Mackie, K.; et al. International Union of Basic and Clinical Pharmacology. LXXIX. Cannabinoid Receptors and Their Ligands: Beyond CB1 and CB2. *Pharmacol. Rev.* **2010**, *62*, 588–631.

(65)   Devane, W. A.; Hanus, L.; Breuer, A.; Pertwee, R. G.; Stevenson, L. A.; Griffin, G.; Gibson, D.; Mandelbaum, A.; Etinger, A.; Mechoulam, R. Isolation and Structure of a Brain Constituent That Binds to the Cannabinoid Receptor. *Science.* **1992**, *258*, 1946–1949.

(66)   Gonsiorek, W.; Lunn, C.; Fan, X. D.; Narula, S.; Lundell, D.; Hipkin, R. W. Endocannabinoid 2-Arachidonyl Glycerol Is a Full Agonist through Human Type 2 Cannabinoid Receptor: Antagonism by Anandamide. *Mol. Pharmacol.* **2000**, *57*, 1045–1050.

(67)   Schmid, P. C.; Reddy, P. V; Natarajan, V.; Schmid, H. H. Metabolism of N-Acylethanolamine Phospholipids by a Mammalian Phosphodiesterase of the Phospholipase D Type. *J. Biol. Chem.* **1983**, *258*, 9302.

(68)   Glaser, S. T.; Abumrad, N. A.; Fatade, F.; Kaczocha, M.; Studholme, K. M.; Deutsch, D. G. Evidence against the Presence of an Anandamide Transporter. *Proc. Natl. Acad. Sci. U. S. A.* **2003**, *100*, 4269–4274.

(69)   Mechoulam, R.; Benshabat, S.; Hanus, L.; Ligumsky, M.; Kaminski, N. E.; Schatz, A. R.; Gopher, A.; Almog, S.; Martin, B. R.; Compton, D. R.; et al. Identification of an Endogenous 2-Monoglyceride, Present in Canine Gut, That Binds to Cannabinoid Receptors. *Biochem. Pharmacol.* **1995**, *50*, 83–90.

(70)   Sugiura, T.; Kondo, S.; Sukagawa, A.; Nakane, S.; Shinoda, A.; Itoh, K.; Yamashita, A.; Waku, K. 2-Arachidonoylglycerol: A Possible Endogenous Cannabinoid Receptor-Ligand in Brain. *Biochem. Biophys. Res. Commun.* **1995**, *215*, 89–97.

(71)   Hanus, L.; Abu-Lafi, S.; Fride, E.; Breuer, A.; Vogel, Z.; Shalev, D. E.; Kustanovich, I.; Mechoulam, R. 2-Arachidonyl Glyceryl Ether, an Endogenous Agonist of the Cannabinoid CB1 Receptor. *Proc. Natl. Acad. Sci. U. S. A.* **2001**, *98*, 3662–3665.

(72)   Porter, A. C.; Sauer, J. M.; Knierman, M. D.; Becker, G. W.; Berna, M. J.; Bao, J. Q.; Nomikos, G. G.; Carter, P.; Bymaster, F. P.; Leese, A. B.; et al. Characterization of a Novel Endocannabinoid, Virodhamine, with Antagonist Activity at the CB1 Receptor. *J. Pharmacol. Exp. Ther.* **2002**, *301*, 1020–1024.

(73)   Bisogno, T.; Melck, D.; Bobrov, M. Y.; Gretskaya, N. M.; Bezuglov, V. V; De Petrocellis, L.; Di Marzo, V. N-Acyl-Dopamines: Novel Synthetic CB1 Cannabinoid-Receptor Ligands and Inhibitors of Anandamide Inactivation with Cannabimimetic Activity in Vitro and in Vivo. *Biochem. J.* **2000**, *351*, 817–824.

(74)   Huang, S. M.; Bisogno, T.; Trevisani, M.; Al-Hayani, A.; De Petrocellis, L.; Fezza, F.; Tognetto, M.; Petros, T. J.; Krey, J. F.; Chu, C. J.; et al. An Endogenous Capsaicin-like Substance with High Potency at Recombinant and Native Vanilloid VR1 Receptors. *Proc. Natl. Acad. Sci. U. S. A.* **2002**, *99*, 8400–8405.

(75)   Howlett, A. C.; Qualy, J. M.; Khachatrian, L. L. Involvement of Gi in the Inhibition of Adenylate-Cyclase by Cannabimimetic Drugs. *Mol. Pharmacol.* **1986**, *29*, 307–313.

(76)   Burstein, S.; Hunter, S. A.; Latham, V.; Mechoulam, R.; Melchior, D. L.; Renzulli, L.; Tefft, R. E. Prostaglandins and Cannabis .15. Comparison of Enantiomeric Cannabinoids in Stimulating Prostaglandin Synthesis in Fibroblasts. *Life Sci.* **1986**, *39*, 1813–1823.

(77)   Burstein, S.; Budrow, J.; Debatis, M.; Hunter, S. A.; Subramanian, A. Phospholipase Participation in Cannabinoid-Induced Release of Free Arachidonic-Acid. *Biochem. Pharmacol.* **1994**, *48*, 1253–1264.

(78)   Rhee, M. H.; Bayewitch, M.; Avidor-Reiss, T.; Levy, R.; Vogel, Z. Cannabinoid Receptor Activation Differentially Regulates the Various Adenylyl Cyclase Isozymes. *J. Neurochem.* **1998**, *71*, 1525–1534.

(79)   Glass, M.; Felder, C. C. Concurrent Stimulation of Cannabinoid CB1 and Dopamine D2 Receptors Augments cAMP Accumulation in Striatal Neurons: Evidence for a G(s) Linkage to the CB1 Receptor. *J. Neurosci.* **1997**, *17*, 5327–5333.

(80)   Felder, C. C.; Joyce, K. E.; Briley, E. M.; Glass, M.; Mackie, K. P.; Fahey, K. J.; Cullinan, G. J.; Hunden, D. C.; Johnson, D. W.; Chaney, M. O.; et al. LY320135, a Novel Cannabinoid CB1 Receptor Antagonist, Unmasks Coupling of the CB1 Receptor to Stimulation of cAMP Accumulation. *J. Pharmacol. Exp. Ther.* **1998**, *284*, 291–297.

(81)   Bonhaus, D. W.; Chang, L. K.; Kwan, J.; Martin, G. R. Dual Activation and Inhibition of Adenylyl Cyclase by Cannabinoid Receptor Agonists: Evidence for Agonist-Specific Trafficking of Intracellular Responses. *J. Pharmacol. Exp. Ther.* **1998**, *287*, 884–888.

(82)   Howlett, A. C. Cannabinoid Receptor Signaling. *Cannabinoids* **2005**, *168,* 53–79.

(83)   Pacher, P.; Batkai, S.; Kunos, G. The Endocannabinoid System as an Emerging Target of Pharmacotherapy. *Pharmacol. Rev.* **2006**, *58*, 389–462.

(84)   Williams, C. M.; Rogers, P. J.; Kirkham, T. C. Hyperphagia in Pre-Fed Rats Following Oral Delta(9)-THC. *Physiol. Behav.* **1998**, *65*, 343–346.

(85)   Cota, D. Role of the Endocannabinoid System in Energy Balance Regulation and Obesity. *Obe. Metab.* **2008**, *36*, 135–145.

(86)   Cota, D.; Woods, S. C. The Role of the Endocannabinoid System in the Regulation of Energy Homeostasis. *Curr. Opin. Endocrinol. Diabetes Obes.* **2005**, *12*, 338.

(87)   Di Marzo, V.; Goparaju, S. K.; Wang, L.; Liu, J.; Batkai, S.; Jarai, Z.; Fezza, F.; Miura, G. I.; Palmiter, R. D.; Sugiura, T.; et al. Leptin-Regulated Endocannabinoids Are Involved in Maintaining Food Intake. *Nature* **2001**, *410*, 822–825.

(88)   Ravinet Trillou, C.; Arnone, M.; Delgorge, C.; Gonalons, N.; Keane, P.; Maffrand, J.-P.; Soubrie, P. Anti-Obesity Effect of SR141716, a CB1 Receptor Antagonist, in Diet-Induced Obese Mice. *Am. J. Physiol. Regul. Integr. Comp. Physiol.* **2003**, *284*, 345–53.

(89)   Matias, I.; Gonthier, M. P.; Orlando, P.; Martiadis, V.; De Petrocellis, L.; Cervino, C.; Petrosino, S.; Hoareau, L.; Festy, F.; Pasquali, R. Regulation, Function, and Dysregulation of Endocannabinoids in Models of Adipose and B-Pancreatic Cells and in Obesity and Hyperglycemia. *J. Clin. Endocrinol. Metab.* **2006**, *91*, 3171–3180.

(90)   Despres, J. P.; Golay, A.; Sjostrom, L.; Rimonabant Obesity Lipids Study, G. Effects of Rimonabant on Metabolic Risk Factors in Overweight Patients with Dyslipidemia. *N. Engl. J. Med.* **2005**, *353*, 2121–2134.

(91)   Pi-Sunyer, F.; Aronne, L. J.; Heshmati, H. M.; Devin, J.; Rosenstock, J.; Grp, R.-N. A. S. Effect of Rimonabant, a Cannabinoid-1 Receptor Blocker, on Weight and Cardiometabolic Risk Factors in Overweight or Obese Patients - RIO-North America: A Randomized Controlled Trial. *Jama-Journal Am. Med. Assoc.* **2006**, *295*, 761–775.

(92)   Scheen, A. J.; Finer, N.; Hollander, P.; Jensen, M. D.; Van Goal, L. F.; Grp, R. I.-D. S. Efficacy and Tolerability of Rimonabant in Overweight or Obese Patients with Type 2 Diabetes: A Randomised Controlled Study. *Lancet* **2006**, *368*, 1660–1672.

(93)   Van Gaal, L.; Pt-Sunyer, X.; Despres, J.-P.; McCarthy, C.; Scheen, A. Efficacy and Safety of Rimonabant for Improvement of Multiple Cardiometabolic Risk Factors in Overweight/Obese Patients Pooled 1-Year Data from the Rimonabant in Obesity (RIO) Program. *Diabetes Care* **2008**, *31*, S229–S240.

(94)   U.S Food & Drug Administration. FDA briefing document: new drug application 21-888. Zimulti (rimonabant). Rockville, MD http://www.fda.gov/ohrms/dockets/AC/07/ briefing/2007-4306b1-fda-backgrounder.pdf. Accessed July 2012.

(95)   European Medicines Agency. Doc. Ref. EMEA/537153/2008 questions and answers on the recommendation to suspend the marketing authorisation of Accomplia (rimonabant).

(96)   Andrews, P. L. R.; Hawthorn, J. The Neurophysiology of Vomiting. *Baillieres. Clin. Gastroenterol.* **1988**, *2*, 141–168.

(97)   Morales, M.; Wang, S. D.; Diaz-Ruiz, O.; Jho, D. H. J. Cannabinoid CB1 Receptor and Serotonin 3 Receptor Subunit a (5-HT(3A)) Are Co-Expressed in GABA Neurons in the Rat Telencephalon. *J. Comp. Neurol.* **2004**, *468*, 205–216.

(98)   Di Carlo, G.; Izzo, A. A. Cannabinoids for Gastrointestinal Diseases: Potential Therapeutic Applications. *Expert Opin. Investig. Drugs* **2003**, *12*, 39–49.

(99)   Tramer, M. R.; Carroll, D.; Campbell, F. A.; Reynolds, D. J. M.; Moore, R. A.; McQuay, H. J. Cannabinoids for Control of Chemotherapy Induced Nausea and Vomiting: Quantitative Systematic Review. *Br. Med. J.* **2001**, *323*, 16–21.

(100)   Sospedra, M.; Martin, R. Immunology of Multiple Sclerosis. *Annu. Rev. Immunol.* **2005**, *23*, 683–747.

(101)   Compston, A.; Coles, A. Multiple Sclerosis (vol 359, Pg 1221, 2002). *Lancet* **2002**, *360*, 648.

(102)   Killestein, J.; Polman, C. H. Current Trials in Multiple Sclerosis: Established Evidence and Future Hopes. *Curr. Opin. Neurol.* **2005**, *18*, 253–260.

(103) Baker, D.; Pryce, G.; Croxford, J. L.; Brown, P.; Pertwee, R. G.; Huffman, J. W.; Layward, L. Cannabinoids Control Spasticity and Tremor in a Multiple Sclerosis Model. *Nature* **2000**, *404*, 84–87.

(104) Eljaschewitsch, E.; Witting, A.; Mawrin, C.; Lee, T.; Schmidt, P. M.; Wolf, S.; Hoertnagl, H.; Raine, C. S.; Schneider-Stock, R.; Nitsch, R.; et al. The Endocannabinoid Anandamide Protects Neurons during CNS Inflammation by Induction of MKP-1 in Microglial Cells. *Neuron* **2006**, *49*, 67–79.

(105) Zajicek, J.; Fox, P.; Sanders, H.; Wright, D.; Vickery, J.; Nunn, A.; Thompson, A.; Grp, U. M. R. Cannabinoids for Treatment of Spasticity and Other Symptoms Related to Multiple Sclerosis (CAMS Study): Multicentre Randomised Placebo-Controlled Trial. *Lancet* **2003**, *362*, 1517–1526.

(106) Zajicek, J.; Fox, R.; Sanders, H.; Wright, D.; Vickery, J.; Nunn, A.; Thompson, A.; Grp, U. M. R. The Cannabinoids in MS Study - Final Results from 12 Months Follow-Up. *Mult. Scler.* **2004**, *10*, S115–S115.

(107) Iskedjian, M.; Bereza, B.; Gordon, A.; Piwko, C.; Einarson, T. R. Meta-Analysis of Cannabis Based Treatments for Neuropathic and Multiple Sclerosis-Related Pain. *Curr. Med. Res. Opin.* **2007**, *23*, 17–24.

(108) Pertwee, R. G. Emerging Strategies for Exploiting Cannabinoid Receptor Agonists as Medicines. *Br. J. Pharmacol.* **2009**, *156*, 397–411.

(109) Dziadulewicz, E. K.; Bevan, S. J.; Brain, C. T.; Coote, P. R.; Culshaw, A. J.; Davis, A. J.; Edwards, L. J.; Fisher, A. J.; Fox, A. J.; Gentry, C.; et al. Naphthalen-1-Yl-(4-Pentyloxynaphthalen-1-Yl)methanone: A Potent, Orally Bioavailable Human CB1/CB2 Dual Agonist with Antihyperalgesic Properties and Restricted Central Nervous System Penetration. *J. Med. Chem.* **2007**, *50*, 3851–3856.

(110) Guindon, J.; Hohmann, A. G. Cannabinoid CB2 Receptors: A Therapeutic Target for the Treatment of Inflammatory and Neuropathic Pain. *Br. J. Pharmacol.* **2008**, *153*, 319–334.

(111) Whiteside, G. T.; Lee, G. P.; Valenzano, K. J. The Role of the Cannabinoid CB2 Receptor in Pain Transmission and Therapeutic Potential of Small Molecule CB2 Receptor Agonists. *Curr. Med. Chem.* **2007**, *14*, 917–936.

(112) Stern, E.; Muccioli, G. G.; Millet, R.; Goossens, J.-F.; Farce, A.; Chavatte, P.; Poupaert, J. H.; Lambert, D. M.; Depreux, P.; Hénichart, J.-P. Novel 4-Oxo-1,4-Dihydroquinoline-3-Carboxamide Derivatives as New CB2 Cannabinoid Receptors Agonists: Synthesis, Pharmacological Properties and Molecular Modeling. *J. Med. Chem.* **2006**, *49*, 70–79.

(113) Manera, C.; Cascio, M. G.; Benetti, V.; Allarà, M.; Tuccinardi, T.; Martinelli, A.; Saccomanni, G.; Vivoli, E.; Ghelardini, C.; Di Marzo, V.; et al. New 1,8-Naphthyridine and Quinoline Derivatives as CB2 Selective Agonists. *Bioorg. Med. Chem. Lett.* **2007**, *17*, 6505–6510.

(114)   Manera, C.; Benetti, V.; Castelli, M. P.; Cavallini, T.; Lazzarotti, S.; Pibiri, F.; Saccomanni, G.; Tuccinardi, T.; Vannacci, A.; Martinelli, A.; et al. Design, Synthesis, and Biological Evaluation of New 1,8-Naphthyridin-4(1H)-on-3-Carboxamide and Quinolin-4(1H)-on-3-Carboxamide Derivatives as CB2 Selective Agonists. *J. Med. Chem.* **2006**, *49*, 5947–5957.

(115)   Pasquini, S.; Botta, L.; Semeraro, T.; Mugnaini, C.; Ligresti, A.; Palazzo, E.; Maione, S.; Di Marzo, V.; Corelli, F. Investigations on the 4-Quinolone-3-Carboxylic Acid Motif. 2. Synthesis and Structure-Activity Relationship of Potent and Selective Cannabinoid-2 Receptor Agonists Endowed with Analgesic Activity in Vivo. *J. Med. Chem.* **2008**, *51*, 5075–5084.

(116)   Baraldi, P. G.; Saponaro, G.; Moorman, A. R.; Romagnoli, R.; Preti, D.; Baraldi, S.; Ruggiero, E.; Varani, K.; Targa, M.; Vincenzi, F.; et al. 7-Oxo-[1,4]oxazino[2,3,4-Ij]quinoline-6-Carboxamides as Selective CB(2) Cannabinoid Receptor Ligands: Structural Investigations around a Novel Class of Full Agonists. *J. Med. Chem.* **2012**, *55*, 6608–6623.

(117)   Aghazadeh Tabrizi, M.; Baraldi, P. G.; Saponaro, G.; Moorman, A. R.; Romagnoli, R.; Preti, D.; Baraldi, S.; Corciulo, C.; Vincenzi, F.; Borea, P. A.; et al. Design, Synthesis, and Pharmacological Properties of New Heteroarylpyridine/heteroarylpyrimidine Derivatives as CB(2) Cannabinoid Receptor Partial Agonists. *J. Med. Chem.* **2013**, *56*, 1098–1112.

(118)   Giblin, G. M. P.; O'Shaughnessy, C. T.; Naylor, A.; Mitchell, W. L.; Eatherton, A. J.; Slingsby, B. P.; Rawlings, D. A.; Goldsmith, P.; Brown, A. J.; Haslam, C. P.; et al. Discovery of 2-[(2,4-Dichlorophenyl)amino]-N-[(tetrahydro- 2H-Pyran-4-Yl)methyl]-4-(trifluoromethyl)- 5-Pyrimidinecarboxamide, a Selective CB2 Receptor Agonist for the Treatment of Inflammatory Pain. *J. Med. Chem.* **2007**, *50*, 2597–2600.

(119)   Appendino, G.; Cascio, M. G.; Bacchiega, S.; Moriello, A. S.; Minassi, A.; Thomas, A.; Ross, R.; Pertwee, R.; De Petrocellis, L.; Di Marzo, V. First "Hybrid" Ligands of Vanilloid TRPV1 and Cannabinoid CB2 Receptors and Non-Polyunsaturated Fatty Acid-Derived CB2-Selective Ligands. *Febs Lett.* **2006**, *580*, 568–574.

(120)   Pertwee, R. G. The Diverse CB1 and CB2 Receptor Pharmacology of Three Plant Cannabinoids: Delta(9)-Tetrahydrocannabinol, Cannabidiol and Delta(9)-Tetrahydrocannabivarin. *Br. J. Pharmacol.* **2008**, *153*, 199–215.

(121)   Sun, Y.; Alexander, S. P. H.; Garle, M. J.; Gibson, C. L.; Hewitt, K.; Murphy, S. P.; Kendall, D. A.; Bennett, A. J. Cannabinoid Activation of PPAR Alpha; a Novel Neuroprotective Mechanism. *Br. J. Pharmacol.* **2007**, *152*, 734–743.

(122)   Bernstein, F. C.; Koetzle, T. F.; Williams, G. J. B.; Meyer, E. F.; Brice, M. D.; Rodgers, J. R.; Kennard, O.; Shimanouchi, T.; Tasumi, M. Protein Data Bank - Computer-Based Archival File for Macromolecular Structures. *J. Mol. Biol.* **1977**, *112*, 535–542.

(123)   Cavasotto, C. N.; Phatak, S. S. Homology Modeling in Drug Discovery: Current Trends and Applications. *Drug Discov. Today* **2009**, *14*, 676–683.

(124)   Venselaar, H.; Joosten, R. P.; Vroling, B.; Baakman, C. A. B.; Hekkelman, M. L.; Krieger, E.; Vriend, G. Homology Modelling and Spectroscopy, a Never-Ending Love Story. *Eur. Biophys. J.* **2010**, *39*, 551–563.

(125)   Altschul, S. F.; Gish, W.; Miller, W.; Myers, E. W.; Lipman, D. J. Basic Local Alignment Search Tool. *J. Mol. Biol.* **1990**, *215*, 403–410.

(126)   Altschul, S. F.; Madden, T. L.; Schäffer, A. A.; Zhang, J.; Zhang, Z.; Miller, W.; Lipman, D. J. Gapped BLAST and PSI-BLAST: A New Generation of Protein Database Search Programs. *Nucleic Acids Res.* **1997**, *25*, 3389–3402.

(127)   Larsson, P.; Wallner, B.; Lindahl, E.; Elofsson, A. Using Multiple Templates to Improve Quality of Homology Models in Automated Homology Modeling. *Protein Sci.* **2008**, *17*, 990–1002.

(128)   Laskowski, R. A.; Macarthur, M. W.; Moss, D. S.; Thornton, J. M. PROCHECK - A Program to Check the Stereochemical Quality of Protein Structures. *J. Appl. Crystallogr.* **1993**, *26*, 283–291.

(129)   Ramachandran, G. N.; Ramakrishnan, C.; Sasisekharan, V. Stereochemistry of Polypeptide Chain Configurations. *J. Mol. Biol.* **1963**, *7*, 95–99.

(130)   Krieger, E.; Darden, T.; Nabuurs, S. B.; Finkelstein, A.; Vriend, G. Making Optimal Use of Empirical Energy Functions: Force-Field Parameterization in Crystal Space. *Proteins* **2004**, *57*, 678–683.

(131)   Misura, K. M. S.; Chivian, D.; Rohl, C. A.; Kim, D. E.; Baker, D. Physically Realistic Homology Models Built with ROSETTA Can Be More Accurate than Their Templates. *Proc. Natl. Acad. Sci. U. S. A.* **2006**, *103*, 5361–5366.

(132)   Halgren, T. a; Murphy, R. B.; Friesner, R. a; Beard, H. S.; Frye, L. L.; Pollard, W. T.; Banks, J. L. Glide: A New Approach for Rapid, Accurate Docking and Scoring. 2. Enrichment Factors in Database Screening. *J. Med. Chem.* **2004**, *47*, 1750–1759.

(133)   Triballeau, N.; Acher, F.; Brabet, I.; Pin, J.-P.; Bertrand, H.-O. Virtual Screening Workflow Development Guided by the "Receiver Operating Characteristic" Curve Approach. Application to High-Throughput Docking on Metabotropic Glutamate Receptor Subtype 4. *J. Med. Chem.* **2005**, *48*, 2534–2547.

(134)   Henzler-Wildman, K.; Kern, D. Dynamic Personalities of Proteins. *Nature* **2007**, *450*, 964–972.

(135)   Leach, A. R. *Molecular Modelling: Principles and Applications*; Pearson Education. **2001**.

(136)   Ponder, J. W.; Case, D. a. Force Fields for Protein Simulations. *Adv. Protein Chem.* **2003**, *66*, 27–85.

(137)   Durrant, J. D.; McCammon, J. A. Molecular Dynamics Simulations and Drug Discovery. *BMC Biol.* **2011**, *9*, 71.

(138) Cornell, W. D.; Cieplak, P.; Bayly, C. I.; Gould, I. R.; Merz, K. M.; Ferguson, D. M.; Spellmeyer, D. C.; Fox, T.; Caldwell, J. W.; Kollman, P. A. A Second Generation Force Field for the Simulation of Proteins, Nucleic Acids, and Organic Molecules. *J. Am. Chem. Soc.* **1995**, *117*, 5179–5197.

(139) Brooks, B. R.; Bruccoleri, R. E.; Olafson, B. D.; States, D. J.; Swaminathan, S.; Karplus, M. CHARMM: A Program for Macromolecular Energy, Minimization, and Dynamics Calculations. *J. Comput. Chem.* **1983**, *4*, 187–217.

(140) Oostenbrink, C.; Villa, A.; Mark, A. E.; Van Gunsteren, W. F. A Biomolecular Force Field Based on the Free Enthalpy of Hydration and Solvation: The GROMOS Force-Field Parameter Sets 53A5 and 53A6. *J. Comput. Chem.* **2004**, *25*, 1656–1676.

(141) Shaw, D. E.; Deneroff, M. M.; Dror, R. O.; Kuskin, J. S.; Larson, R. H.; Salmon, J. K.; Young, C.; Batson, B.; Bowers, K. J.; Chao, J. C.; et al. Anton, a Special-Purpose Machine for Molecular Dynamics Simulation. *Commun. ACM* **2008**, *51*, 91–97.

(142) Yuriev, E.; Agostino, M.; Ramsland, P. A. Challenges and Advances in Computational Docking: 2009 in Review. *J. Mol. Recognit. JMR* **2011**, *24*, 149–164.

(143) Plewczynski, D.; Łaźniewski, M.; Augustyniak, R.; Ginalski, K. Can We Trust Docking Results? Evaluation of Seven Commonly Used Programs on PDBbind Database. *J. Comput. Chem.* **2011**, *32*, 742–755.

(144) Cheng, T.; Li, X.; Li, Y.; Liu, Z.; Wang, R. Comparative Assessment of Scoring Functions on a Diverse Test Set. *J. Chem. Inf. Model.* **2009**, *49*, 1079–1093.

(145) Wang, R. X.; Lu, Y. P.; Wang, S. M. Comparative Evaluation of 11 Scoring Functions for Molecular Docking. *J. Med. Chem.* **2003**, *46*, 2287–2303.

(146) Ferrara, P.; Gohlke, H.; Price, D. J.; Klebe, G.; Brooks, C. L. Assessing Scoring Functions for Protein-Ligand Interactions. *J. Med. Chem.* **2004**, *47*, 3032–3047.

(147) Wang, R. X.; Lu, Y. P.; Fang, X. L.; Wang, S. M. An Extensive Test of 14 Scoring Functions Using the PDBbind Refined Set of 800 Protein-Ligand Complexes. *J. Chem. Inf. Comput. Sci.* **2004**, *44*, 2114–2125.

(148) Warren, G. L.; Andrews, C. W.; Capelli, A.-M.; Clarke, B.; LaLonde, J.; Lambert, M. H.; Lindvall, M.; Nevins, N.; Semus, S. F.; Senger, S.; et al. A Critical Assessment of Docking Programs and Scoring Functions. *J. Med. Chem.* **2006**, *49*, 5912–5931.

(149) Kufareva, I.; Rueda, M.; Katritch, V.; Stevens, R. C.; Abagyan, R. Status of GPCR Modeling and Docking as Reflected by Community-Wide GPCR Dock 2010 Assessment. *Structure* **2011**, *19*, 1108–1126.

(150) Bramblett, R. D.; Panu, A. M.; Ballesteros, J. A.; Reggio, P. H. Construction of a 3D Model of the Cannabinoid CB1 Receptor: Determination of Helix Ends and Helix Orientation. *Life Sci.* **1995**, *56*, 1971–1982.

(151)   Mahmoudian, M. The Cannabinoid Receptor: Computer-Aided Molecular Modeling and Docking of Ligand. *J. Mol. Graph. Model.* **1997**, *15*, 149–153.

(152)   Xie, X. Q.; Chen, J. Z.; Billings, E. M. 3D Structural Model of the G-Protein-Coupled Cannabinoid CB2 Receptor. *Proteins-Structure Funct. Genet.* **2003**, *53*, 307–319.

(153)   Shim, J.-Y.; Welsh, W. J.; Howlett, A. C. Homology Model of the CB1 Cannabinoid Receptor: Sites Critical for Nonclassical Cannabinoid Agonist Interaction. *Biopolymers* **2003**, *71*, 169–189.

(154)   Singh, R.; Hurst, D. P.; Barnett-Norris, J.; Lynch, D. L.; Reggio, P. H.; Guarnieri, F. Activation of the Cannabinoid CB1 Receptor May Involve a W6.48/F3.36 Rotamer Toggle Switch. *J. Pept. Res.* **2002**, *60*, 357–370.

(155)   Latek, D.; Kolinski, M.; Ghoshdastider, U.; Debinski, A.; Bombolewski, R.; Plazinska, A.; Jozwiak, K.; Filipek, S. Modeling of Ligand Binding to G Protein Coupled Receptors: Cannabinoid CB(1), CB(2) and Adrenergic beta(2)AR. *J. Mol. Model.* **2011**, *17*, 2353–2366.

(156)   Tuccinardi, T.; Ferrarini, P. L.; Manera, C.; Ortore, G.; Saccomanni, G.; Martinelli, A. Cannabinoid CB2/CB1 Selectivity. Receptor Modeling and Automated Docking Analysis. *J. Med. Chem.* **2006**, *49*, 984–994.

(157)   Durdagi, S.; Reis, H.; Papadopoulos, M. G.; Mavromoustakos, T. Comparative Molecular Dynamics Simulations of the Potent Synthetic Classical Cannabinoid Ligand AMG3 in Solution and at Binding Site of the CB1 and CB2 Receptors. *Bioorg. Med. Chem.* **2008**, *16*, 7377–7387.

(158)   Durdagi, S.; Papadopoulos, M. G.; Zoumpoulakis, P. G.; Koukoulitsa, C.; Mavromoustakos, T. A Computational Study on Cannabinoid Receptors and Potent Bioactive Cannabinoid Ligands: Homology Modeling, Docking, de Novo Drug Design and Molecular Dynamics Analysis. *Mol. Divers.* **2010**, *14*, 257–276.

(159)   Renault, N.; Laurent, X.; Farce, A.; El Bakali, J.; Mansouri, R.; Gervois, P.; Millet, R.; Desreumaux, P.; Furman, C.; Chavatte, P. Virtual Screening of CB(2) Receptor Agonists from Bayesian Network and High-Throughput Docking: Structural Insights into Agonist-Modulated GPCR Features. *Chem. Biol. Drug Des.* **2013**, *81*, 442–454.

(160)   Shim, J.-Y.; Rudd, J.; Ding, T. T. Distinct Second Extracellular Loop Structures of the Brain Cannabinoid CB(1) Receptor: Implication in Ligand Binding and Receptor Function. *Proteins-Structure Funct. Bioinforma.* **2011**, *79*, 581–597.

(161)   Hurst, D. P.; Grossfield, A.; Lynch, D. L.; Feller, S.; Romo, T. D.; Gawrisch, K.; Pitman, M. C.; Reggio, P. H. A Lipid Pathway for Ligand Binding Is Necessary for a Cannabinoid G Protein-Coupled Receptor. *J. Biol. Chem.* **2010**, *285*, 17954–17964.

(162)   Cichero, E.; Ligresti, A.; Allarà, M.; di Marzo, V.; Lazzati, Z.; D'Ursi, P.; Marabotti, A.; Milanesi, L.; Spallarossa, A.; Ranise, A.; et al. Homology Modeling in Tandem with 3D-QSAR Analyses: A Computational Approach to Depict the Agonist Binding Site of the Human CB2 Receptor. *Eur. J. Med. Chem.* **2011**, *46*, 4489–4505.

(163) Ai, R.; Chang, C. A. Ligand-Specific Homology Modeling of Human Cannabinoid (CB1) Receptor. *J. Mol. Graph. Model.* **2012**, *38*, 155–164.

(164) Tao, Q.; McAllister, S. D.; Andreassi, J.; Nowell, K. W.; Cabral, G. A.; Hurst, D. P.; Bachtel, K.; Ekman, M. C.; Reggio, P. H.; Abood, M. E. Role of a Conserved Lysine Residue in the Peripheral Cannabinoid Receptor (CB2): Evidence for Subtype Specificity. *Mol. Pharmacol.* **1999**, *55*, 605–613.

(165) Song, Z. H.; Slowey, C. A.; Hurst, D. P.; Reggio, P. H. The Difference between the CB1 and CB2 Cannabinoid Receptors at Position 5.46 Is Crucial for the Selectivity of WIN55212-2 for CB2. *Mol. Pharmacol.* **1999**, *56*, 834–840.

(166) McAllister, S. D.; Tao, Q.; Barnett-Norris, J.; Buehner, K.; Hurst, D. P.; Guarnieri, F.; Reggio, P. H.; Harmon, K. W. N.; Cabral, G. A.; Abood, M. E. A Critical Role for a Tyrosine Residue in the Cannabinoid Receptors for Ligand Recognition. *Biochem. Pharmacol.* **2002**, *63*, 2121–2136.

(167) McAllister, S. D.; Rizvi, G.; Anavi-Goffer, S.; Hurst, D. P.; Barnett-Norris, J.; Lynch, D. L.; Reggio, P. H.; Abood, M. E. An Aromatic Microdomain at the Cannabinoid CB1 Receptor Constitutes an Agonist/inverse Agonist Binding Region. *J. Med. Chem.* **2003**, *46*, 5139–5152.

(168) McAllister, S. D.; Hurst, D. P.; Barnett-Norris, J.; Lynch, D.; Reggio, P. H.; Abood, M. E. Structural Mimicry in Class A G Protein-Coupled Receptor Rotamer Toggle Switches - The Importance of the F3.36(201)/W6.48(357) Interaction in Cannabinoid CB1 Receptor Activation. *J. Biol. Chem.* **2004**, *279*, 48024–48037.

(169) Kapur, A.; Hurst, D. P.; Fleischer, D.; Whitnell, R.; Thakur, G. A.; Makriyannis, A.; Reggio, P. H.; Abood, M. E. Mutation Studies of Ser7.39 and Ser2.60 in the Human CB(1) Cannabinoid Receptor: Evidence for a Serine-Induced Bend in CB(1) Transmembrane Helix 7. *Mol. Pharmacol.* **2007**, *71*, 1512–1524.

(170) Gouldson, P.; Calandra, B.; Legoux, P.; Kerneis, A.; Rinaldi-Carmona, M.; Barth, F.; Le Fur, G.; Ferrara, P.; Shire, D. Mutational Analysis and Molecular Modelling of the Antagonist SR 144528 Binding Site on the Human Cannabinoid CB2 Receptor. *Eur. J. Pharmacol.* **2000**, *401*, 17–25.

(171) Zhang, Y. X.; Xie, Z. J.; Wang, L. R.; Schreiter, B.; Lazo, J. S.; Gertsch, J.; Xie, X. Q. Mutagenesis and Computer Modeling Studies of a GPCR Conserved Residue W5.43(194) in Ligand Recognition and Signal Transduction for CB2 Receptor. *Int. Immunopharmacol.* **2011**, *11*, 1303–1310.

(172) Montero, C.; Campillo, N. E.; Goya, P.; Páez, J. A. Homology Models of the Cannabinoid CB1 and CB2 Receptors. A Docking Analysis Study. *Eur. J. Med. Chem.* **2005**, *40*, 75–83.

(173) Sitkoff, D. F.; Lee, N.; Ellsworth, B. A.; Huang, Q.; Kang, L.; Baska, R.; Huang, Y.; Sun, C.; Pendri, A.; Malley, M. F.; et al. Cannabinoid CB(1) Receptor Ligand Binding and Function Examined through Mutagenesis Studies of F200 and S383. *Eur. J. Pharmacol.* **2011**, *651*, 9–17.

(174) Backes, J. M.; Gibson, C. A.; Ruisinger, J. F.; Moriarty, P. M. Fibrates: What Have We Learned in the Past 40 Years? *Pharmacotherapy* **2007**, *27*, 412–424.

(175) Staels, B.; Dallongeville, J.; Auwerx, J.; Schoonjans, K.; Leitersdorf, E.; Fruchart, J.-C. Mechanism of Action of Fibrates on Lipid and Lipoprotein Metabolism. *Circulation* **1998**, *98*, 2088–2093.

(176) Fazio, S.; Linton, M. F. The Role of Fibrates in Managing Hyperlipidemia: Mechanisms of Action and Clinical Efficacy. *Curr. Atheroscler. Rep.* **2004**, *6*, 148–157.

(177) Xu, H. E.; Lambert, M. H.; Montana, V. G.; Plunket, K. D.; Moore, L. B.; Collins, J. L.; Oplinger, J. A.; Kliewer, S. A.; Gampe, R. T.; McKee, D. D.; et al. Structural Determinants of Ligand Binding Selectivity between the Peroxisome Proliferator-Activated Receptors. *Proc. Natl. Acad. Sci. U. S. A.* **2001**, *98*, 13919–13924.

(178) McGuinness, D.; Malikzay, A.; Visconti, R.; Lin, K.; Bayne, M.; Monsma, F.; Lunn, C. A. Characterizing Cannabinoid CB2 Receptor Ligands Using DiscoveRx PathHunter Beta-Arrestin Assay. *J. Biomol. Screen. Off. J. Soc. Biomol. Screen.* **2009**, *14*, 49–58.

(179) Spencer, S. Novel Fenofibrate Derivatives as Cannabinoid Receptor Ligands. Unpublished doctoral dissertation. University of Nottingham, UK, **2011**.

(180) Apweiler, R.; Martin, M. J.; O'Donovan, C.; Magrane, M.; Alam-Faruque, Y.; Antunes, R.; Barrell, D.; Bely, B.; Bingley, M.; Binns, D.; et al. Ongoing and Future Developments at the Universal Protein Resource. *Nucleic Acids Res.* **2011**, *39*, 214–219.

(181) Rice, P.; Longden, I.; Bleasby, A. EMBOSS: The European Molecular Biology Open Software Suite. *Trends Genet.* **2000**, *16*, 276–277.

(182) Larkin, M. A.; Blackshields, G.; Brown, N. P.; Chenna, R.; McGettigan, P. A.; McWilliam, H.; Valentin, F.; Wallace, I. M.; Wilm, A.; Lopez, R. Clustal W and Clustal X Version 2.0. *Bioinformatics* **2007**, *23*, 2947–2948.

(183) Waterhouse, A. M.; Procter, J. B.; Martin, D. M. A.; Clamp, M.; Barton, G. J. Jalview Version 2-a Multiple Sequence Alignment Editor and Analysis Workbench. *Bioinformatics* **2009**, *25*, 1189–1191.

(184) Fay, J. F.; Dunham, T. D.; Farrens, D. L. Cysteine Residues in the Human Cannabinoid Receptor: Only C257 and C264 Are Required for a Functional Receptor, and Steric Bulk at C386 Impairs Antagonist SR141716A Binding. *Biochemistry* **2005**, *44*, 8757–8769.

(185) Sali, A.; Blundell, T. L. Comparative Protein Modeling by Satisfaction of Spatial Restraints. *J. Mol. Biol.* **1993**, *234*, 779–815.

(186) Morris, A. L.; Macarthur, M. W.; Hutchinson, E. G.; Thornton, J. M. Stereochemical Quality of Protein-Structure Coordinates. *Proteins-Structure Funct. Genet.* **1992**, *12*, 345–364.

(187)	Oostenbrink, C.; Soares, T. A.; Van Der Vegt, N. F. A.; Van Gunsteren, W. F. Validation of the 53A6 GROMOS Force Field. *Eur. Biophys. J.* **2005**, *34*, 273–284.

(188)	Poger, D.; Van Gunsteren, W. F.; Mark, A. E. A New Force Field for Simulating Phosphatidylcholine Bilayers. *J. Comput. Chem.* **2010**, *31*, 1117–1125.

(189)	Berger, O.; Edholm, O.; Jahnig, F. Molecular Dynamics Simulations of a Fluid Bilayer of Dipalmitoylphosphatidylcholine at Full Hydration, Constant Pressure, and Constant Temperature. *Biophys. J.* **1997**, *72*, 2002–2013.

(190)	Kukol, A. Lipid Models for United-Atom Molecular Dynamics Simulations of Proteins. *J. Chem. Theory Comput.* **2009**, *5*, 615–626.

(191)	Poger, D.; Mark, A. E. On the Validation of Molecular Dynamics Simulations of Saturated and Cis-Monounsaturated Phosphatidylcholine Lipid Bilayers: A Comparison with Experiment. *J. Chem. Theory Comput.* **2010**, *6*, 325–336.

(192)	Pabst, G.; Rappolt, M.; Amenitsch, H.; Laggner, P. Structural Information from Multilamellar Liposomes at Full Hydration: Full Q-Range Fitting with High Quality X-Ray Data. *Phys. Rev. E.* **2000**, *62*, 4000.

(193)	Smaby, J. M.; Momsen, M. M.; Brockman, H. L.; Brown, R. E. Phosphatidylcholine Acyl Unsaturation Modulates the Decrease in Interfacial Elasticity Induced by Cholesterol. *Biophys. J.* **1997**, *73*, 1492–1505.

(194)	Kučerka, N.; Tristram-Nagle, S.; Nagle, J. F. Structure of Fully Hydrated Fluid Phase Lipid Bilayers with Monounsaturated Chains. *J. Membr. Biol.* **2006**, *208*, 193–202.

(195)	Hyslop, P. A.; Morel, B.; Sauerheber, R. D. Organization and Interaction of Cholesterol and Phosphatidylcholine in Model Bilayer Membranes. *Biochemistry* **1990**, *29*, 1025–1038.

(196)	Humphrey, W.; Dalke, A.; Schulten, K. VMD: Visual Molecular Dynamics. *J. Mol. Graph.* **1996**, *14*, 33–38.

(197)	Wolf, M. G.; Hoefling, M.; Aponte-Santamaria, C.; Grubmueller, H.; Groenhof, G. G_membed: Efficient Insertion of a Membrane Protein into an Equilibrated Lipid Bilayer with Minimal Perturbation. *J. Comput. Chem.* **2010**, *31*, 2169–2174.

(198)	Allen, W. J.; Lemkul, J. A.; Bevan, D. R. GridMAT-MD: A Grid-Based Membrane Analysis Tool for Use With Molecular Dynamics. *J. Comput. Chem.* **2009**, *30*, 1952–1958.

(199)	Withers, I. M.; Mazanetz, M. P.; Wang, H.; Fischer, P. M.; Laughton, C. A. Active Site Pressurization: A New Tool for Structure-Guided Drug Design and Other Studies of Protein Flexibility. *J. Chem. Inf. Model.* **2008**, *48(7),* 1448-1454.

(200)	Malde, A. K.; Zuo, L.; Breeze, M.; Stroet, M.; Poger, D.; Nair, P. C.; Oostenbrink, C.; Mark, A. E. An Automated Force Field Topology Builder (ATB) and Repository: Version 1.0. *J. Chem. Theory Comput.* **2011**, *7(12),* 4026-4037.

(201) Matthes, D.; de Groot, B. L. Secondary Structure Propensities in Peptide Folding Simulations: A Systematic Comparison of Molecular Mechanics Interaction Schemes. *Biophys. J.* **2009**, *97*, 599–608.

(202) Felder, C. C.; Joyce, K. E.; Briley, E. M.; Mansouri, J.; Mackie, K.; Blond, O.; Lai, Y.; Ma, A. L.; Mitchell, R. L. Comparison of the Pharmacology and Signal-Transduction of the Human Cannabinoid CB1 and CB2 Receptors. *Mol. Pharmacol.* **1995**, *48*, 443–450.

(203) Manera, C.; Cascio, M. G.; Benetti, V.; Allara, M.; Tuccinardi, T.; Martinelli, A.; Saccomanni, G.; Vivoli, E.; Ghelardini, C.; Di Marzo, V.; et al. New 1,8-Naphthyridine and Quinoline Derivatives as CB2 Selective Agonists. *Bioorg. Med. Chem. Lett.* **2007**, *17*, 6505–6510.

(204) Lopez-Rodriguez, M. L.; Viso, A.; Ortega-Gutierrez, S.; Lastres-Becker, I.; Gonzalez, S.; Fernandez-Ruiz, J.; Ramos, J. A. Design, Synthesis and Biological Evaluation of Novel Arachidonic Acid Derivatives as Highly Potent and Selective Endocannabinoid Transporter Inhibitors. *J. Med. Chem.* **2001**, *44*, 4505–4508.

(205) Hillard, C. J.; Manna, S.; Greenberg, M. J.; Dicamelli, R.; Ross, R. A.; Stevenson, L. A.; Murphy, V.; Pertwee, R. G.; Campbell, W. B. Synthesis and Characterization of Potent and Selective Agonists of the Neuronal Cannabinoid Receptor (CB1). *J. Pharmacol. Exp. Ther.* **1999**, *289*, 1427–1433.

(206) Di Marzo, V.; Bisogno, T.; De Petrocellis, L.; Brandi, I.; Jefferson, R. G.; Winckler, R. L.; Davis, J. B.; Dasse, O.; Mahadevan, A.; Razdan, R. K.; et al. Highly Selective CB1 Cannabinoid Receptor Ligands and Novel CB1/VR1 Vanilloid Receptor "Hybrid" Ligands. *Biochem. Biophys. Res. Commun.* **2001**, *281*, 444–451.

(207) Showalter, V. M.; Compton, D. R.; Martin, B. R.; Abood, M. E. Evaluation of Binding in a Transfected Cell Line Expressing a Peripheral Cannabinoid Receptor (CB2): Identification of Cannabinoid Receptor Subtype Selective Ligands. *J. Pharmacol. Exp. Ther.* **1996**, *278*, 989–999.

(208) Iwamura, H.; Suzuki, H.; Ueda, Y.; Kaya, T.; Inaba, T. In Vitro and in Vivo Pharmacological Characterization of JTE907, a Novel Selective Ligand for Cannabinoid CB2 Receptor. *J. Pharmacol. Exp. Ther.* **2001**, *296*, 420–425.

(209) Van der Stelt, M.; van Kuik, J. A.; Bari, M.; van Zadelhoff, G.; Leeflang, B. R.; Veldink, G. A.; Finazzi-Agro, A.; Vliegenthart, J. F. G.; Maccarone, M. Oxygenated Metabolites of Anandamide and 2-Arachidonoylglycerol: Conformational Analysis and Interaction with Cannabinoid Receptors, Membrane Transporter, and Fatty Acid Amide Hydrolase. *J. Med. Chem.* **2002**, *45*, 3709–3720.

(210) Appendino, G.; Ligresti, A.; Minassi, A.; Cascio, M. G.; Allara, M.; Taglialatela-Scafati, O.; Pertwee, R. G.; De Petrocellis, L.; Di Marzo, V. Conformationally Constrained Fatty Acid Ethanolamides as Cannabinoid and Vanilloid Receptor Probes. *J. Med. Chem.* **2009**, *52*, 3001–3009.

(211)   Aung, M. M.; Griffin, G.; Huffman, J. W.; Wu, M. J.; Keel, C.; Yang, B.; Showalter, V. M.; Abood, M. E.; Martin, B. R. Influence of the N-1 Alkyl Chain Length of Cannabimimetic Indoles upon CB1 and CB2 Receptor Binding. *Drug Alcohol Depend.* **2000**, *60*, 133–140.

(212)   Ward, A.; Holmes, B. Nabilone - A Preliminary Review of Its Pharmacological Properties and Therapeutic Use. *Drugs* **1985**, *30*, 127–144.

(213)   Jarbe, T. U. C.; DiPatrizio, N. V; Lu, D.; Makriyannis, A. (-)-Adamantyl-Delta(8)-Tetrahydrocannabinol (AM-411), a Selective Cannabinoid CB1 Receptor Agonist: Effects on Open-Field Behaviors and Antagonism by SR-141716 in Rats. *Behav. Pharmacol.* **2004**, *15*, 517–521.

(214)   Mauler, F.; Mittendorf, J.; Horvath, E.; De Vry, J. Characterization of the Diarylether Sulfonylester (-)-(R)-3-(2-Hydroxymethylindanyl-4-Oxy)phenyl-4,4,4-Trifluoro-1-Sulfona Te (BAY 38-7271) as a Potent Cannabinoid Receptor Agonist with Neuroprotective Properties. *J. Pharmacol. Exp. Ther.* **2002**, *302*, 359–368.

(215)   Khanolkar, A. D.; Lu, D.; Ibrahim, M.; Duclos Jr., R. I.; Thakur, G. A.; Malan Jr., T. P.; Porreca, F.; Veerappan, V.; Tian, X.; George, C.; et al. Cannabilactones: A Novel Class of CB2 Selective Agonists with Peripheral Analgesic Activity. *J. Med. Chem.* **2007**, *50*, 6493–6500.

(216)   Ross, R. A.; Brockie, H. C.; Stevenson, L. A.; Murphy, V. L.; Templeton, F.; Makriyannis, A.; Pertwee, R. G. Agonist Inverse Agonist Characterization at CB1 and CB2 Cannabinoid Receptors of L759633, L759656 and AM630. *Br. J. Pharmacol.* **1999**, *126*, 665–672.

(217)   Martin, B. R.; Wiley, J. L.; Beletskaya, I.; Sim-Selley, L. J.; Smith, F. L.; Dewey, W. L.; Cottney, J.; Adams, J.; Baker, J.; Hill, D.; et al. Pharmacological Characterization of Novel Water-Soluble Cannabinoids. *J. Pharmacol. Exp. Ther.* **2006**, *318*, 1230–1239.

(218)   Huffman, J. W.; Liddle, J.; Yu, S.; Aung, M. M.; Abood, M. E.; Wiley, J. L.; Martin, B. R. 3-(1 ’,1 '-Dimethylbutyl)-1-Deoxy-Delta(8)-THC and Related Compounds: Synthesis of Selective Ligands for the CB2 Receptor. *Bioorg. Med. Chem.* **1999**, *7*, 2905–2914.

(219)   Huffman, J. W.; Zengin, G.; Wu, M. J.; Lu, J. Z.; Hynd, G.; Bushell, K.; Thompson, A. L. S.; Bushell, S.; Tartal, C.; Hurst, D. P.; et al. Structure-Activity Relationships for 1-Alkyl-3-(l-Naphthoyl)indoles at the Cannabinoid CB1 and CB2 Receptors: Steric and Electronic Effects of Naphthoyl Substituents. New Highly Selective CB2 Receptor Agonists. *Bioorg. Med. Chem.* **2005**, *13*, 89–112.

(220)   Frost, J. M.; Dart, M. J.; Tietje, K. R.; Garrison, T. R.; Grayson, G. K.; Daza, A. V; El-Kouhen, O. F.; Miller, L. N.; Li, L.; Yao, B. B.; et al. Indol-3-Yl-Tetramethylcyclopropyl Ketones: Effects of Indole Ring Substitution on CB(2) Cannabinoid Receptor Activity. *J. Med. Chem.* **2008**, *51*, 1904–1912.

(221)   Meng, T.; Wang, J.; Peng, H.; Fang, G.; Li, M.; Xiong, B.; Xie, X.; Zhang, Y.; Wang, X.; Shen, J. Discovery of Benzhydrylpiperazine Derivatives as CB(1) Receptor Inverse Agonists via Privileged Structure-Based Approach. *Eur. J. Med. Chem.* **2010**, *45*, 1133–1139.

(222) Rinaldi-Carmona, M.; Barth, F.; Heaulme, M.; Alonso, R.; Shire, D.; Congy, C.; Soubrie, P.; Breliere, J. C.; Lefur, G. Biochemical and Pharmacological Characterization of SR141716A, the First Potent and Selective Brain Cannabinoid Receptor Antagonist. *Life Sci.* **1995**, *56*, 1941–1947.

(223) Rinaldi-Carmona, M.; Barth, F.; Congy, C.; Martinez, S.; Oustric, D.; Perio, A.; Poncelet, M.; Maruani, J.; Arnone, M.; Finance, O.; et al. SR147778 5-(4-Bromophenyl)-1-(2,4-Dichlorophenyl)-4-Ethyl-N-(1-Piperidinyl)-1H-P Yrazole-3-Carboxamide , a New Potent and Selective Antagonist of the CB1 Cannabinoid Receptor: Biochemical and Pharmacological Characterization. *J. Pharmacol. Exp. Ther.* **2004**, *310*, 905–914.

(224) Rinaldi-Carmona, M.; Barth, F.; Millan, J.; Derocq, J. M.; Casellas, P.; Congy, C.; Oustric, D.; Sarran, M.; Bouaboula, M.; Calandra, B.; et al. SR 144528, the First Potent and Selective Antagonist of the CB2 Cannabinoid Receptor. *J. Pharmacol. Exp. Ther.* **1998**, *284*, 644–650.

(225) Lan, R.; Gatley, J.; Lu, Q.; Fan, P.; Fernando, S. R.; Volkow, N. D.; Pertwee, R.; Makriyannis, A. Design and Synthesis of the CB1 Selective Cannabinoid Antagonist AM281: A Potential Human SPECT Ligand. *AAPS PharmSci* **1999**, *1*, 39-45.

(226) Meschler, J. P.; Kraichely, D. M.; Wilken, G. H.; Howlett, A. C. Inverse Agonist Properties of N-(piperidin-1-Yl)-5-(4-Chlorophenyl)-1-(2,4-Dichlorophenyl)-4-Methyl-1H -Pyrazole-3-Carboxamide HCl (SR141716A) and 1-(2-Chlorophenyl)-4-Cyano-5-(4-Methoxypheny-1H-Pyrazole-3-Carboxylic Acid Phenylamide (CP-272871) for the C. *Biochem. Pharmacol.* **2000**, *60*, 1315–1323.

(227) Katoch-Rouse, R.; Pavlova, O. A.; Caulder, T.; Hoffman, A. F.; Mukhin, A. G.; Horti, A. G. Synthesis, Structure-Activity Relationship, and Evaluation of SR141716 Analogues: Development of Central Cannabinoid Receptor Ligands with Lower Lipophilicity. *J. Med. Chem.* **2003**, *46*, 642–645.

(228) Ruiu, S.; Pinna, G. A.; Marchese, G.; Mussinu, J. M.; Saba, P.; Tambaro, S.; Casti, P.; Vargiu, R.; Pani, L. Synthesis and Characterization of NESS 0327: A Novel Putative Antagonist of the CB1 Cannabinoid Receptor. *J. Pharmacol. Exp. Ther.* **2003**, *306*, 363–370.

(229) Stoit, A. R.; Lange, J. H. M.; den Hartog, A. P.; Ronken, E.; Tipker, K.; van Stuivenberg, H. H.; Dijksman, J. A. R.; Wals, H. C.; Kruse, C. G. Design, Synthesis and Biological Activity of Rigid Cannabinoid CB1 Receptor Antagonists. *Chem. Pharm. Bull. (Tokyo).* **2002**, *50*, 1109–1113.

(230) Lange, J. H. M.; Coolen, H.; van Stuivenberg, H. H.; Dijksman, J. A. R.; Herremans, A. H. J.; Ronken, E.; Keizer, H. G.; Tipker, K.; McCreary, A. C.; Veerman, W.; et al. Synthesis, Biological Properties, and Molecular Modeling Investigations of Novel 3,4-Diarylpyrazolines as Potent and Selective CB1 Cannabinoid Receptor Antagonists. *J. Med. Chem.* **2004**, *47*, 627–643.

(231) Lin, L. S.; Lanza, T. J.; Jewell, J. P.; Liu, P.; Shah, S. K.; Qi, H. B.; Tong, X. C.; Wang, J. Y.; Xu, S. Y. S.; Fong, T. M.; et al. Discovery of N- (1S,2S)-3-(4-Chlorophenyl)-2-(3-Cyanophenyl)-1-Methylpropyl -2-Methyl -2-{ 5-(trifluoromethyl)pyridin-2-Yl Oxy}propanamide (MK-0364), a Novel, Acyclic Cannabinoid-1 Receptor Inverse Agonist for the Treatment of Obesity. *J. Med. Chem.* **2006**, *49*, 7584–7587.

(232) Lavey, B. J.; Kozlowski, J. A.; Hipkin, R. W.; Gonsiorek, W.; Lundell, D. J.; Piwinski, J. J.; Narula, S.; Lunn, C. A. Triaryl Bis-Sulfones as a New Class of Cannabinoid CB2 Receptor Inhibitors: Identification of a Lead and Initial SAR Studies. *Bioorg. Med. Chem. Lett.* **2005**, *15*, 783–786.

(233) Rhee, M. H.; Vogel, Z.; Barg, J.; Bayewitch, M.; Levy, R.; Hanus, L.; Breuer, A.; Mechoulam, R. Cannabinol Derivatives: Binding to Cannabinoid Receptors and Inhibition of Adenylylcyclase. *J. Med. Chem.* **1997**, *40*, 3228–3233.

(234) Hanus, L.; Breuer, A.; Tchilibon, S.; Shiloah, S.; Goldenberg, D.; Horowitz, M.; Pertwee, R. G.; Ross, R. A.; Mechoulam, R.; Fride, E. HU-308: A Specific Agonist for CB2, a Peripheral Cannabinoid Receptor. *Proc. Natl. Acad. Sci. U. S. A.* **1999**, *96*, 14228–14233.

(235) Ibrahim, M. M.; Deng, H. F.; Zvonok, A.; Cockayne, D. A.; Kwan, J.; Mata, H. P.; Vanderah, T. W.; Lai, J.; Porreca, F.; Makriyannis, A.; et al. Activation of CB2 Cannabinoid Receptors by AM1241 Inhibits Experimental Neuropathic Pain: Pain Inhibition by Receptors Not Present in the CNS. *Proc. Natl. Acad. Sci. U. S. A.* **2003**, *100*, 10529–10533.

(236) Seltzman, H. H.; Fleming, D. N.; Thomas, B. F.; Gilliam, A. F.; McCallion, D. S.; Pertwee, R. G.; Compton, D. R.; Martin, B. R. Synthesis and Pharmacological Comparison of Dimethylheptyl and Pentyl Analogs of Anandamide. *J. Med. Chem.* **1997**, *40*, 3626-3634.

(237) Kanyonyo, M.; Govaerts, S. J.; Hermans, E.; Poupaert, J. H.; Lambert, D. M. 3-Alkyl-(5,5'-Diphenyl)imidazolidinediones as New Cannabinoid Receptor Ligands. *Bioorg. Med. Chem. Lett.* **1999**, *9*, 2233–2236.

(238) Wiley, J. L.; Jefferson, R. G.; Grier, M. C.; Mahadevan, A.; Razdan, R. K.; Martin, B. R. Novel Pyrazole Cannabinoids: Insights into CB1 Receptor Recognition and Activation. *J. Pharmacol. Exp. Ther.* **2001**, *296*, 1013–1022.

(239) Ross, R. A.; Gibson, T. M.; Stevenson, L. A.; Saha, B.; Crocker, P.; Razdan, R. K.; Pertwee, R. G. Structural Determinants of the Partial Agonist-Inverse Agonist Properties of 6'-Azidohex-2'-Yne-Delta(8)-Tetrahydrocannabinol at Cannabinoid Receptors. *Br. J. Pharmacol.* **1999**, *128*, 735–743.

(240) Kim, R.; Skolnick, J. Assessment of Programs for Ligand Binding Affinity Prediction. *J. Comput. Chem.* **2008**, *29*, 1316–1331.

(241) Pan, Y.; Huang, N.; Cho, S.; MacKerell, A. D. Consideration of Molecular Weight during Compound Selection in Virtual Target-Based Database Screening. *J. Chem. Inf. Comput. Sci.* **2003**, *43*, 267–272.

(242) Song, Z. H.; Bonner, T. I. A Lysine Residue of the Cannabinoid Receptor Is Critical for Receptor Recognition by Several Agonists but Not WIN55212-2. *Mol. Pharmacol.* **1996**, *49*, 891–896.

(243) Shim, J.-Y.; Bertalovitz, A. C.; Kendall, D. A. Identification of Essential Cannabinoid-Binding Domains STRUCTURAL INSIGHTS INTO EARLY DYNAMIC EVENTS IN RECEPTOR ACTIVATION. *J. Biol. Chem.* **2011**, *286*, 33422–33435.

(244) Lin, L. S.; Ha, S.; Ball, R. G.; Tsou, N. N.; Castonguay, L. A.; Doss, G. A.; Fong, T. M.; Shen, C.-P.; Xiao, J. C.; Goulet, M. T.; et al. Conformational Analysis and Receptor Docking of N- (1S,2S)-3-(4-Chlorophenyl)-2-(3-Cyanophenyl)-1-Methylpropyl -2-Methyl -2-{ 5-(trifluoromethyl)pyridin-2-Yl Oxy}propanamide (taranabant, MK-0364), a Novel, Acyclic Cannabinoid-1 Receptor Inverse Agonist. *J. Med. Chem.* **2008**, *51*, 2108–2114.

(245) Picone, R. P.; Khanolkar, A. D.; Xu, W.; Ayotte, L. A.; Thakur, G. A.; Hurst, D. P.; Abood, M. E.; Reggio, P. H.; Fournier, D. J.; Makriyannis, A. (-)-7 '-Isothiocyanato-11-Hydroxy-1 ",1-" Dimethylheptylhexahydrocannabinol (AM841), a High-Affinity Electrophilic Ligand, Interacts Covalently with a Cysteine in Helix Six and Activates the CB1 Cannabinoid Receptor. *Mol. Pharmacol.* **2005**, *68*, 1623–1635.

(246) Ahn, K. H.; Bertalovitz, A. C.; Mierke, D. F.; Kendall, D. A. Dual Role of the Second Extracellular Loop of the Cannabinoid Receptor 1: Ligand Binding and Receptor Localization. *Mol. Pharmacol.* **2009**, *76*, 833–842.

(247) Chin, C. N.; Murphy, J. W.; Huffman, J. W.; Kendall, D. A. The Third Transmembrane Helix of the Cannabinoid Receptor Plays a Role in the Selectivity of Aminoalkylindoles for CB2, Peripheral Cannabinoid Receptor. *J. Pharmacol. Exp. Ther.* **1999**, *291*, 837–844.

(248) Tao, Q.; Abood, M. E. Mutation of a Highly Conserved Aspartate Residue in the Second Transmembrane Domain of the Cannabinoid Receptors, CB1 and CB2, Disrupts G-Protein Coupling. *J. Pharmacol. Exp. Ther.* **1998**, *285*, 651–658.

(249) Poso, A.; Huffman, J. W. Targeting the Cannabinoid CB2 Receptor: Modelling and Structural Determinants of CB2 Selective Ligands. *Br. J. Pharmacol.* **2008**, *153*, 335–346.

(250) Shire, D.; Calandra, B.; Bouaboula, M.; Barth, F.; Rinaldi-Carmona, M.; Casellas, P.; Ferrara, P. Cannabinoid Receptor Interactions with the Antagonists SR 141716A and SR 144528. *Life Sci.* **1999**, *65*, 627–635.

(251) Zhang, R. D.; Hurst, D. P.; Barnett-Norris, J.; Reggio, P. H.; Song, Z. H. Cysteine 2.59(89) in the Second Transmembrane Domain of Human CB2 Receptor Is Accessible within the Ligand Binding Crevice: Evidence for Possible CB2 Deviation from a Rhodopsin Template. *Mol. Pharmacol.* **2005**, *68*, 69–83.

(252) Nebane, N. M.; Hurst, D. P.; Carrasquer, C. A.; Qiao, Z.; Reggio, P. H.; Song, Z.-H. Residues Accessible in the Binding-Site Crevice of Transmembrane Helix 6 of the CB2 Cannabinoid Receptor. *Biochemistry* **2008**, *47*, 13811–13821.

(253) Zhang, R.; Reggio, P. H.; Song, Z. H. Mutagenesis of Aromatic Microdomains at Human CB2 Cannabinoid Receptor, *14ᵗʰ Annual Symposium on Cannbinoid*s, **2004**.

(254)   Rhee, M. H.; Nevo, I.; Bayewitch, M. L.; Zagoory, O.; Vogel, Z. Functional Role of Tryptophan Residues in the Fourth Transmembrane Domain of the CB2 Cannabinoid Receptor. *J. Neurochem.* **2000**, *75*, 2485–2491.

(255)   Shire, D.; Calandra, B.; Delpech, M.; Dumont, X.; Kaghad, M.; LeFur, G.; Caput, D.; Ferrara, P. Structural Features of the Central Cannabinoid CB1 Receptor Involved in the Binding of the Specific CB1 Antagonist SR 141716A. *J. Biol. Chem.* **1996**, *271*, 6941–6946.

(256)   Zhang, Y.; Xie, Z.; Wang, L.; Schreiter, B.; Lazo, J. S.; Gertsch, J.; Xie, X.-Q. Mutagenesis and Computer Modeling Studies of a GPCR Conserved Residue W5.43(194) in Ligand Recognition and Signal Transduction for CB2 Receptor. *Int. Immunopharmacol.* **2011**, *11*, 1303–1310.

(257)   Lange, J. H. M.; Kruse, C. G. Medicinal Chemistry Strategies to CB1 Cannabinoid Receptor Antagonists. *Drug Discov. Today* **2005**, *10*, 693–702.

(258)   Kulkarni, P.; Kadam, A.; Mane, R. Demethylation of Methyl Aryl Ethers Using Pyridine Hydrochloride in Solvent-Free Conditions under Microwave Irradiation. *J. Chem. Res.* **1999**, 1–2.

(259)   Herrero, M. A.; Kremsner, J. M.; Kappe, C. O. Nonthermal Microwave Effects Revisited: On the Importance of Internal Temperature Monitoring and Agitation in Microwave Chemistry. *J. Org. Chem.* **2008**, *73*, 36–47.

(260)   Shi, Y.-J.; Hughes, D. L.; McNamara, J. M. Stereospecific Synthesis of Chiral Tertiary Alkyl-Aryl Ethers via Mitsunobu Reaction with Complete Inversion of Configuration. *Tetrahedron Lett.* **2003**, *44*, 3609–3611.

(261)   Kishorebabu, N.; Periasamy, M. A Simple, Convenient Method for the Synthesis of Maleic Anhydrides from A-Keto Esters and Alkanoic Acid Anhydrides Using the TiCl4/n-Bu3N Reagent System. *Tetrahedron Lett.* **2006**, *47*, 2107–2109.

(262)   Reddy, P. Y.; Kondo, S.; Toru, T.; Ueno, Y. Lewis Acid and Hexamethyldisilazane-Promoted Efficient Synthesis of N -Alkyl- and N -Arylimide Derivatives. *J. Org. Chem.* **1997**, *62*, 2652–2654.

(263)   Paul, S.; Nanda, P.; Gupta, R.; Loupy, A. Zinc Mediated Friedel-Crafts Acylation in Solvent-Free Conditions under Microwave Irradiation. *Synthesis*, **2003**, 2877–2881.

(264)   Sarvari, M. H.; Sharghi, H. Reactions on a Solid Surface. A Simple, Economical and Efficient Friedel-Crafts Acylation Reaction over Zinc Oxide (ZnO) as a New Catalyst. *J. Org. Chem.* **2004**, *69*, 6953–6956.

(265)   Shore, D. M.; Ballie, G. L.; Hurst, D. P.; Navas, F. J.; Seltzman, H. H.; Marcu, J. P.; Abood, M. E.; Ross, R. a.; Reggio, P. H. Allosteric Modulation of a Cannabinoid G Protein-Coupled Receptor: Binding Site Elucidation and Relationship to G Protein Signaling. *J. Biol. Chem.* **2013**, 5828–5845.

(266)   Schmid, N.; Eichenberger, A. P.; Choutko, A.; Riniker, S.; Winger, M.; Mark, A. E.; van Gunsteren, W. F. Definition and Testing of the GROMOS Force-Field Versions 54A7 and 54B7. *Eur. Biophys. J.* **2011**, *40*, 843–856.

(267)   Ng, H. W.; Laughton, C. A.; Doughty, S. W. Molecular Dynamics Simulations of the Adenosine A2a Receptor in POPC and POPE Lipid Bilayers: Effects of Membrane on Protein Behavior. *J. Chem. Inf. Model.* **2014**, *54*, 573–581.

(268)   Ng, H. W.; Laughton, C. A.; Doughty, S. W. Molecular Dynamics Simulations of the Adenosine A2a Receptor: Structural Stability, Sampling, and Convergence. *J. Chem. Inf. Model.* **2013**, *53*, 1168–1178.

(269)   Lazareno, S. Determination of Allosteric Interactions Using Radioligand-Binding Techniques. In *Methods in Molecular Biology*; Willars, G.; Challiss, R., Eds.; Humana Press Inc. **2004**, *259*, 29–46.

(270)   Hess, B.; Kutzner, C.; van der Spoel, D.; Lindahl, E. GROMACS 4: Algorithms for Highly Efficient, Load-Balanced, and Scalable Molecular Simulation. *J. Chem. Theory Comput.* **2008**, *4*, 435–447.

(271)   Berendsen, H. J. C.; Postma, J. P. M.; Van Gunsteren, W. F.; Hermans, J. Interaction Models for Water in Relation to Protein Hydration. *Intermol. forces* **1981**, *331*.

(272)   Darden, T.; York, D.; Pedersen, L. Particle Mesh Ewald - An N.log(N) Method for Ewald Sums in Large Systems. *J. Chem. Phys.* **1993**, *98*, 10089–10092.

(273)   Essmann, U.; Perera, L.; Berkowitz, M. L.; Darden, T.; Lee, H.; Pedersen, L. G. A Smooth Particle Mesh Ewald Method. *J. Chem. Phys.* **1995**, *103*, 8577–8593.

(274)   Hess, B.; Bekker, H.; Berendsen, H. J. C.; Fraaije, J. LINCS: A Linear Constraint Solver for Molecular Simulations. *J. Comput. Chem.* **1997**, *18*, 1463–1472.

(275)   Miyamoto, S.; Kollman, P. A. SETTLE - An Analytical Version of the SHAKE and RATTLE Algorithm for Rigid Water Models. *J. Comput. Chem.* **1992**, *13*, 952–962.

(276)   Bussi, G.; Donadio, D.; Parrinello, M. Canonical Sampling through Velocity Rescaling. *J. Chem. Phys.* **2007**, *126*.

(277)   Parrinello, M.; Rahman, A. Polymorphic Transitions in Single-Crystals - A New Molecular-Dynamics Method. *J. Appl. Phys.* **1981**, *52*, 7182–7190.

(278)   Morris, G. M.; Goodsell, D. S.; Halliday, R. S.; Huey, R.; Hart, W. E.; Belew, R. K.; Olson, A. J. Automated Docking Using a Lamarckian Genetic Algorithm and an Empirical Binding Free Energy Function. *J. Comput. Chem.* **1998**, *19*, 1639–1662.

(279)   Morris, G. M.; Huey, R.; Lindstrom, W.; Sanner, M. F.; Belew, R. K.; Goodsell, D. S.; Olson, A. J. AutoDock4 and AutoDockTools4: Automated Docking with Selective Receptor Flexibility. *J. Comput. Chem.* **2009**, *30*, 2785–2791.

(280)   Milne, G. W. A. Software Review of ChemBioDraw 12.0. *J. Chem. Inf. Model.* **2010**, *50,* 2053.

(281)   Williams, D. B. G.; Lawton, M. Drying of Organic Solvents: Quantitative Evaluation of the Efficiency of Several Desiccants. *J. Org. Chem.* **2010**, *75*, 8351–8354.

(282)   Pence, H. E.; Williams, A. Chemspider: An Online Chemical Information Resource. *Journal of Chemical Education*, **2010**, *87*, 1123–1124.

(283)   Knorr, R.; Trzeciak, A.; Bannwarth, W.; Gillessen, D. New Coupling Reagents in Peptide Chemistry. *Tetrahedron Letters*, **1989**, *30*, 1927–1930.

(284)   Burden, D. Guide to the Homogenization of Biological Samples. *Random Prim.* **2008**, *7*, 1– 14.

(285)   Lowry, O.; Rosebrough, N. J.; Farr, A. L.; Randall, R. J. Protein Measurement with the Folin Phenol Reagent. *J. Biol. Chem.* **1951**, *193*, 265–275.
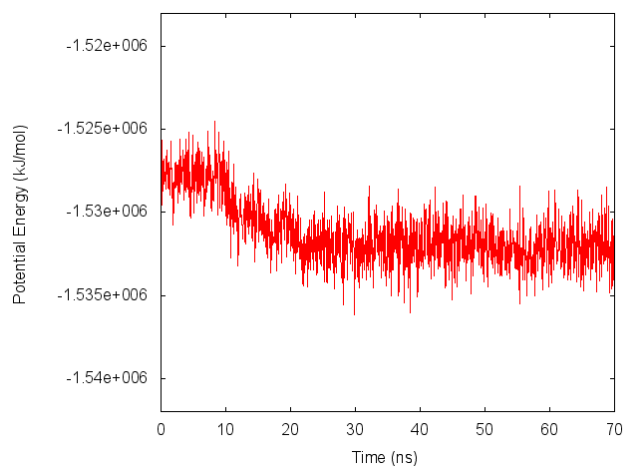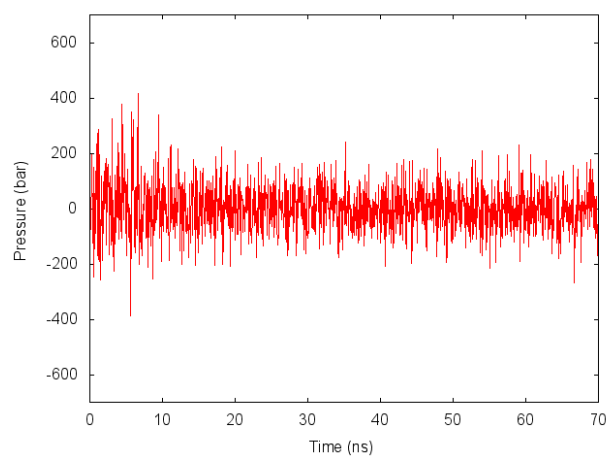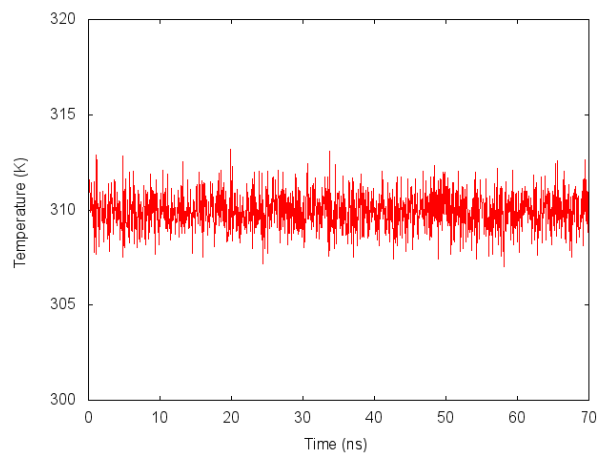
APPENDIX 1

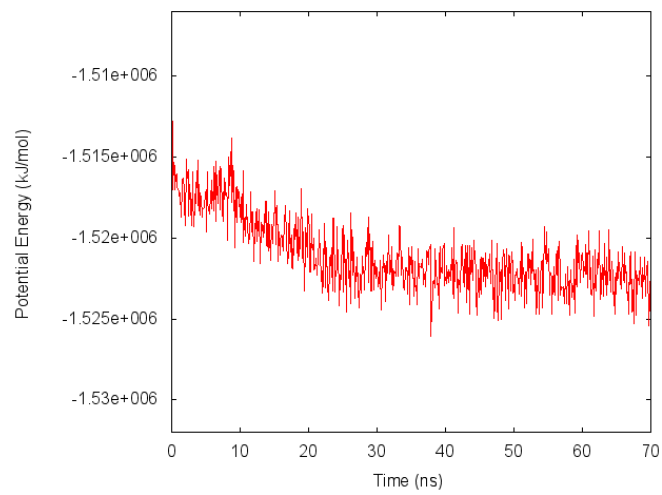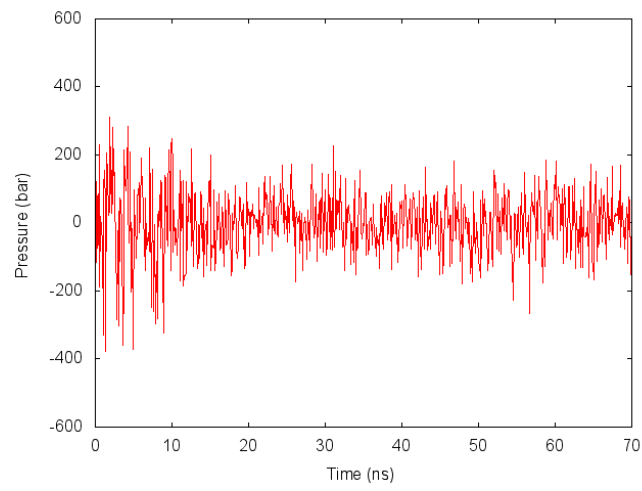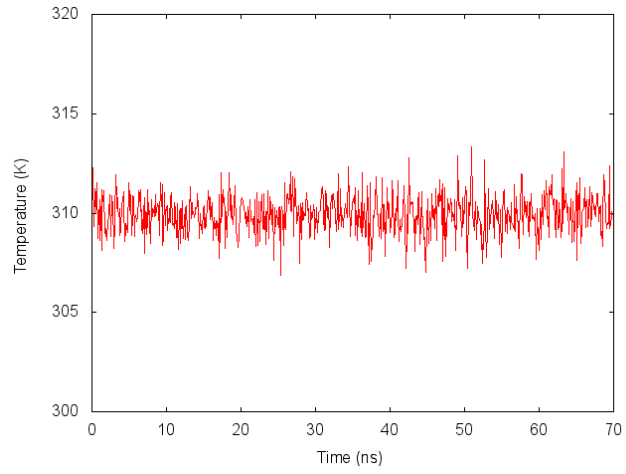**EQUILIBRATION OF THE CANNABINOID RECEPTORS IN A POPC BILAYER**
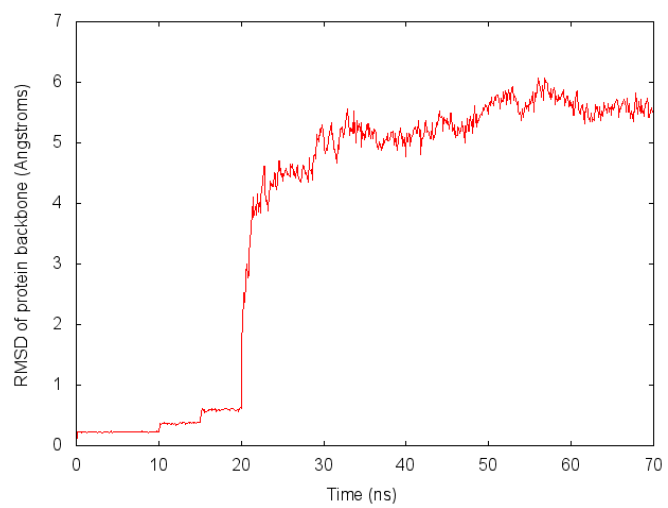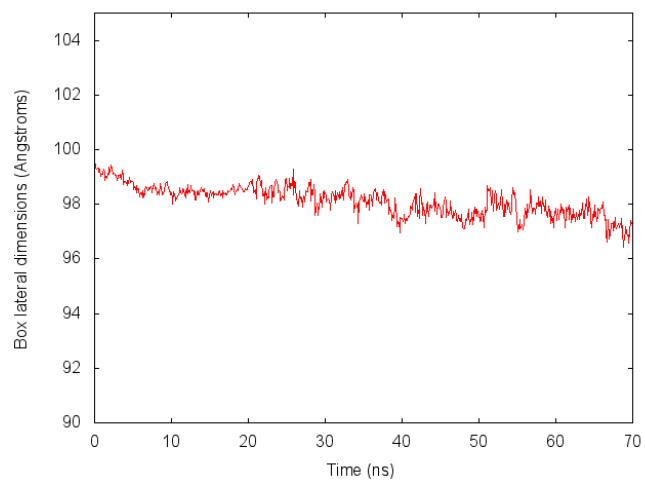
Cannabinoid receptor CB1
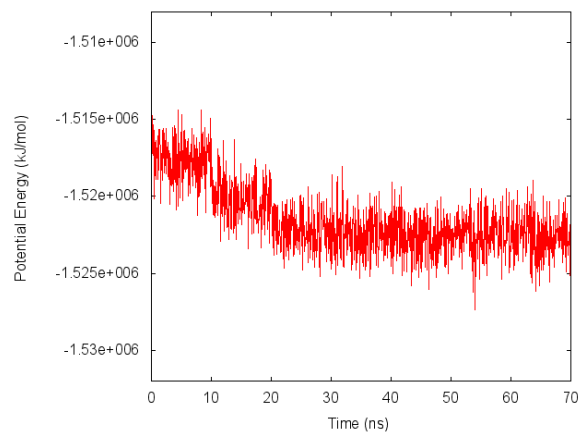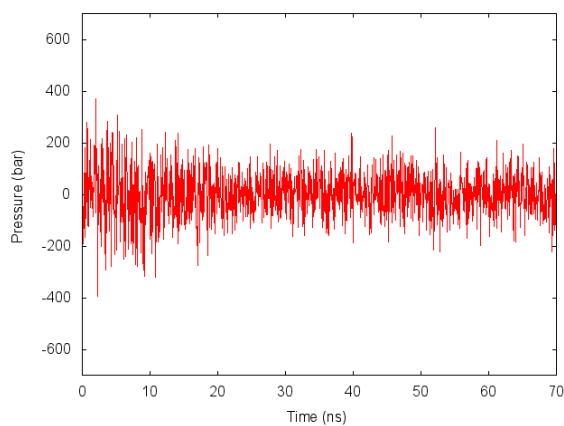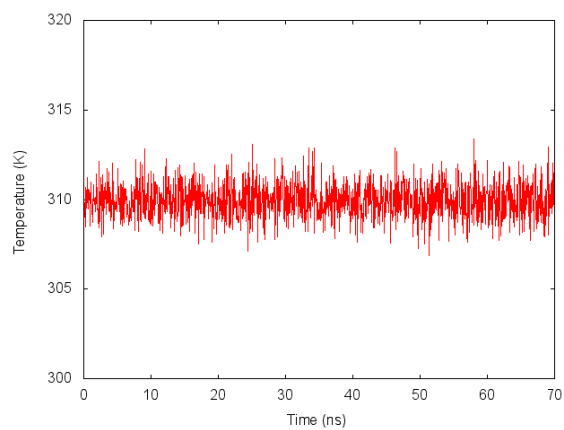
Cannabinoid receptor CB2
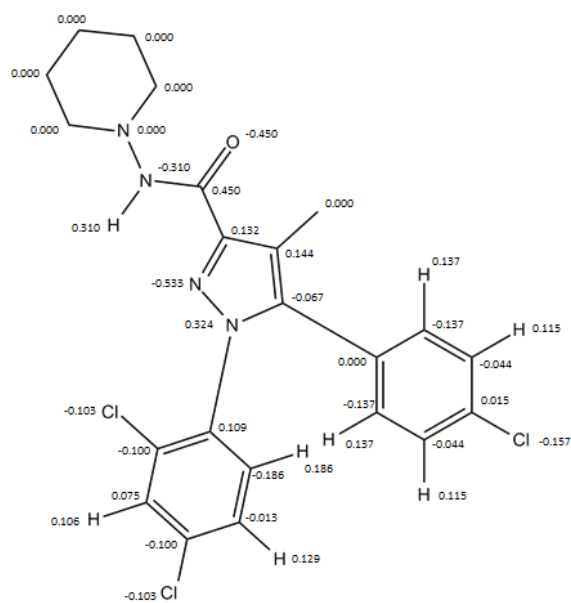
Cannabinoid receptor CB1 with SR141716 bound

Cannabinoid receptor CB1 with SR141716 bound (continued)

APPENDIX II

PARTIAL CHARGES USED IN SR141716 TOPOLOGY

FORCEFIELD: GROMOS 53a6

SR141716

APPENDIX III

LIGANDS USED IN DOCKING EVALUATION

Cannabinoid receptor CB1 agonists

Ligand	Experimental pK_i	Reference
2AG	6.3	(69)
A796260	6.1	(220)
AM1714	6.4	(215)
AM411	8.2	(213)
Anandamide	6.6	(236)
BAY387271	8.7	(214)
Cannabinol	6.5	(207)
CP55940	9.2	(204)
HU210	10.2	(202)
JWH015	6.4	(211)
JWH133	6.2	(219)
O2545	8.9	(217)
THC	7.3	(202)
WIN55212-2	8.7	(207)

Cannabinoid receptor CB1 antagonists

Ligand	Experimental pK_i	Reference
AM281	7.9	(225)
AM630	5.3	(216)
CP272871	8.5	(226)
DML23	7.0	(237)
JTE907	5.6	(208)
LY320135	6.9	(80)
MK0364	9.5	(231)
NESS0327	12.5	(228)
NIDA41020	8.4	(227)
NIDA41109	8.9	(227)
O1270	7.3	(238)
O2050	8.6	(64)
SLV319	8.1	(230)
SR141716	9.1	(221)
SR147778	8.5	(223)

Cannabinoid receptor CB2 agonists

Ligand	Experimental pK_i	Reference
AM 1241	8.5	(235)
AM 1714	9.1	(215)
Anandamide	6.1	(210)
BAY 387271	8.2	(214)
CP 55940	9.8	(204)
HU 308	7.6	(234)
JWH 015	7.9	(211)
JWH 133	8.5	(218)
JWH 267	8.1	(219)
L 759633	8.2	(216)
L 759656	7.9	(216)
O 2545	9.9	(217)
O 1812	5.4	(206)
THC	7.1	(208)
WIN 55212-2	9.6	(207)

Cannabinoid receptor CB2 antagonists

Ligand	Experimental pK_i	Reference
AM 281	5.4	(225)
CP 272871	6.9	(226)
JTE 907	7.4	(208)
LY 320135	4.8	(80)
MK 0364	6.5	(231)
NESS 0327	7.7	(228)
O 1184	8.1	(239)
O 2050	8.8	(64)
Sch 336	9.4	(232)
SR 141716	6.9	(221)
SR 144528	9.2	(224)
SR 147778	6.4	(223)

APPENDIX IV

RESIDUES IMPLICATED IN LIGAND BINDING VIA MUTAGENESIS STUDIES

Cannabinoid receptor CB1

Residue	Ligand with possible interaction	Reference
D2.50	WIN55212-2	(248)
K2.38	Classical and non-classical cannabinoids	(242)
F3.25	Anandamide	(167)
L3.29	CP55940, HU210, THC	(243)
G3.31	WIN55212-2	(247)
F3.36	SR141716, WIN55212-2	(167)
F268	CP55940, HU210, methanandamide	(246)
P269	CP55940, HU210, methanandamide	(246)
H270	CP55940, HU210, methanandamide	(246)
I271	CP55940, HU210, methanandamide	(246)
Y5.39	Anandamide, CP55940, WIN55212-2	(166)
W5.43	SR141716, WIN55212-2	(167)
C6.47	Classical and non-classical cannabinoids	(245)
W6.48	SR141716, WIN55212-2	(167)
M6.55	CP55940, HU210, THC	(243)
S7.39	AM4056, CP55940, HU210, MK0364	(169,244)
C7.42	SR141716	(184)

Cannabinoid receptor CB2

Residue	Ligand with possible interaction	Reference
K3.28	JWH015	(164)
S3.31	Classical and non-classical cannabinoids	(164)
W4.50	HU210, 2-AG, CP55940, WIN55212-2	(254)
S4.53	SR144528	(170)
S4.57	SR144528	(170)
W4.64	HU210, 2-AG, CP55940, WIN55212-2	(254)
C174	CP55940, WIN55212-2, Anandamide	(170,255)
C175	SR144528, WIN55212-2	(170)
C179	CP55940, WIN55212-2, Anandamide	(170,255)
Y5.39	Anandamide	(166)
W5.43	CP55940, WIN55212-2, SR144528	(171)
F5.46	WIN55212-2	(165)
W6.48	CP55940	(253)

*   Residues C2.59, V6.51, L6.52, L6.54, M6.55, L6.59, and T6.62 have been experimentally shown to be accessible in the binding site crevice of the CB2 receptor (251,252).

APPENDIX V

PREDICTED BINDING AFFINITIES OF FENOFIBRATE DERIVATIVES ADOPTING THE PREDICTED BINDING CONFORMATION

No	Experimental pK_i	Predicted pK_i
24f	6.66	8.11
24g	7.82	7.81
24h	7.80	7.78
25a	6.23	7.98
25b	6.37	8.17
25c	6.62	8.07
25f	5.88	8.42
26a	5.94	7.65
26c	5.87	8.00
26d	5.81	8.24
26e	6.12	8.35
27c	6.51	7.60
27f	6.84	7.28
28c	7.54	7.84
28i	7.85	7.92

APPENDIX VI

PHARMACOLOGY OF NOVEL FENOFIBRATE DERIVATIVES DESIGNED BASED ON MODELLING DATA
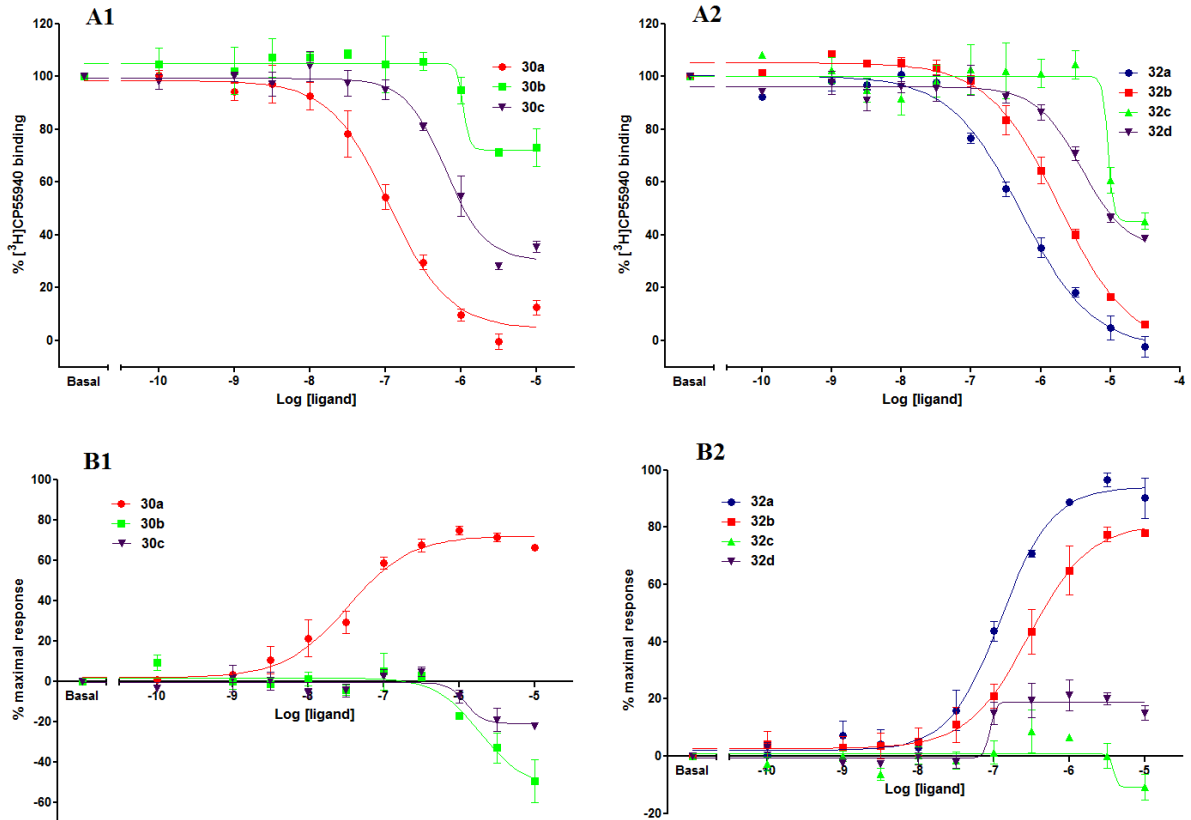
(A) Displacement of [^{3}H]CP55940 from membrane homogenates of CHO cells expressing the human CB2 receptor. (B) Measurement of enhancement of [^{35}S]GTPγS binding in membrane homogenates of CHO cells expressing the CB2 receptor, expressed as a percentage of the response achieved by 1μM CP55940. The figures represent mean values ± SEMs of three independent experiments.